HIGH-RESOLUTION IMAGING OF MAGNETIC FIELDS USING SCANNING SUPERCONDUCTING QUANTUM INTERFERENCE DEVICE (SQUID) MICROSCOPY

By

Luis E. Fong de los Santos

Dissertation

Submitted to the Faculty of the

Graduate School of Vanderbilt University

in partial fulfillment of the requirements

for the degree of

DOCTOR OF PHILOSOPHY

in

Physics

May, 2005

Nashville, Tennessee

Approved by:

Professor Franz Baudenbacher

Professor John P. Wikswo

Professor David Ernst

Professor Thomas Kephart

Professor Jonathan Gilligan

ACKNOWLEDGMENTS

Well known is the fact that great projects require the cooperation of a number of great individuals, and this was definitely the case in my case. That is why I consider very important to thank all the people who participated in this long lasting and fascinating project.

First of all I would like to thank the members of my committee for their support and guidance through my PhD, sometimes winding path.

I owe a special debt of gratitude to my thesis advisor and committee chair, Dr. Franz Baudenbacher. He is the founding father of SQUID microscopy at Vanderbilt, who created the required basis for my project. He also taught me the art of experimental physics and instrument development. He always provided me with valuable information and guidance through every step of the PhD process.

I also had the privilege to work with Dr. John P. Wikswo. His passion and dedication to science and his personal intensity to pursue any project he sets his mind on, have set an example for my future. Thanks to him, I learned the important inter-personal and leadership skills that are crucial for a successful career. I feel honored by this opportunity.

I also would like to thank Dr. David Ernst for his valuable contribution and continuous support to the Latin-American community of scientists. Dr. Ernst has an exceptional combination of a great heart and a great mind. I greatly appreciate all the moments when I had the opportunity to talk to him. He always has something interesting and useful to share with you. I am glad, we met back in Monterrey.

I also would like to thank the rest of the members of my committee: Dr. Fred Gittes, Dr. Tom Kephart and Dr. Jonathan Gilligan for their contributions. Their support, suggestions and ideas were important for the success of this work.

I also would like to express my sincere appreciation to all the collaborators of our group. Dr. Masoud Radparvar at Hypres helped with the fabrication of the SQUID sensors. I am grateful to Dr. Benjamin Weiss for his continuous support in the development of SQUID microscopy; his projects are the driving engine for the continuous improvement of this novel instrument. Thanks to him, I had the opportunity to work with interesting and exciting samples like the Martian meteorite ALH84001. I also would like to express a special gratitude to Dr. Zvonko Trontelj, whose efforts were a fundamental piece on the completion of the Chara project. This project introduced me for the first time to the wonderful world of SQUID microscopy and initiated me as an experimental physicist. I also would like to thank Dr. Anne Fu for her contribution of the microfluidic devices, initiating the development of the project that would combine SQUID microscopy and microfluidic devices for the detection of magnetic particles.

Our entire group is composed of very intelligent and bright people, from whom I had the opportunity to learn a number of skills as well as built up strong friendships. Especially, I would like to mention Dr. Eduardo A. Lima, “The MATLAB Guru”. His help was essential in the analysis and processing of the magnetic measurements and field maps. He dedicated a substantial amount of time and energy to our discussions on research related and unrelated topics. Ron Reiserer has provided important technical support during the course of my projects. Always humorous and friendly, Ron was willing to give me a hand. David Schaffer at the VIIBRE lab fabricated and helped me with the design of our microfluidic devices. Dr. Igor Ges made some of the magnetic structures to characterize the imaging properties of our system. I would like to

thank Dr. Yu Pei Ma for her support on the liquid He and N_2 supply as well as for the interesting discussions in SQUID magnetometry. I also appreciate Dr. Jenny Holzer's contributions in the heart measurements and the beginning of the SQUID chips mounting procedure. I also would like to thank my fellow graduate students Krista McBride and Eric Chancellor for their help and enjoyable company in the SQUIDs characterization and in the experiments that we carried on together.

I would like to give special thanks to Cheryl Cosby and Don Berry for their never ending assistance throughout all these years at Vanderbilt, and also the workshop guys, John Fellenstein and Bob Patchin, for their patience and continuous support in the fabrication of all the gadgets and tiny devices and tools for the SQUID microscope system.

My sister, Erika, has helped and cheered me up through some of my moments of frustration. Dr. Manuel Morales, "El Gran Maestro de Maestros", assisted and showed me the light during the difficult coursework times. He encouraged me in the moment of complete desperation and helped me to continue in the proper path. I am forever grateful to him.

I would like to thank all my family, closest friends and colleagues for their sincere support, truly friendship and caring concerns during the time of my PhD work.

I would like express a very special gratitude to my life companion, Natasha for all her love, motivation, patience, thoughtfulness and enormous enthusiasm. She was there with me in all those difficult moments and helped me to learn to focus on a solution of the problem as opposed to the problem itself. Her support was vital for this accomplishment and will be essential for all of those to come.

Most importantly, I would like to thank my parents for all their unconditional love, constant support, prayers, encouragement and advice throughout my life. I dedicate this doctorate degree to them.

TABLE OF CONTENTS

LIST OF TABLES

LIST OF FIGURES

CHAPTER I

INTRODUCTION

1.1. Objectives

The objectives of this research were the development and application of monolithic thin-film low critical temperature (*Tc*) superconducting quantum interference device (SQUID) sensors to measure and image magnetic fields with an unprecedented combination of high spatial resolution and field sensitivity. The sensors were incorporated into a scanning SQUID microscope system, which permits low-noise, precise and non-invasive magnetic field measurements of a variety of samples at distances smaller than 100 μm.

Development of optimized SQUID sensors for specific source configurations requires a clear understanding of the intrinsic parameters and design constraints of the device. Of great practical importance are spatially distributed current sources, typically associated with bioelectric phenomena, and magnetic dipolar sources, present in rock samples and magnetic microparticles.

Currently available multichannel systems for heart and brain diagnostics are able to detect the magnetic field outside the body; nevertheless, the spatial resolution is limited by the large sensor-to-source distance. In order to address the validity of the source configuration models, it is necessary to study the magnetic activity at the tissue level, which requires the utilization of a SQUID microscope to obtain proper magnetic mappings. High resolution imaging of biomagnetic fields will ultimately lead to a better understanding of how the

magnetocardiogram and the magnetoencephalogram are generated, thereby improving their diagnostic value.

Equally important is the development of new tools for rock magnetism and paleomagnetic studies. The sensitivity and resolution of standard technologies are limited by the relatively large sensing coils [1]. Low-*Tc* SQUID microscopy of room temperature samples provides an enhancement in sensitivity of 3 orders of magnitude with a corresponding spatial resolution improvement of 2 orders of magnitude [2]. This instrument can therefore create magnetic maps of thin sections and single mineral grains that can be directly compared with optical and electron microscopy data, thus bringing together rock magnetism and petrology.

Detection, identification and sorting of biological agents have become a highly demanded method in biomedical research and biotechnology. One common approach to detect biological analytes is the use of magnetic microparticles as labels. Typically, separation techniques can not discriminate according to the magnetic moment and can only isolate magnetically-tagged analytes from their non-magnetic counterparts. Our new system is able to detect and identify a single moving magnetic microparticle confined inside a microfluidic channel. The innovative combination of microfluidic devices and low-*Tc* SQUID microscopy opens new possibilities for high-content magnetic flow cytometry and cell sorting.

The following chapters present the development, application and practical significance of room-temperature-sample low-*Tc* SQUID microscopy, which is an emerging and novel technique to measure and image magnetic fields with unparalleled combination of sensitivity and spatial resolution.

1.2. References

[1] W. L. Goodman, V. W. Hesterma, L. H. Rorden, and W. S. Goree, "Superconducting Instrument Systems," *Proceedings of the Ieee*, vol. 61, no. 1, pp. 20-27, 1973.

[2] B. P. Weiss, F. J. Baudenbacher, J. P. Wikswo, and Kirschvink J.L., "Magnetic Microscopy Promises a Leap in Sensitivity and Resolution," *Eos Trans. AGU*, vol. 82, pp. 513-518, 2001.

CHAPTER II

BACKGROUND

2.1. Scanning probe microscopy

Scanning Probe Microscope (SPM) is the generic term for instruments that measure the near-field interaction between a probe and the surface of a sample. The key point of SPMs is to bring the probe as close as possible to the sample, since the field and spatial resolution are highly diminished as the distance between the sample and the probe increases. The result of the measurement, after the sample has been scanned, is a single to three-dimensional (two spatial and one temporal) image of the interaction as a function of position.

Scanning Probe Microscopy has been widely used because of its outstanding spatial resolution and also due to the great variety of near-field interactions available. The first instrument that used this principle was the Topografiner and it was designed by R.D. Young and co-workers in 1971[1,2]. Later on, Gerd Binnig and Heinrich Rohrer improved the mechanical stability of Young's design and created the scanning tunneling microscope (STM) [3]. Binnig and Rohrer shared the Nobel Prize in Physics in 1986 because of their ability to demonstrate atomic resolution in scanning tunneling microscopy. Several other instruments followed the same principle, including magnetic-force microscope (MFM) [4], atomic-force microscope (AFM) [5], scanning near-field optical microscopy (SNOM) [6] among others.

Among some techniques used for imaging magnetic fields we find: Bitter Pattern Imaging [7-9], Magneto-Optical Imaging [7,10,11], Magnetic Force Microscopy [4,12,13], Scanning Electron Microscopy (SEM) [14,15], Lorentz Transmission Electron Microscopy [16-

18], Scanning Electron Microscopy with Polarization Analysis (SEMPA) [19], electron holography [20-24], X-Ray Magnetic Circular Dichroism (XMCD) [25-28], Spin Polarized Low Energy Electron Microscopy (SPLEEM) [29,30], Scanning Magnetoresistive Microscopy [31,32], Scanning Hall Probe microscopy [33-35] and Scanning SQUID microscopy[36-40]. The decision to use one versus the other depends on several factors such as [36,41]: sensitivity, spatial resolution, frequency response, linearity, stability, source-to-sensor distance, detection of fields versus gradients, need to operate in an externally applied field, ability to reject external noise or the applied field, ability to make measurements without perturbing the sample, and the required operating temperatures of both the sample and the sensor.

Scanning superconducting quantum interference device (SQUID) microscopy is one of the most powerful and promising techniques to measure and image magnetic field distributions [37]. This is mainly due to the SQUIDs unsurpassed sensitivity, its linear and easy-to-calibrate response over a large dynamic range, its ability to operate without perturbing the sample, as well as the versatility of the technique its self to measure a great variety of samples.

The goal of this work was to develop an instrument capable of measuring and imaging the magnetic field of samples at room temperature with a combination of high sensitivity and high spatial resolution. To be able to achieve the expected sensitivity and spatial resolution, we proposed the use of monolithic low transition temperature (low-Tc) niobium-based dc SQUID magnetometers integrated into a Scanning SQUID microscope system [40].

2.2. Scanning SQUID microscopy

In recent years, there has been a large increase in the use of SQUID microscopy, mainly as a result of advances in the SQUID design and fabrication, in the mechanism to scan the

sample and in the magnetic shielding and cryogenic technologies. In general, we can classify SQUID microscopy according to the sample's temperature and also to the type of SQUID sensor used. In terms of the sample's temperature, we find SQUID microscopes in which the sample and the sensor are at the same temperature (cold-sample) and others where the sample is at room temperature (warm-sample or room-temperature (RT) sample). In addition, we can also group SQUID microscopes by the transition temperature (*Tc*): low-*Tc* where the SQUID needs to be cooled down to liquid He temperatures, and high-*Tc*, where the SQUID is cool down to liquid N_2 temperatures.

Historically, low-*Tc* cold-sample SQUID microscopes were the first to be developed. Immediately after the invention of the SQUID magnetometer, Zimmerman and Mercereau [42] scanned a 50-μm niobium wire through a window in a two-contact SQUID and provided the first confirmation of the presence of individual quantized vortices trapped in a wire [43,44]. Another group of pioneers, formed by Goodman and Deaver [45,46], developed an innovative SQUID microscope to measure trapped flux in cylindrical tin films. The microscope design had a toroidal, radio frequency (RF) SQUID inductively coupled to a small pick up coil that surrounded a very small tin cylinder. The 14 – 56 μm diameter and 1000 – 5000 Å thick tin cylinder was vertically scanned. They demonstrated that different portions of the cylinder can be in different flux states and support differing persistent currents [46].

The first two-dimensional scanning SQUID microscope was developed by Rogers and Bermon [47]. They observed flux trapped in an array of 0.1 mm square holes in a superconducting niobium thin film. More recently, low-*Tc* cold-sample SQUID microscopy has been extensively used to study a great variety of superconducting phenomena. Vortices trapped in planar superconducting films [48,49], Meissner imaging [50,51], phase-sensitive symmetry

tests [52-62], interlayer Josephson vortices [63-67], vortex-like excitations (visons) [68-70], diamagnetic shielding above *Tc* [71,72] and measurements of magnetic properties of small particles [73,74] are some of the exciting areas where low-*Tc* cold-sample SQUID microscopy has shown to be a valuable tool for fundamental research.

Another rapidly emerging area for SQUID microscopy development is the use of high-*Tc* SQUID sensors. Black and co-workers [75] were the pioneers on using high-*Tc* SQUIDs to study cold samples with a variety of techniques, including static magnetization [76], eddy current [77], radio frequency [78] and microwave imaging [79]. High-*Tc* RT-sample SQUID microscopy has recently been extensively developed by two groups: the Wellstood group at the University of Maryland [80-84] and the Clarke group at University of California at Berkeley [38,85-89]. For some applications, the higher operating temperatures of high-*Tc* SQUID microscope systems provide an important advantage in comparison with low-*Tc* SQUID systems. High-*Tc* SQUIDs operate around 77 K, so the cryogenic as well as the radiation shielding requirements are much less restrictive. However, higher operating temperatures impose higher intrinsic noise levels, since the SQUID flux noise scales up with $T^{1/2}$, where T is temperature of the sensor. High-*Tc* SQUIDs also suffer from excess of 1/f noise at low frequencies. Therefore, high-*Tc* SQUIDs have not yet achieved the key combination of low-noise performance, low-frequency sensitivity and high spatial resolution needed for imaging weak biomagnetic signals associated with bioelectric currents in living tissue [90-92].

Besides these applications, low-*Tc* RT-sample scanning SQUID microscopy has found an important area for development in the field of electromagnetic nondestructive evaluation (NDE). The sensitivity of low-*Tc* SQUIDs at low frequencies allows them to work as eddy-current sensors with unmatched depth resolution, as well as to image the static magnetization of

paramagnetic materials and the flow of near-dc corrosion currents. SQUIDs' wide dynamic range make them suitable to image defects in steel structures and to measure the magnetomechanical behavior of ferromagnetic materials. The main three areas where SQUID microscopy has been used for NDE experiments are: flaw characterization, magnetic properties of materials and corrosion studies. In all of these areas, the SQUID measures the weak magnetic flux and gives an image of the magnetic field distribution in the vicinity of the test object. The magnetic field sources can be intrinsic in the test object or one may use an external source of electric or magnetic field to excite the test object for a resultant magnetic field. A more extensive review of SQUIDs and SQUID microscopy for NDE can be found in Weinstock *et al.* [93,94], Donaldson *et al.* [95], Cochran *et al.* [96-99] and Wikswo *et al*. [100-108].

In the past years, substantial improvements in low-*Tc* RT-sample scanning SQUID microscopy have been made at Vanderbilt University. Baudenbacher *et al.* were the pioneers in the incorporation of hand-wound 25 μm-superconducting niobium-wire miniature (250 to 500 μm diameter) pickup coils connected directly to the terminals of a flux transformer circuit of commercial low-*Tc* SQUID sensors, as well as in the development of innovative cryogenic Dewars, which allows bringing the probe, held at cryogenic temperatures, to distances closer than 100 μm from a RT sample [39]. Using this system, Baudenbacher *et al.* measured and imaged the weak magnetic field of rock samples [109-111], including the well-known Martian meteorite ALH84001. They also measured the magnetic signals from isolated rabbit hearts [90,92] and the time evolution of the field produced by plant cells [112]. Subsequent improvements included the development, fabrication and incorporation of monolithic niobium-based SQUID sensors to the SQUID microscope system in order to measure directly the magnetic field of RT samples at distances smaller than 100 μm. The new system has played an

important role in the development of novel paleomagnetic and rock magnetism analysis, cardiac electrophysiology studies and magnetic flow cytometry. The details of the development the SQUID sensors, their further incorporation into our SQUID microscope and applications of this pioneering system are the main focus of this dissertation.

Recently, Kominis *et al*. [113] have developed a new technique to measure magnetic fields with subfemtotesla sensitivity. By measuring the Zeeman effect, they have designed the atomic magnetometer. The atomic or optical magnetometer measures the magnetic-field-induced shift of the energy levels of an atom's spin states. This is a big accomplishment in terms of sensitivities and represents a major improvement in the state of the art techniques for measuring the magnetic field; nevertheless there are several obstacles that need to be addressed before this new technology will replace SQUIDs for most applications [114].

2.3. Introduction to SQUIDs

2.3.1. Flux Quantization

SQUIDs bring together two basic superconducting phenomena. On the one side, we have flux quantization, which arises from Landau-Ginzburg equations. In 1950, Landau and Ginzburg [115,116] proposed to describe the superconducting state by means of a macroscopic wave function Ψ. The Landau-Ginzburg equations predict that the magnetic flux trapped within a superconductor ring is quantized in units of Φ_o, where Φ_o is the flux quantum and has a value of: 2.07×10^{-15} Wb. Figure 2.1 (left) shows a schematic of flux quantization. The phenomenological explanation of this behavior comes from the ability of a superconductor to respond to an external magnetic field. Meissner and Ochsenfeld [117] found in 1933 that the magnetic fields are expelled from a superconductor due to the creation of superconducting currents that do not

display any damping. Therefore, the flux threading the ring is held constant by these superconducting currents which flow in the ring to oppose any change in flux applied to the ring.

2.3.2. Josephson Effect

On the other side, we have the Josephson junction effect [118,119]. A Josephson junction is a weak link or insulator placed between two superconductors. Using the same treatment as with the flux quantization, it is possible to describe the superconducting state, and thus the charge carriers (Cooper pairs) using a macroscopic wave function Ψ with an arbitrary phase θ. The charge carriers tunnel through the junction and the relative phase $\delta = \theta_1 - \theta_2$ affects the electrical properties of the junction. Figure 2.1 (right) shows a schematic of a Josephson junction and the corresponding Josephson equations. The Cooper tunneling is an example of the quantum mechanical nature of superconductivity

There are two important effects present in Josephson junctions: the dc Josephson effect [120] and the ac Josephson effect [121]. In the first one, a dc current flows through the junction without a voltage being developed across it, provided the current is below a certain value, I_C (the critical current). This gives rise to the current-phase relation (Fig. 2.1):

$$I = I_C \sin\delta \tag{2.1}$$

In the ac Josephson effect, a dc voltage, V, applied across a junction will cause oscillations in the current through the junction and the phase difference will increase with time. This is expressed as the voltage phase relation:

$$\frac{d\delta}{dt} = \frac{2\pi}{\Phi_0} V \tag{2.2}$$

where the magnetic flux quantum $\Phi_o = h/2e$.

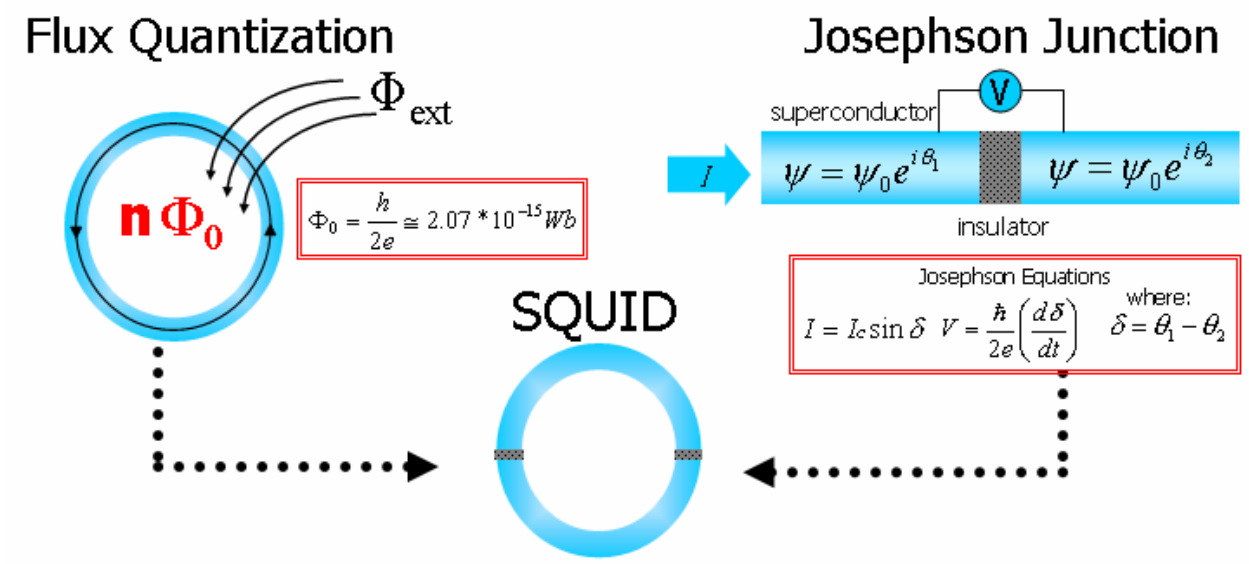

Figure 2.1: A SQUID works with the combination of two superconducting effects: flux quantization and the Josephson junction effect. Flux quantization (left) occurs in a superconducting ring enclosing only certain amounts of magnetic flux which are integer units n of the flux quantum Φ_o. A Josephson junction (right) is a weak link or insulator between two superconductors. The relative phase δ of the superconducting order parameter Ψ after tunneling the junction affects the electrical properties of the junction. The relationship between the electrical properties and the relative phase is shown by the Josephson equations.

An applied magnetic field will periodically modulate the maximum supercurrent that can flow through the junction. By plotting the maximum supercurrent as a function of flux in the junction, an intereference pattern is obtained as shown in Fig. 2.2. In the small junction limit, the theoretical $I_C - B$ pattern is described by the following equation:

$$\frac{I_C(\Phi)}{I_C(0)} = \left| \frac{\sin\left(\frac{\pi\Phi}{\Phi_0}\right)}{\frac{\pi\Phi}{\Phi_0}} \right| \tag{2.3}$$

2.3.3. The Resistively Shunted Junction (RSJ) Model

Typically, the Josephson junction is represented with the equivalent circuit of the ideal, noise-free, resistively shunted junction (RSJ), where we have the Josephson junction (X), its

physical capacitance (C) and the resistor (R), all joined in parallel. The circuit diagram of this model is shown in Fig. 2.3.

Initially for current $I < I_C$, the voltage across the junction is zero and the current is given by equation 2.1. For $I > I_C$, a voltage appears and the phase difference becomes time dependent as express in equation 2.2. Using Kirchhoff's law, the Josephson equations (2.1 and 2.2) and rearranging in a dimensionless form we get the following non-linear second order differential equation:

$$\frac{I}{I_C} = \sin\delta + \frac{d\delta}{d\bar{\tau}} + \beta_C \frac{d^2\delta}{d\bar{\tau}^2} \tag{2.4}$$

where

$$\bar{\tau} = \frac{t}{\tau_C} \tag{2.5}$$

$$\tau_C = \frac{\Phi_0}{2\pi I_C R} = \text{the junction time constant} \tag{2.6}$$

and

$$\beta_C = \frac{RC}{\tau_C} = \frac{\tau_{RC}}{\tau_C} = \text{Steart McCumber parameter [122,123]} \tag{2.7}$$

A analogous model to understand the dynamics of the junction is by realizing that equation 2.4 also describes a ball moving on a "tilted washboard". In this model, a ball rolls down a tilted ridged plane as shown in Fig. 2.4 [124]. The displacement of the ball is represented by δ, the angle of the slope, θ, is the analogue of current *I*, the velocity of the ball correspond to the voltage, *V*, across the junction and the inertia of the ball is analogous to the capacitance, *C*, of the system.

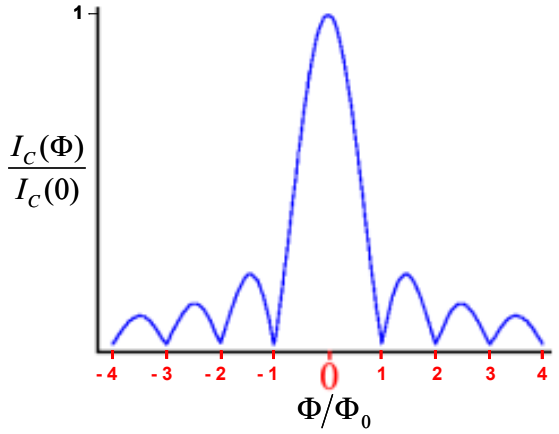

Figure 2.2: I_C-B pattern of a junction.

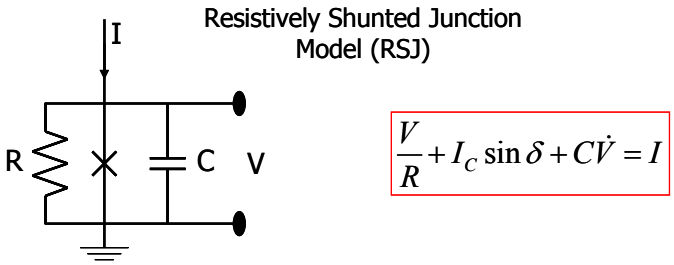

Figure 2.3: The equivalent circuit of the ideal, noise-free, resistively shunted junction (RSJ) and its corresponding equation

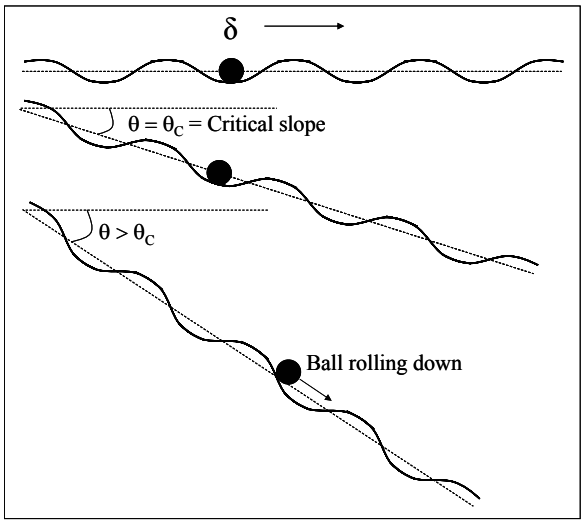

Figure 2.4: Tilted washboard analogy to illustrate the Josephson junction dynamics.

By increasing the driving current I (with $I < I_C$), the current phase relation δ changes but the time average of δ, which is proportional to the average voltage, will be zero. This is equivalent to having the washboard slightly tilted, at first the ball will oscillate in a potential minimum, but the time average of the displacement will be zero. When the angle of the plane exceeds a critical angle θ_C ($\theta > \theta_C$), the ball will move into the next potential minimum and continue to roll at an increasing rate due to gravity. This is analogous to exceeding the critical current of the junction, therefore increasing the voltage which in turn increases the phase difference across the junction.

Now, by taking into account the capacitance of the system, which is equivalent to the inertia of the washboard model, we can analyze the following two cases:

Overdamped Case or $\beta_C << 1$:

In this scenario $\tau_C >> \tau_{RC}$ and the phase δ evolves slower than the capacitor relaxation. Equation 2.4 becomes:

$$\frac{I}{I_C} = \sin\delta + \frac{d\delta}{d\bar{\tau}} \tag{2.8}$$

When $I < I_C$, all the current flows through the junction and the time average of the voltage $V = 0$. If $I > I_C$ some current will flow creating a voltage drop through the resistor, causing δ to change. Integrating equation 2.8 and extracting the dc voltage component we obtain:

$$V = IR\sqrt{1-\left(\frac{I_C}{I}\right)^2} \tag{2.9}$$

The voltage-current relation is shown in Fig. 2.5. This is the non-hysteretic theoretical V-I characteristic curve. Following the washboard analogy, the ball has little inertia and therefore when the angle of the slope passes through θ_C, the ball returns to a potential minimum.

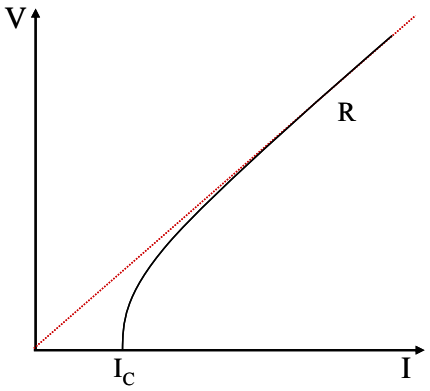

Figure 2.5: Single Josephson junction VI characteristic curve.

Underdamped Case or $\beta_C >> 1$:

In this case $\tau_C << \tau_{RC}$, therefore the dynamics of the circuit is directed solely by *R* and *C*. For $I < I_C$, current can still flow through the resistor; when $I > I_C$, the system switches to a finite voltage given by $V=IR$. Since the dynamics of the system are determined by τ_{RC}, when the current goes below I_C the junction stays with a finite voltage. Therefore, the V-I characteristic curve is hysteretic (Fig. 2.6) and the amount of hysteresis is given by β_C. In the washboard analogy, the ball has a large inertia and consequently when the angle of the slopes comes back to θ_C, the ball will continue to roll, making the system hysteretic. In an optimized SQUID, the junctions must be non-hysteretic ($\beta_C < 1$), since hysteresis causes noise due to switching between different states.

In order to have a more realistic model for the junctions, a noise term must be introduced as shown in the following equation:

$$I + I_n(t) = I_C \sin\delta + \frac{V}{R} + C\frac{dV}{dt} \tag{2.10}$$

where $I_n(t)$ represents the Nyquist current noise associated with the shunt resistance *R*, having a spectral density in the thermal noise limit given by:

$$S_I(f) = \frac{4k_B T}{R} \tag{2.11}$$

Going back to the washboard analogy, this term ($I_n(t)$) represents fluctuation in the inclination angle.

Even though $I < I_C$, this current noise could cause phase slip. Since $I + I_n(t)$ can fluctuate above the critical current, it could give rise to voltage spikes. This means that for currents just below I_C, finite voltages are observed and the V-I characteristic curve becomes noise rounded [125]. A measurement of the amount of noise rounding is given by the noise parameter, Γ:

$$\Gamma = \frac{2\pi k_B T}{I_C \Phi_0} = \frac{thermal\ energy}{Josephson\ coupling\ energy} \tag{2.12}$$

In order to achieve coherence and maintain the Josephson coupling energy above the thermal fluctuations, we need that $\Gamma << 1$.

For $I > I_C$, we observe a voltage noise due to a Nyquist noise current flowing through a dynamic resistance R_d,

$$R_d = \frac{dV}{dI} \tag{2.13}$$

In the limit when $\beta_C << 1$ and $f << f_J$ (the Josephson frequency = V/Φ_o), the spectral density of the voltage noise across the SQUID $S_V(f)$ is given by [126,127]:

$$S_V(f) = \left[1 + \frac{1}{2}\left(\frac{I_C}{I}\right)^2\right]\frac{4k_B T R_d^2}{R} \tag{2.14}$$

where the first term represents the Nyquist noise current flowing through the dynamic resistance R_d as a function of frequency f.

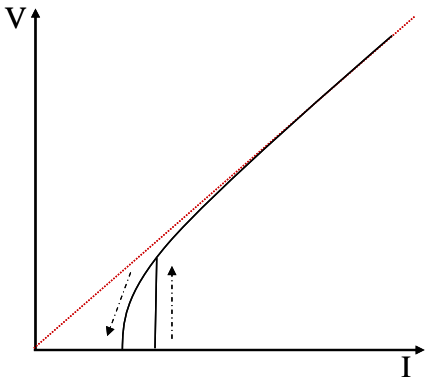

Figure 2.6: Hysteretic junction VI characteristic curve for increasing and decreasing current.

When designing a SQUID sensor, it is important to consider the $I_C R$ product, the critical current density J_C and the resistance-area product ρ_N, since they will determine the junction quality. The critical current density is given by:

$$J_C = \frac{I_C}{A_{JX}} \tag{2.15}$$

where A_{JX} is the cross-sectional area of the junction and is given by:

$$A_{JX} = tw \tag{2.16}$$

where t is the thickness of the film and w the width of the junction. Finally, the resistance-area product ρ_N, is given by:

$$\rho_N = RA_{JX} \tag{2.17}$$

2.3.4. DC SQUID

The RSJ model can be extended to the dc SQUID (Fig. 2.7). For practical purposes, we will assume that the junctions are identical and non-hysteretic. The body of the SQUID possesses an intrinsic inductance L. With the absent of any external magnetic flux, the bias current, I, will split equally between paths 1 and 2, with no voltage drop for values of $I < 2I_C$. Figure 2.8 shows the V-I characteristic curve for a dc SQUID with no external applied flux.

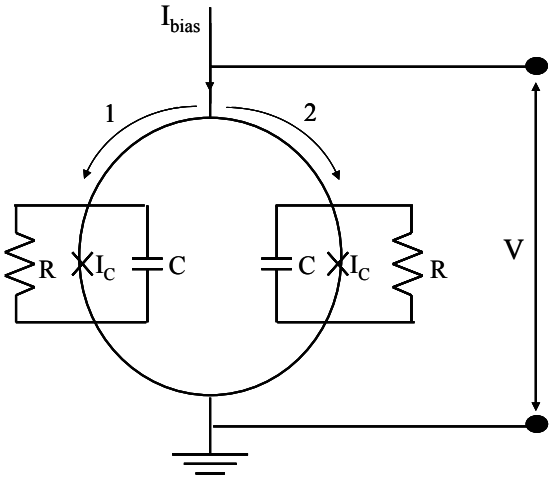

Figure 2.7: Schematic of a dc SQUID

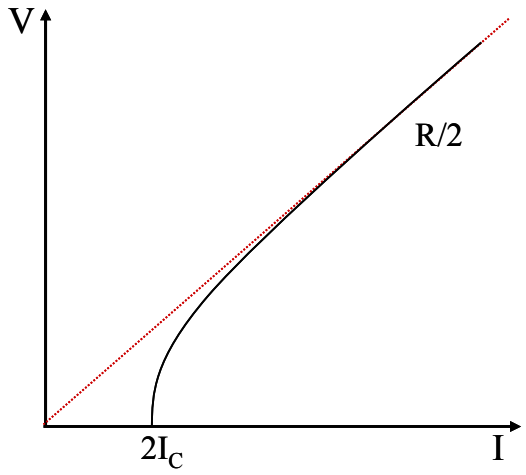

Figure 2.8: VI characteristic curve for a dc SQUID with no applied flux.

Now, by applying a small magnetic flux ($\Phi_{ext} < \Phi_o/2$), the SQUID will generate an opposing circulating current, I_S. Since this circulating screening current is superimposed over the bias current, the external magnetic field reduces the amount of bias current that can go through the SQUID without a voltage drop. Therefore the critical current of the SQUID becomes a function of the amount of applied magnetic field. For $LI_C >> \Phi_o$, the flux inside the superconducting ring becomes an integral number of Φ_o,

$$\Phi = \Phi_{ext} + LI_S = n\Phi \tag{2.18}$$

where n is the integer closest to Φ_{ext}/Φ_o. Therefore

$$I_S = \frac{n\Phi_0 - \Phi_{ext}}{L} \tag{2.19}$$

As Φ_{ext} is increased from zero to Φ_o, the ring stays in the $n = 0$ flux state and generates a current given by:

$$I_S = \frac{-\Phi_{ext}}{L} \tag{2.20}$$

When $\Phi_{ext} = \Phi_o/2$, it becomes energetically favorable to allow one Φ_o into the SQUID, and the screening current reverses direction. Figure 2.9 shows the variation I_S as a function of applied flux. The screening current (I_S) is a periodic function with a period equal to Φ_o.

One feature that requires attention to understand the SQUID operation is the fact that the critical current is a periodic function of the applied flux. Since the critical current depends on the screening current, the maximum supercurrent, I_m, in the SQUID is also periodic with applied flux with a period of Φ_o and a maximum value of $2I_C$. This is shown in Fig. 2.10.

By applying a magnetic flux, the V-I curve of a dc SQUID will oscillate between two states: the integer ($\Phi = n\Phi_o$) and half integer flux ($\Phi = (n+1/2)\Phi_o$) states. This oscillation produces a voltage modulation, ΔV, as a function of applied magnetic flux. Instead of measuring the change in critical current as a function of applied flux, it is easier to current bias the SQUID at a constant value in the finite voltage regime and measure the modulation voltage as a function of applied flux. This is how one creates a V-Φ characteristic curve. Figure 2.11 shows this in detail.

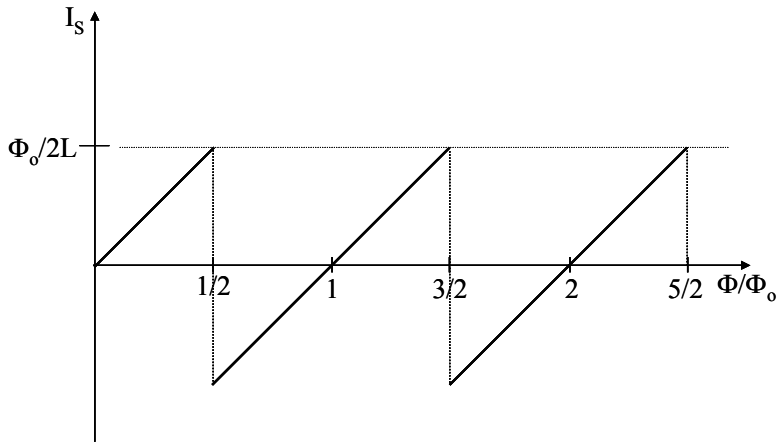

Figure 2.9: Variation of the screening current as a function of applied flux.

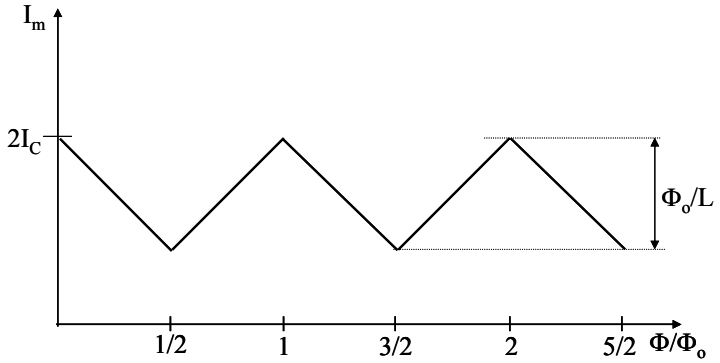

Figure 2.10: Variation of the maximum supercurrent as a function of applied flux.

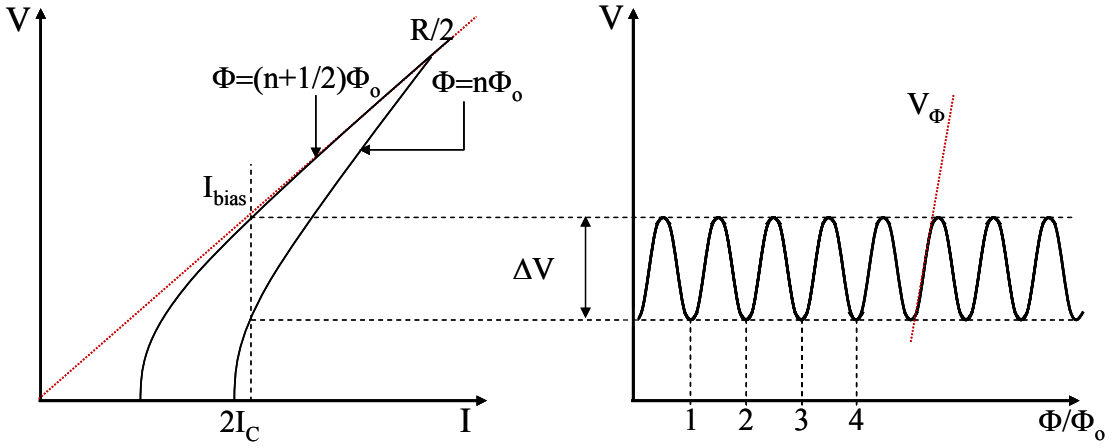

Figure 2.11: Periodic SQUID voltage response as a function of applied flux for a defined constant bias current.

The modulation voltage, ΔV, is the actual output signal of a dc SQUID as a function of applied flux (Φext). Therefore, we can say that a dc SQUID is basically a flux-to-voltage transducer with a non-linear and periodic transfer function. The non-linearity of the output imposes an inconvenience to use the dc SQUID as a magnetic sensor. In order to get around this difficulty, Ketchen *et al*. came out with the idea of operating the SQUID in a Flux-Locked Loop (FLL) [128]. Figure 2.12 shows a schematic of a dc SQUID operated in a FLL. An oscillator applies a modulation flux (100 kHz signal) to the SQUID through the feedback coil. The voltage signal of the SQUID, Vs, goes through a preamplifier, is synchronously detected and then sent through an integrating circuit. The smoothed output of the integrator is connected to the feedback coil via a resistor R_f. In this way, for a flux change $\delta\Phi$ detected by the SQUID, the feedback circuit will produce an opposing flux $-\delta\Phi$ and a voltage proportional to $\delta\Phi$ can be measured across R_f. In other words, the FLL is a negative feedback circuit that creates a null-detector of magnetic flux and allows flux changes, ranging from much less than a single flux quantum to many flux quanta, to be measured with sub-flux quantum accuracy. The combination of a dc SQUID and the FLL electronics makes a SQUID sensor, which is the most sensitive magnetic flux-to-voltage transducer.

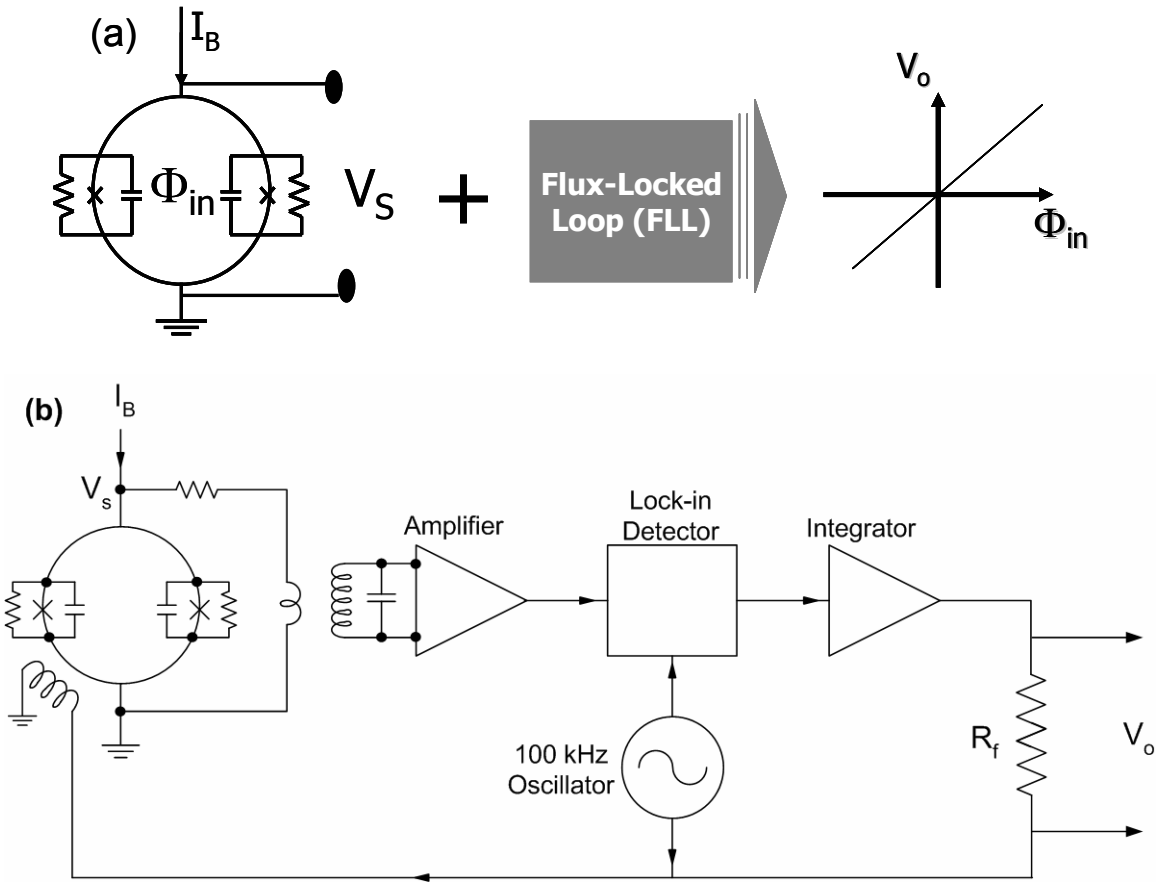

Figure 2.12: (a) The transfer function between the input magnetic flux Φ_{in} and the voltage output of the SQUID V_s is nonlinear and periodic. In order to have a linear relationship, we operate the SQUID in a Flux-Locked Loop (FLL). (b) FLL modulation and feedback circuit (adapted from 102). The SQUID is coupled to the preamplifier via a cooled step-up transformer. The voltage response of the SQUID V_s is the input of the FLL, which uses a modulation flux scheme to maintain the SQUID at an extremum on the V-Φ curve. The user measures a change in V_o, which is proportional to the amount of flux changed detected by the SQUID.

2.6. References

[1] R. Young, J. Ward, and F. Scire, "Topografiner - Instrument for Measuring Surface Microtopography," *Rev. Sci. Instrum.*, vol. 43, no. 7, p. 999-&, 1972.

[2] R. D. Young, "Surface Microtopography," *Physics Today*, vol. 24, no. 11, p. 42-&, 1971.

[3] G. Binnig, H. Rohrer, C. Gerber, and E. Weibel, "7X7 Reconstruction on Si(111) Resolved in Real Space," *Phys. Rev. Lett.*, vol. 50, no. 2, pp. 120-123, 1983.

[4] Y. Martin and H. K. Wickramasinghe, "Magnetic Imaging by Force Microscopy with 1000-A Resolution," *Appl. Phys. Lett.*, vol. 50, no. 20, pp. 1455-1457, 1987.

[5] G. Binnig, C. F. Quate, and C. Gerber, "Atomic Force Microscope," *Phys. Rev. Lett.*, vol. 56, no. 9, pp. 930-933, 1986.

[6] D. W. Pohl, W. Denk, and M. Lanz, "Optical Stethoscopy - Image Recording with Resolution Lambda/20," *Appl. Phys. Lett.*, vol. 44, no. 7, pp. 651-653, 1984.

[7] D. J. Craik, "The Observation of Magnetic Domains, in Methods of Experimental Physics,". R. V. Coleman, Ed. New York: Academic Press, 1974, pp. 675-743.

[8] D. J. Bishop, P. L. Gammel, D. A. Huse, and C. A. Murray, "Magnetic Flux-Line Lattices and Vortices in the Copper-Oxide Superconductors," *Science*, vol. 255, no. 5041, pp. 165-172, 1992.

[9] O. Kitakami, T. Sakurai, and Y. Shimada, "High density recorded patterns observed by high-resolution Bitter scanning electron microscope method," *J. Appl. Phys.*, vol. 79, no. 8, pp. 6074-6076, 1996.

[10] P. L. Trouilloud, B. Petek, and B. E. Argyle, "Methods for Wide-Field Kerr Imaging of Small Magnetic Devices," *IEEE Trans. Mag.*, vol. 30, no. 6, pp. 4494-4496, 1994.

[11] B. E. Argyle and J. G. Mccord, "New laser illumination method for Kerr microscopy," *J. Appl. Phys.*, vol. 87, no. 9, pp. 6487-6489, 2000.

[12] R. H. Koch, J. Clarke, W. M. Goubau, J. M. Martinis, C. M. Pegrum, and D. J. Vanharlingen, "Flicker (1/F) Noise in Tunnel Junction Dc Squids," *J. Low Temp. Phys.*, vol. 51, no. 1-2, pp. 207-226, 1983.

[13] D. Sarid, *Scanning Force Microscopy*. New York: Oxford University Press, 1991.

[14] D. E. Newbury, D. C. Joy, P. Echlin, C. E. Fiori, and J. I. Goldstein, *Advanced Scanning Electron Micrsocopy and X-Ray Microanalysis*. New York: Plenum Press, 1986.

[15] L. Reimer, *Scanning Electron Microscopy*. Berlin: Springer-Verlag, 1985.

[16] H. Ardhuin, J. N. Chapman, P. R. Aitchison, M. F. Gillies, K. J. Kirk, and C. D. W. Wilkinson, "Magnetization reversal of patterned spin-tunnel junction material: A transmission electron microscopy study," *J. Appl. Phys.*, vol. 88, no. 5, pp. 2760-2765, 2000.

[17] J. N. Chapman, S. Mcvitie, and I. R. Mcfadyen, "Magnetic-Structure Determination by Scanning-Transmission Electron-Microscopy," *Scanning Microscopy*, pp. 221-228, 1987.

[18] J. N. Chapman, "The Investigation of Magnetic Domain-Structures in Thin Foils by Electron-Microscopy," *Journal of Physics D-Applied Physics*, vol. 17, no. 4, p. 623-&, 1984.

[19] M. R. Scheinfein, J. Unguris, M. H. Kelley, D. T. Pierce, and R. J. Celotta, "Scanning Electron-Microscopy with Polarization Analysis (Sempa)," *Rev. Sci. Instrum.*, vol. 61, no. 10, pp. 2501-2526, 1990.

[20] A. Tonomura, *Electron Holography*. Berlin: Springer-Verlag, 1994.

[21] M. Mankos, J. M. Cowley, and M. R. Scheinfein, "Quantitative micromagnetics at high spatial resolution using far-out-of-focus STEM electron holography," *Physica Status Solidi A-Applied Research*, vol. 154, no. 2, pp. 469-504, 1996.

[22] D. G. Streblechenko, M. R. Scheinfein, M. Mankos, and K. Babcock, "Quantitative magnetometry using electron holography: Field profiles near magnetic force microscope tips," *IEEE Trans. Mag.*, vol. 32, no. 5, pp. 4124-4129, 1996.

[23] R. M. Tromp, M. Mankos, M. C. Reuter, A. W. Ellis, and M. Copel, "A new low energy electron microscope," *Surface Review and Letters*, vol. 5, no. 6, pp. 1189-1197, 1998.

[24] K. Harada, T. Matsuda, J. Bonevich, M. Igarashi, S. Kondo, G. Pozzi, U. Kawabe, and A. Tonomura, "Real-Time Observation of Vortex Lattices in A Superconductor by Electron-Microscopy," *Nature*, vol. 360, no. 6399, pp. 51-53, 1992.

[25] J. Stohr, Y. Wu, B. D. Hermsmeier, M. G. Samant, G. R. Harp, S. Koranda, D. Dunham, and B. P. Tonner, "Element-Specific Magnetic Microscopy with Circularly Polarized X-Rays," *Science*, vol. 259, no. 5095, pp. 658-661, 1993.

[26] B. P. Tonner, D. Dunham, J. Zhang, W. L. Obrien, M. Samant, D. Weller, B. D. Hermsmeier, and J. Stohr, "Imaging Magnetic Domains with the X-Ray Dichroism Photoemission Microscope," *Nuclear Instruments & Methods in Physics Research Section A-Accelerators Spectrometers Detectors and Associated Equipment*, vol. 347, no. 1-3, pp. 142-147, 1994.

[27] G. Denbeaux, P. Fischer, G. Kusinski, M. Le Gros, A. Pearson, and D. Attwood, "A full field transmission X-ray microscope as a tool for high-resolution magnetic imaging," *IEEE Trans. Mag.*, vol. 37, no. 4, pp. 2764-2766, 2001.

[28] P. Fischer, T. Eimuller, G. Schutz, P. Guttmann, G. Schmahl, K. Pruegl, and G. Bayreuther, "Imaging of magnetic domains by transmission x-ray microscopy," *Journal of Physics D-Applied Physics*, vol. 31, no. 6, pp. 649-655, 1998.

[29] E. Bauer, "Low-Energy-Electron Microscopy," *Reports on Progress in Physics*, vol. 57, no. 9, pp. 895-938, 1994.

[30] R. Zdyb and E. Bauer, "Magnetic domain structure and spin-reorientation transition in ultrathin Fe-Co alloy films," *Physical Review B*, vol. 67, no. 13 2003.

[31] S. Y. Yamamoto and S. Schultz, "Scanning magnetoresistance microscopy (SMRM): Imaging with a MR head," *J. Appl. Phys.*, vol. 81, no. 8, pp. 4696-4698, 1997.

[32] S. Y. Yamamoto and S. Schultz, "Scanning magnetoresistance microscopy," *Appl. Phys. Lett.*, vol. 69, no. 21, pp. 3263-3265, 1996.

[33] A. M. Chang, H. D. Hallen, L. Harriott, H. F. Hess, H. L. Kao, J. Kwo, R. E. Miller, R. Wolfe, J. Vanderziel, and T. Y. Chang, "Scanning Hall Probe Microscopy," *Appl. Phys. Lett.*, vol. 61, no. 16, pp. 1974-1976, 1992.

[34] A. Oral, S. J. Bending, and M. Henini, "Real-time scanning hall probe microscopy," *Appl. Phys. Lett.*, vol. 69, no. 9, pp. 1324-1326, 1996.

[35] A. Sandhu, H. Masuda, and A. Oral, "Room temperature scanning micro-Hall probe microscopy under extremely large pulsed magnetic fields," *IEEE Trans. Mag.*, vol. 39, no. 5, pp. 3462-3464, 2003.

[36] J. R. Kirtley and J. P. Wikswo, Jr., "Scanning SQUID microscopy," *Annual Reviews of Material Science*, vol. 29, pp. 117-148, 1999.

[37] J. R. Kirtley, "SQUID microscopy for fundamental studies," *Physica C-Superconductivity and Its Applications*, vol. 368, no. 1-4, pp. 55-65, 2002.

[38] T. S. Lee, E. Dantsker, and J. Clarke, "High-transition temperature superconducting quantum interference device microscope," *Rev. Sci. Instrum.*, vol. 67, no. 12, pp. 4208-4215, 1996.

[39] F. Baudenbacher, N. T. Peters, and J. P. Wikswo, Jr., "High Resolution Low-Temperature Superconductivity Superconducting Quantum Interference Device Microscope for Imaging Magnetic Fields of Samples at Room Temperatures," *Rev. Sci. Instrum.*, vol. 73, no. 3, pp. 1247-1254, 2002.

[40] Fong L.E., Holzer J.L., K. McBride, E. A. Lima, M. Radparvar, and Baudenbacher F., "High-resolution room-temperature-sample scanning superconducting quantum interference device microscope configurable for geological and biomagnetic applications," *Rev. Sci. Instrum.*, vol. (Accepted for publication) 2005.

[41] R. J. Celotta, J. Unguris, M. H. Kelley, and D. T. Pierce, "Techniques to Measure Magnetic Domain Structures," 2000.

[42] J. E. Zimmerman and J. E. Mercereau, "Quantized Flux Pinning in Superconducting Niobium," *Phys. Rev. Lett.*, vol. 13, no. 4, pp. 125-126, 1964.

[43] R. C. Jaklevic, J. Lambe, A. H. Silver, and J. E. Mercereau, "Quantum interference effects in Josephson Tunneling," *Phys. Rev. Lett.*, vol. 12, no. 7, pp. 159-160, 1964.

[44] J. E. Zimmerman and A. H. Silver, "Quantum effects in type II superconductors," *Physics Letters*, vol. 10, no. 1, pp. 47-48, 1964.

[45] W. L. Goodman and B. S. Deaver, Jr., "Detailed Measurements of the Quantized Flux States of Hollow Superconducting Cylinders," *Phys. Rev. Lett.*, vol. 24, no. 16, pp. 870-873, 1970.

[46] W. L. Goodman, W. D. Willis, D. A. Vincent, and B. S. Deaver, Jr., "Quantized Flux States of Superconducting Cylinders," *Physical Review B*, vol. 4, no. 5, pp. 1530-1538, 1971.

[47] F. P. Rogers, "A device for experimental observation of flux vortices trapped in superconducting thin films." MS MIT, 1983.

[48] M. Jeffery, T. Van Duzer, J. R. Kirtley, and M. B. Ketchen, "Magnetic Imaging of moat-guarded superconducting electronic circuits," *Appl. Phys. Lett.*, vol. 67, no. 12, pp. 1769-1771, 1995.

[49] J. R. Kirtley, C. C. Tsuei, K. A. Moler, V. G. Kogan, J. R. Clem, and A. J. Turberfield, "Variable sample temperature scanning superconducting quantum interference device microscope," *Appl. Phys. Lett.*, vol. 74, no. 26, pp. 4011-4013, 1999.

[50] B. A. Scott, J. R. Kirtley, D. Walker, B.-H. Chen, and Y. Wang, "Application of scanning SQUID petrology to high-pressure materials science," *Nature*, vol. 389, pp. 164-167, 1997.

[51] J. R. Kirtley, C. C. Tsuei, M. Rupp, J. Z. Sun, L. S. YuJahnes, A. Gupta, M. B. etchen, K. A. Moler, and M. Bhushan, "Direct imaging of integer and half-integer Josephson Vortices in High-T_c grain boundaries," *Phys. Rev. Lett.*, vol. 76, no. 8, pp. 1336-1339, 1996.

[52] D. A. Wollman, D. J. Van Harlingen, W. C. Lee, D. M. Ginsberg, and A. J. Leggett, "Experimental determination of the superconducting paring state in YBCO from the phase coherence of YBCO-Pb dc SQUIDs," *Phys. Rev. Lett.*, vol. 71, no. 13, pp. 2134-2137, 1993.

[53] D. A. Brawner and H. R. Ott, "Evidence for an unconventional superconducting order parameter in $YBa_2Cu_3O_{6.9}$," *Physical Review B*, vol. 50, no. 9, pp. 6530-6533, 1994.

[54] C. C. Tsuei, J. R. Kirtley, C. C. Chi, L. S. Yu-Jahnes, A. Gupta, T. Shaw, J. Z. Sun, and M. B. Ketchen, "Paring Symmetry and Flux Quantization in a Tricrystal Superconducting Ring of $YBa_2O_{7-\delta}$," *Phys. Rev. Lett.*, vol. 73, no. 4, pp. 593-596, 1994.

[55] A. Mathai, Y. Gim, R. C. Black, A. Amar, and F. C. Wellstood, "Experimental proof of a time-reversal-invariant order parameter with a π shift in $YBa_2Cu_3O_{7-\delta}$," *Phys. Rev. Lett.*, vol. 74, no. 22, pp. 4523-4526, 1995.

[56] J. R. Kirtley, C. C. Tsuei, J. Z. Sun, C. C. Chi, L. S. Yu-Jahnes, A. Gupta, M. Rupp, and M. B. Ketchen, "Symmetry of the order parameter in the high-T_c superconductor $YBa_2Cu_3O_{7-\delta}$," *Nature*, vol. 373, no. 6511, pp. 225-228, 1995.

[57] J. H. Miller, Q. Y. Ying, Z. G. Zou, N. Q. Fan, J. H. Xu, M. F. Davis, and J. C. Wolfe, "Use of Tricrystal Junctions to Probe the Pairing State Symmetry of Yba2Cu3O7-Delta," *Phys. Rev. Lett.*, vol. 74, no. 12, pp. 2347-2350, 1995.

[58] Y. Gim, A. Mathai, R. C. Black, A. Amar, and F. C. Wellstood, "Angular dependence of the symmetry of the order parameter in $YBa_2Cu_3O_{7-\delta}$," *IEEE Trans. Appl. Supercond.*, vol. 7, no. 2, pp. 2331-2334, 1997.

[59] J. R. Kirtley, C. C. Tsuei, and K. A. Moler, "Temperature dependence of the half-integer magnetic flux quantum," *Science*, vol. 285, no. 5432, pp. 1373-1375, 1999.

[60] R. R. Schulz, B. Chesca, B. Goetz, C. W. Schneider, A. Schmehl, H. Bielefeldt, H. Hilgenkamp, J. Mannhart, and C. C. Tsuei, "Design and realization of an all d-wave dc pi-superconducting quantum interference device," *Appl. Phys. Lett.*, vol. 76, no. 7, pp. 912-914, 2000.

[61] B. Chesca, R. R. Schulz, B. Goetz, C. W. Schneider, H. Hilgenkamp, and J. Mannhart, "d-wave induced zero-field resonances in dc pi-superconducting quantum interference devices," *Phys. Rev. Lett.*, vol. 88, no. 17 2002.

[62] B. Chesca and R. Kleiner, "Order parameter phase sensitive experiments and SDJ dc SQUIDs," *Physica C*, vol. 357, pp. 1561-1566, 2001.

[63] J. M. Wheatley, T. C. Hsu, and P. W. Anderson, "Interlayer Effects in High-Tc Superconductors," *Nature*, vol. 333, no. 6169, p. 121, 1988.

[64] J. R. Kirtley, K. A. Moler, G. Villard, and A. Maignam, "c-Axis penetration depth of Hg-1201 single crystals," *Phys. Rev. Lett.*, vol. 81, no. 10, pp. 2140-2143, 1998.

[65] K. A. Moler, J. R. Kirtley, D. G. Hinks, T. W. Li, and M. Xu, "Images of Interlayer Josephson Vortices in $Tl_2Ba_2CuO_{6-\delta}$," *Science*, vol. 179, pp. 1193-1196, 1998.

[66] J. R. Kirtley, K. A. Moler, J. A. Schlueter, and J. M. Williams, "Inhomogeneous interlayer Josephson coupling in kappa-(BEDT-TTF)(2)Cu(NCS)(2)," *Journal of Physics-Condensed Matter*, vol. 11, no. 8, pp. 2007-2016, 1999.

[67] K. A. Moler, J. R. Kirtley, R. X. Liang, D. A. Bonn, W. N. Hardy, J. M. Williams, J. A. Schlueter, D. Hinks, G. Villard, A. Maignan, M. Nohara, and H. Takagi, "Images of interlayer Josephson vortices in single-layer cuprates," *Physica C*, vol. 341, pp. 977-980, 2000.

[68] P. W. Anderson, "The Resonating Valence Bond State in La2Cuo4 and Superconductivity," *Science*, vol. 235, no. 4793, pp. 1196-1198, 1987.

[69] D. A. Bonn, J. C. Wynn, B. W. Gardner, Y. J. Lin, R. Liang, W. N. Hardy, J. R. Kirtley, and K. A. Moler, "A limit on spin-charge separation in high-T-c superconductors from the absence of a vortex-memory effect," *Nature*, vol. 414, no. 6866, pp. 887-889, 2001.

[70] J. C. Wynn, D. A. Bonn, B. W. Gardner, Y. J. Lin, R. X. Liang, W. N. Hardy, J. R. Kirtley, and K. A. Moler, "Limits on spin-charge separation from h/2e fluxoids in very underdoped YBa2Cu3O6+x," *Phys. Rev. Lett.*, vol. 8719, no. 19, p. art-197002, 2001.

[71] Z. A. Xu, N. P. Ong, Y. Wang, T. Kakeshita, and S. Uchida, "Vortex-like excitations and the onset of superconducting phase fluctuation in underdoped La2-xSrxCuO4," *Nature*, vol. 406, no. 6795, pp. 486-488, 2000.

[72] I. Iguchi, T. Yamaguchi, and A. Sugimoto, "Diamagnetic activity above T-c as a precursor to superconductivity in La2-xSrxCuO4 thin films," *Nature*, vol. 412, no. 6845, pp. 420-423, 2001.

[73] M. Jamet, W. Wernsdorfer, C. Thirion, D. Mailly, V. Dupuis, P. Melinon, and A. Perez, "Magnetic anisotropy of a single cobalt nanocluster," *Phys. Rev. Lett.*, vol. 86, no. 20, pp. 4676-4679, 2001.

[74] S. I. Woods, J. R. Kirtley, S. H. Sun, and R. H. Koch, "Direct investigation of superparamagnetism in Co nanoparticle films," *Phys. Rev. Lett.*, vol. 8713, no. 13, p. art-137205, 2001.

[75] Black R.C., "Magnetic Microscopy using a Superconducting Quantum Interference Device." PhD University of Maryland, 1995.

[76] R. C. Black, A. Mathai, F. C. Wellstood, E. Dantsker, A. H. Miklich, D. T. Nemeth, J. J. Kingston, and J. Clarke, "Magnetic Microscopy Using A Liquid-Nitrogen Cooled Yba2Cu3O7 Superconducting Quantum Interference Device," *Appl. Phys. Lett.*, vol. 62, no. 17, pp. 2128-2130, 1993.

[77] R. C. Black, F. C. Wellstood, E. Dantsker, A. H. Miklich, J. J. Kingston, D. T. Nemeth, and J. Clarke, "Eddy-Current Microscopy Using A 77-K Superconducting Sensor," *Appl. Phys. Lett.*, vol. 64, no. 1, pp. 100-102, 1994.

[78] R. C. Black, F. C. Wellstood, E. Dantsker, A. H. Miklich, D. Koelle, F. Ludwig, and J. Clarke, "Imaging Radiofrequency Fields Using A Scanning Squid Microscope," *Appl. Phys. Lett.*, vol. 66, no. 10, pp. 1267-1269, 1995.

[79] R. C. Black, F. C. Wellstood, E. Dantsker, A. H. Miklich, D. T. Nemeth, D. Koelle, F. Ludwig, and J. Clarke, "Microwave Microscopy Using A Superconducting Quantum Interference Device," *Appl. Phys. Lett.*, vol. 66, no. 1, pp. 99-101, 1995.

[80] F. C. Wellstood, Y. Gim, A. Amar, R. C. Black, and A. Mathai, "Magnetic microscopy using SQUIDs," *IEEE Trans. Appl. Supercond.*, vol. 7, no. 2, pp. 3134-3138, 1997.

[81] "Magma-C1 Scanning HTS SQUID microscope, Neocera, Inc., 10000 Virginia Manor Road, Beltsville, MD 20705,"US Patent No. 5491411, 1995.

[82] S. Chatraphorn, E. F. Fleet, F. C. Wellstood, L. A. Knauss, and T. M. Eiles, "Scanning SQUID microscopy of integrated circuits," *Appl. Phys. Lett.*, vol. 76, no. 16, pp. 2304-2306, 2000.

[83] S. Chatraphorn, E. F. Fleet, F. C. Wellstood, and R. C. Black, "Imaging high-frequency magnetic and electric fields using a high-T-c SQUID microscope," *IEEE Trans. Appl. Supercond.*, vol. 9, no. 2, pp. 4381-4384, 1999.

[84] L. A. Knauss, A. B. Cawthorne, N. Lettsome, S. Kelly, S. Chatraphorn, E. F. Fleet, F. C. Wellstood, and W. E. Vanderlinde, "Scanning SQUID microscopy for current imaging," *Microelectronics Reliability*, vol. 41, no. 8, pp. 1211-1229, 2001.

[85] T. S. Lee, Y. R. Chemla, E. Dantsker, and J. Clarke, "High-T-c SQUID microscope for room temperature samples," *IEEE Trans. Appl. Supercond.*, vol. 7, no. 2, pp. 3147-3150, 1997.

[86] Y. R. Chemla, H. L. Crossman, Y. Poon, R. McDermott, R. Stevens, M. D. Alper, and J. Clarke, "Ultrasensitive magnetic biosensor for homogeneous immunoassay," *Proceedings of the National Academy of Sciences of the United States of America*, vol. 97, no. 26, pp. 14268-14272, 2000.

[87] Y. R. Chemla, H. L. Grossman, T. S. Lee, J. Clarke, M. Adamkiewicz, and B. B. Buchanan, "A New Investigation of Bacterial Motion: Superconducting Quantum Interference Device Microscopy of Magnetotactic Bacteria," *Biophys. J.*, vol. 76, pp. 3323-3330, 1999.

[88] H. L. Grossman, Y. R. Chemla, T. S. Lee, J. Clarke, M. Adamkiewicz, and B. B. Buchanan, "Squid detection of magnetic bacteria," *Biophys. J.*, vol. 78, no. 1, p. 267A, 2000.

[89] H. L. Grossman, W. R. Myers, V. J. Vreeland, R. Bruehl, M. D. Alper, C. R. Bertozzi, and J. Clarke, "Detection of bacteria in suspension by using a superconducting quantum interference device," *Proceedings of the National Academy of Sciences of the United States of America*, vol. 101, no. 1, pp. 129-134, 2004.

[90] F. Baudenbacher, N. T. Peters, P. Baudenbacher, and J. P. Wikswo, "High resolution imaging of biomagnetic fields generated by action currents in cardiac tissue using a LTS-SQUID microscope," *Physica C: Super.*, vol. 368, no. 1-4, pp. 24-31, Mar.2002.

[91] Baudenbacher F., Fong L.E., Thiel G., Wacke M., Jazbinsek V., Holzer J.R., Stampfl A., and Trontelj Z., "Intracellular Axial Current in Chara corallina Reflects the Altered Kinetics of Ions in Cytoplasm under the Influence of Light," *Biophys. J.*, 2004.

[92] J. R. Holzer, L. E. Fong, V. Y. Sidorov, J. P. Wikswo, Jr., and F. Baudenbacher, "High Resolution Magnetic Images of Planar Wave Fronts Reveal Bidomain Properties of Cardiac Tissue," *Biophys. J.*, vol. 87, no. 6, pp. 4326-4332, Dec.2004.

[93] H. Weinstock, "Prospects on the Application of Hts Squid Magnetometry to Nondestructive Evaluation (Nde)," *Physica C*, vol. 209, no. 1-3, pp. 269-272, 1993.

[94] H. Weinstock, "A Review of Squid Magnetometry Applied to Nondestructive Evaluation," *IEEE Trans. Mag.*, vol. 27, no. 2, pp. 3231-3236, 1991.

[95] G. B. Donaldson, "SQUIDS for Everything Else," in *Superconducting Electronics*. W. Weinstock and M. Nisenoff, Eds. Berlin/Heidelberg: Springer-Verlag, 1989, pp. 175-207.

[96] A. Cochran, G. B. Donaldson, L. N. C. Morgan, R. M. Bowman, and K. J. Kirk, "Squids for Ndt - the Technology and Its Capabilities," *British Journal of Non-Destructive Testing*, vol. 35, no. 4, pp. 173-182, 1993.

[97] U. Klein, M. E. Walker, C. Carr, D. M. McKirdy, C. M. Pegrum, G. B. Donaldson, A. Cochran, and H. Nakane, "Integrated low-temperature superconductor SQUID gradiometers for nondestructive evaluation," *IEEE Trans. Appl. Supercond.*, vol. 7, no. 2, pp. 3037-3039, 1997.

[98] U. Klein, M. E. Walker, C. Carr, D. M. McKirdy, C. M. Pegrum, G. B. Donaldson, A. Cochran, and H. Nakane, "Integrated low-temperature superconductor SQUID gradiometers for nondestructive evaluation," *IEEE Trans. Appl. Supercond.*, vol. 7, no. 2, pp. 3037-3039, 1997.

[99] D. M. McKirdy, A. Cochran, A. Mcnab, and G. B. Donaldson, *Using SQUIDs to solve some current problems in eddy current testing* 1995, pp. 1515-1518.

[100] J. P. Wikswo, Jr., "SQUID Magnetometers for Biomagnetism and Nondestructive Testing: Important Questions and Initial Answers," *IEEE Trans. Appl. Supercond.*, vol. 5, no. 2, Pt.1, pp. 74-120, 1995.

[101] J. P. Wikswo, Jr., "High-resolution magnetic imaging: Cellular action currents and other applications," in *SQUID Sensors: Fundamentals, Fabrication and Applications*. H. Weinstock, Ed. The Netherlands: Kluwer Academic Publishers, 1996, pp. 307-360.

[102] W. G. Jenks, S. S. H. Sadeghi, and J. P. Wikswo, Jr., "SQUIDs for nondestructive evaluation," *J. Phys. D: Appl. Phys.*, vol. 30, no. 3, pp. 293-323, 1997.

[103] J. P. Wikswo, Jr., "Applications of SQUID magnetometers to biomagnetism and nondestructive evaluation," in *Applications of Superconductivity*. H. Weinstock, Ed. Netherlands: Kluwer Academic Publishers, 2000, pp. 139-228.

[104] A. Abedi and J. P. Wikswo, Jr., "SQUID Magnetometers for Quantitative Measurements of Corrosion in Aluminum," 2000.

[105] A. Abedi and J. P. Wikswo, Jr., "SQUID Magnetometers and an Inverse Model for Quantification of Hidden Corrosion," in *PIERS 2000 : Progress in Electromagnetics Research Symposium : proceedings* Cambridge, MA: Electromagnetics Academy, 2000, p. 562.

[106] Y. P. Ma, J. P. Wikswo, and G. Fitzpatrick, "SQUID Measurements of Magnetization for a Magnetically Tagged Composite Material," *Review of Progress in Quantitative Nondestructive Evaluation*, vol. 20A, pp. 1831-1836, 2001.

[107] Y. P. Ma, J. P. Wikswo, M. Samuleviciene, K. Leinartas, and E. Juzeliunas, "Magnetic Fields Induced by Electrochemical Reactions: Aluminum Alloy Corrosion Sensing by SQUID Magnetometry on a Macroscopic Scale," *Journal of Physical Chemistry B*, vol. 106, no. 48, pp. 12549-12555, 2002.

[108] A. Abedi, J. J. Fellenstein, A. J. Lucas, and J. P. Wikswo, "A superconducting quantum interference device magnetometer system for quantitative analysis and imaging of hidden corrosion activity in aircraft aluminum structures," *Rev. Sci. Instrum.*, vol. 70, no. 12, pp. 4640-4651, 1999.

[109] B. P. Weiss, J. L. Kirschvink, F. J. Baudenbacher, H. Vali, N. T. Peters, F. A. Macdonald, and J. P. Wikswo, "A low temperature transfer of ALH84001 from Mars to Earth," *Science*, vol. 290, no. 5492, pp. 791-795, 2000.

[110] B. P. Weiss, F. J. Baudenbacher, J. P. Wikswo, and Kirschvink J.L., "Magnetic Microscopy Promises a Leap in Sensitivity and Resolution," *Eos Trans. AGU*, vol. 82, pp. 513-518, 2001.

[111] B. P. Weiss, H. Vali, F. J. Baudenbacher, J. L. Kirschvink, S. T. Stewart, and D. L. Shuster, "Records of an ancient Martian magnetic field in ALH84001," *Earth and Planetary Science Letters*, vol. 201, no. 3-4, pp. 449-463, 2002.

[112] F. Baudenbacher, L. E. Fong, G. Thiel, M. Wacke, V. Jazbinsek, J. R. Holzer, A. Stampfl, and Z. Trontelj, "Intracellular axial current in Chara corallina reflects the altered kinetics of ions in cytoplasm under the influence of light," *Biophys. J.*, vol. 88, no. 1, pp. 690-697, 2005.

[113] I. K. Kominis, T. W. Kornack, J. C. Allred, and M. V. Romalis, "A subfemtotesla multichannel atomic magnetometer," *Nature*, vol. 422, no. 6932, pp. 596-599, 2003.

[114] J. P. Wikswo, "SQUIDs remain best tools for measuring brain's magnetic field," *Physics Today*, vol. 57, no. 2, pp. 15-17, 2004.

[115] Landau L.D. and Ginzburg V.L., "On the theory of superconductivity," *Journal of Experimental and Theoretical Physics (U. S. S. R.)*, vol. 20, p. 1064, 1950.

[116] Landau L.D., *Collected Papers of L D Landau*. New York: Gordon and Breach, 1965.

[117] Meissner W. and Ochsenfeld R., "A new effect in penetration of superconductors," *Die Naturwissenschaften*, vol. 21, pp. 787-788, 1933.

[118] B. D. Josephson, "Discovery of Tunnelling Supercurrents," *Reviews of Modern Physics*, vol. 46, no. 2, pp. 251-254, 1974.

[119] B. D. Josephson, "Discovery of Tunneling Supercurrents," *Science*, vol. 184, no. 4136, pp. 527-530, 1974.

[120] P. W. Anderson and J. M. Rowell, *Phys. Rev. Lett.*, vol. 10, p. 230, 1963.

[121] S. Shapiro, *Phys. Rev. Lett.*, vol. 11, p. 80, 1963.

[122] W. C. Stewart, "Current-Voltage Characteristics of Josephson Junctions," *Appl. Phys. Lett.*, vol. 12, no. 8, p. 277-&, 1968.

[123] D. E. Mccumber, "Effect of Ac Impedance on Dc Voltage-Current Characteristics of Superconductor Weak-Link Junctions," *J. Appl. Phys.*, vol. 39, no. 7, p. 3113-&, 1968.

[124] J. C. Gallop, *SQUIDs, the Josephson Effects and superconducting electronics*. Portland, OR: Institute of Physics Publishing, 1991.

[125] V. Ambegaok and B. I. Halperin, "Voltage Due to Thermal Noise in Dc Josephson Effect," *Phys. Rev. Lett.*, vol. 22, no. 25, p. 1364-&, 1969.

[126] K. K. Likharev and V. K. Semenov, "Fluctuation Spectrum in Superconducting Point Junctions," *Jetp Letters-Ussr*, vol. 15, no. 10, p. 442-&, 1972.

[127] A. N. Vystavki, V. N. Gubankov, L. S. Kuzmin, K. K. Likharev, V. V. Migulin, and V. K. Semenov, "S-C-S Junctions As Nonlinear Elements of Microwave Receiving Devices," *Revue de Physique Appliquee*, vol. 9, no. 1, pp. 79-109, 1974.

[128] J. Clarke, W. M. Goubau, and M. B. Ketchen, "Tunnel Junction Dc Squid - Fabrication, Operation, and Performance," *J. Low Temp. Phys.*, vol. 25, no. 1-2, pp. 99-144, 1976.

CHAPTER III

OPTIMIZATION, DESIGN AND CHARAZTERIZATION OF SQUIDS

3.1 Noise in DC SQUIDs

The noise of low-*Tc* dc SQUIDs was first investigated by Tesche and Clarke [1]. They found that the dc SQUID was relatively insensitive to asymmetries in the inductance of the two arms, the critical currents, the shunt resistances and the capacitance of the junctions. For illustrational purposes, I present a noise study of a symmetrical dc SQUID with noise sources [2]. A diagram of this configuration is shown in Fig. 3.1. This diagram shows two independent Nyquist noise current sources, $I_{n1}(t)$ and $I_{n2}(t)$, associated with each shunt resistor. Since we consider a symmetrical configuration, each arm has an inductance of $L/2$.

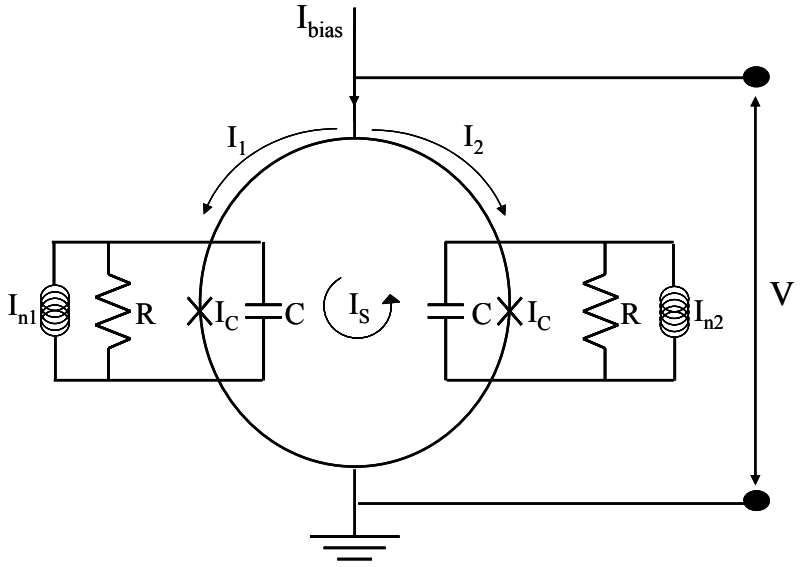

Figure 3.1: Schematic of a dc SQUID including noise sources.

The constant bias current is I_{BIAS}, and the currents in each arm are I_1 and I_2.

$$I_{BIAS} = I_1 + I_2 \tag{3.1}$$

The screening current, I_S, is defined as:

$$I_S = \frac{I_2 - I_1}{2} \tag{3.2}$$

Using the dc and ac Josephson equations (2.1, 2.2), the current in each arm is given by

$$I_1 = I_C \sin\delta_1 + I_{n1} + \frac{V_1}{R} + C\frac{dV_1}{dt} \tag{3.3}$$

and

$$I_2 = I_C \sin\delta_2 + I_{n2} + \frac{V_2}{R} + C\frac{dV_2}{dt} \tag{3.4}$$

The phase differences across each junction are given by

$$\frac{d\delta_1}{dt} = \frac{2e}{\hbar}V_1 \tag{3.5}$$

and

$$\frac{d\delta_2}{dt} = \frac{2e}{\hbar}V_2 \tag{3.6}$$

From equations (3.1) and (3.2) it can be shown that:

$$\frac{dI_S}{dt} = -\frac{dI_1}{dt} = \frac{dI_2}{dt} \tag{3.7}$$

The total voltage, V, across the SQUID is:

$$V = V_1 + \frac{L}{2}\frac{dI_1}{dt} \tag{3.8}$$

and

$$V = V_2 + \frac{L}{2}\frac{dI_2}{dt} \tag{3.9}$$

The phase differences across the junctions are related by [3]

$$\delta_1 - \delta = \frac{2\pi\Phi}{\Phi_0} \tag{3.10}$$

and the total flux in the loop is:

$$\Phi = \Phi_{ext} + LI_S \tag{3.11}$$

Equations (3.1) to (3.11) can be combined to produce the following set of equations:

$$V = \frac{\hbar}{4e}\left(\frac{d\delta_1}{dt} - \frac{d\delta_2}{dt}\right) \tag{3.12}$$

$$I_S = \frac{\Phi_0}{2\pi L}\left(\delta_1 - \delta_2 - \frac{2\pi\Phi_{ext}}{\Phi_0}\right) \tag{3.13}$$

$$\frac{\hbar C}{2e}\frac{d^2\delta_1}{dt^2} + \frac{\hbar}{2eR}\frac{d\delta_1}{dt} = \frac{I}{2} - I_S - I_C \sin\delta_1 - I_{n1} \tag{3.14}$$

$$\frac{\hbar C}{2e}\frac{d^2\delta_2}{dt^2} + \frac{\hbar}{2eR}\frac{d\delta_2}{dt} = \frac{I}{2} + I_S - I_C \sin\delta_2 - I_{n1} \tag{3.15}$$

These equations were solves numerically by Tesche and Clarke [1] for a range of values of Γ, β_C and β_L, where β_L is the reduced inductance parameter given by

$$\beta_L = \frac{2I_C L}{\Phi_0} \tag{3.16}$$

In the limit where the thermal energy is much smaller than the Josephson coupling energy (see equation 2.12), Γ is related to the size of the critical current modulation, ΔI_m, by

$$\Delta I_m = \frac{2I_C}{1+\beta_L} \tag{3.17}$$

The magnetic flux noise of a SQUID, Φ_n, as a function of frequency is given by

$$\Phi_n(f) = \left(S_\Phi(f)\right)^{1/2} = \frac{\left(S_V(f)\right)^{1/2}}{\left(V_\Phi\right)} \tag{3.18}$$

where $S_\Phi(f)$ and $S_V(f)$ are the spectral densities of flux and voltage noise respectively. From numerical simulations [4], the maximum value of V_Φ occurs when $\Phi = (2n+1)\Phi_o/4$ and the optimum value of β_L for low noise operation is $\beta_L \approx 1$. This gives a spectral density that is white below typical flux-locked loop (FLL) modulation frequencies [5].

For an optimized SQUID with $\beta_L = 1$, $\Gamma = 0.05$, $\Phi = (2n+1)\Phi_o/4$ and I_{BIAS} set at the value for maximum modulation voltage, V_Φ, the following equations were obtained [4]:

$$V_\Phi \approx \frac{R}{L} \tag{3.19}$$

$$S_V(f) \approx 16k_B TR \tag{3.20}$$

$$S_\Phi(f) \approx \frac{16k_B TL^2}{R} \tag{3.21}$$

We can now easily identify that L should be reduced and R increased to reduce the noise of the SQUID. But the maximum value of R is still restricted by the parameter β_C to avoid hysteretic behavior that will affect the noise performance of the SQUID.

At low frequencies, the flux noise of a SQUID has a $1/f$ dependence. There are two effects responsible for this: the motion of flux trapped in the SQUID body [6] and the critical current fluctuations in the junctions [7]. The second one arises from electron being trapped by defects in the junctions and then being released. While the electron is trapped, the height of the potential barrier changes and this alters the critical current density in the region of the defect. The switching between the two states is random but a $1/f$ noise spectrum is obtained when a few trapping defects are present.

The spectral density of the $1/f$ voltage noise $S_V(f)$ at constant bias current can be approximated by the sum of two terms [4]:

$$S_V(f) \approx \frac{1}{2}\left[\left(\frac{dV}{dI_C}\right) + L^2\left(V_\Phi\right)^2\right] S_{I_C}(f) \tag{3.22}$$

where S_{I_C} is the spectral density of critical current noise and is assumed to be the same for each junction. The first term on the right is the "in-phase" mode caused by the junctions producing fluctuations in the same direction. The second term is the "out-of-phase" mode where the fluctuations of the junctions are opposite polarity and create a circulating current. The "in-phase" mode is removed by the FLL modulation scheme and the effect of the critical current "out-of-phase" mode by implementing a bias reversal scheme [8].

3.2. SQUID optimization and design for low-Tc RT-sample SQUID microscopy

The evident goal in the development of SQUID microscopy is to get the closest possible to the sample with the highest sensitivity and spatial resolution sensor possible. Nevertheless, since what the SQUID detects is the magnetic flux (the integration of the field strength *B* on the sensing area *A*), with the miniaturization of the SQUID sensor there is a corresponding loss in sensitivity to magnetic fields, and vice-versa: the enhancement of field sensitivity diminishes the spatial resolution of the system. Thus, the overall final goal of SQUID microscopy results in a Catch-22 kind of situation. However, the performance of SQUID microscopy is not just governed by the improvements of spatial resolution and sensitivity of the SQUID sensor, but also by the fall-off rate of the magnetic field of the sources intended to be measured.

Following Wikswo's approach [9], magnetic field sources can be classified as: current-carrying wire sources, where the magnetic field strength is proportional to 1/*a* (where *a* is the distance from the source to the sensor); current dipolar sources immersed in a conducting medium (typical of corrosion or bioelectric systems), where the magnetic field is proportional to

$1/a^2$, and magnetic dipolar sources where the magnetic field is proportional to $1/a^3$. With this in mind, the sensitivity of system can be specified in terms of a noise-equivalent source defined as the minimum detectable source per unit of bandwidth. In this way, we have a minimum detectable current, I_{min}; minimum detectable current dipole in a conducting medium, p_{min}; and minimum detectable magnetic dipole, m_{min}. The main advantage of this approach is that it allows for the comparison of different magnetometer configurations in terms of the sources being studied.

Several quantitative analysis of magnetic imaging [9-17] have shown that a SQUID will achieve the best combination of spatial resolution and field sensitivity if the diameter of the sensing area, a, is approximately the same as the sensor-to-sample distance, r. Using this assumption, Wikswo *et al.* [9] came up with an elegant method to explore the trade-offs between sensitivity and spatial resolution for a specific magnetic source. Table 3.1 summarizes their results. From the results, we can conclude that applications like rock magnetism and paleomagnetism, where the sources behave as magnetic dipoles, will benefit the most from a small sensor close to the sample. In contrast, for typical fields associated to biomagnetism, where more sensitivity is required and the sources act as either axial currents or sheet of currents, bigger sensors at distances equal to the diameter of the sensor are the best trade-off.

The definition of the magnetic source of study is followed by the design and manufacturing of the specific SQUID sensor. As shown in previous sections, the two parameters generally used to optimize a dc SQUID sensor are the reduced inductance β_L and the hysteresis parameter β_C, also referred to as the Stewart-McCumber parameter:

$$\beta_L = \frac{2I_C L}{\Phi_o}, \beta_C = \frac{2\pi I_C R^2 C}{\Phi_o} \tag{3.23}$$

where I_C is the critical current , L is the SQUID inductance, C is the Josephson junction capacitance, R is the shunt resistance and Φ_o is the magnetic flux quantum. These parameters come from the analysis of the differential equations that govern the operation of the dc SQUID. β_L is a measure of the modulation depth of the maximum current at zero voltage, as a function of the applied flux. For $\beta_L >> 1$, the modulation depth becomes very small and for $\beta_L < 1$ the modulation depth approaches the limit of $2I_C$. The optimal performance occurs for $\beta_L \approx 1$. On the other hand, β_C is a measure of the damping of the Josephson junction. For $\beta_C \leq 0.7$, the IV characteristics of the SQUID are non-hysteretic and the average voltage across the SQUID for a given external flux is a single value. The idea of the optimization is to achieve the highest possible signal-to-noise ratio by modifying the SQUID inductance L, which is related to the geometry and dimensions of the SQUID body; the critical current I_C and the capacitance of the Josephson junction C, which are controlled by the physical dimensions and properties of the junction; and by choosing the proper shunt resistance R. For an optimized SQUID ($\beta_L \approx 1$ and $\beta_C \leq 0.7$), we can express the equivalent flux noise of the SQUID S_Φ, above very low frequencies, as a function independent of the frequency, as follow [1]:

$$S_\Phi(f) = \frac{16k_B TL^2}{R} = 16k_B TL\sqrt{\frac{\pi LC}{\beta_C}} \tag{3.24}$$

where f denotes the frequency, k_B the Boltzman constant, T the operational temperature, R the shunt resistance and L the inductance of the device.

Modern thin-film technology allows great versatility in SQUID parameters and fabrication. They are typically manufactured by sputtering of niobium thin films and patterning the films with photolithography or electron-beam lithography. In general, any superconducting material can be used to fabricate a SQUID, but generally, niobium technology is used for low-*Tc*

SQUIDs. The junction are fabricated using a trilayer process of $Nb/NbO_x/Pb$ or $Nb/Al_2O_3/Nb$, and the shunt resistances consist of a material that does not become superconducting at liquid He temperatures, generally copper, molybdenum or gold.

Table 3.1: The relationship between SQUID dimension *a*, the signal strength *S*, the SQUID noise *N*, and the minimum detectable source (*MDS*) for the three different types of sources. (Taken from 101)

Source	*S*	*N*	*S/N*	*MDS*
Wire	a^{-1}	$a^{-3/2}$	$a^{1/2}$	$a^{-1/2}$
Electric Dipole	a^{-2}	$a^{-3/2}$	$a^{-1/2}$	$a^{1/2}$
Magnetic Dipole	a^{-3}	$a^{-3/2}$	$a^{-3/2}$	$a^{3/2}$

3.3. Methods of SQUID characterization: V-I, V-Φ and noise measurements

During the characterization of a SQUID sensor, one measures the intrinsic parameters and assesses the noise performance of each device. The characterization procedure gives information about the homogeneity of the fabrication process and helps us to evaluate a particular design. In this way, we can adjust the fabrication process and/or make changes to the device itself aiming to improve its performance.

The first step is to measure the V-I characteristic. Figure 3.2(a) shows a schematic of the set up and a typical V-I curve. We apply a periodic time-varying signal (in this case a triangular waveform) and measure the output voltage. The SQUID is superconducting until the critical current is reached, when a voltage drop then appears. From this plot, we can obtain information about the shunt resistance *R* and the critical current I_C. The next step is to measure the V-Φ characteristic. Figure 3.2(b) shows a schematic of the set up and a typical V-Φ curve. Now, we

apply the periodic time varying signal through the feedback line and measure the modulation voltage on the SQUID as a function of bias current I_B, until we reach the maximum modulation voltage, ΔV_{max}. From the V-Φ plot, we can estimate the maximum modulation voltage ΔV, which gives information about how steep the SQUID transfer function is, and also measure the coupling (mutual inductance M) between the SQUID and the integrated feedback line, $M = I/\Phi_o$.

The SQUID noise is mainly composed of Johnson noise. Since the Johnson noise has a stochastic nature, the measurement of the power spectral density (PSD) is a useful tool to characterize it. To measure the PSD, we operate the SQUID in the FLL mode and place it in a magnetically noise free environment. We then connect the output of the SQUID electronics to a spectrum analyzer and measure the power spectrum, usually in units of $V/\sqrt{Hz}$. In general, the SQUID power spectrum is characterized by a 1/f noise (Flicker noise) region at low frequencies, and by a white noise region starting from the 1/f knee up to the roll-off frequency of the feedback circuit (for details see section 3.1). For conventional niobium-based SQUIDs, the 1/f noise starts below frequencies of ~ 0.1 Hz. From the PSD we can estimate the noise in terms of energy ($J/Hz^{1/2}$), magnetic flux ($\Phi_o/Hz^{1/2}$), field ($T/Hz^{1/2}$) or field gradient ($T/(cm\ Hz^{1/2})$). Usually, energy and flux noise are figures of merit for the bare SQUID, while the field and the field gradient noise are figures of merit for the complete system. Figure 3.3 shows the field and flux noise spectral density of one of our SQUID sensors.

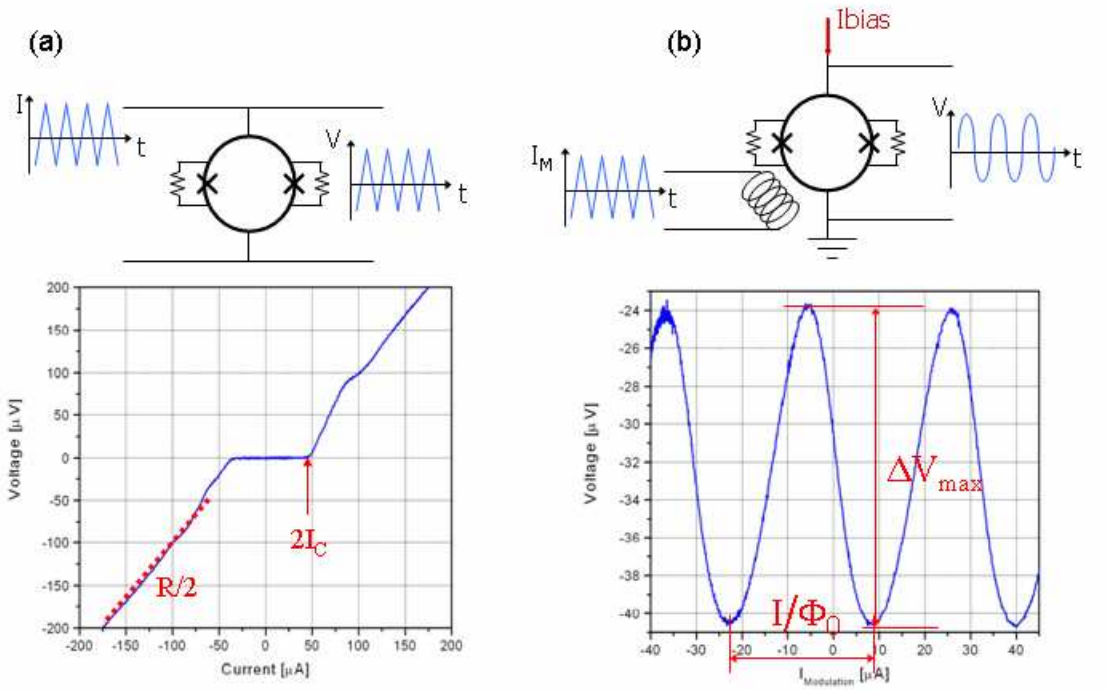

Figure 3.2: (a) Schematic of the measurement set up and its corresponding V-I characteristic curve. From the curve, we extract the critical current and the shunt resistance. (b) Schematic of the measurement set up and its corresponding V-Φ characteristic curve. From the curve, we extract the maximum modulation voltage ΔV_{max} and the coupling between the feedback coil and the SQUID, I/Φo.

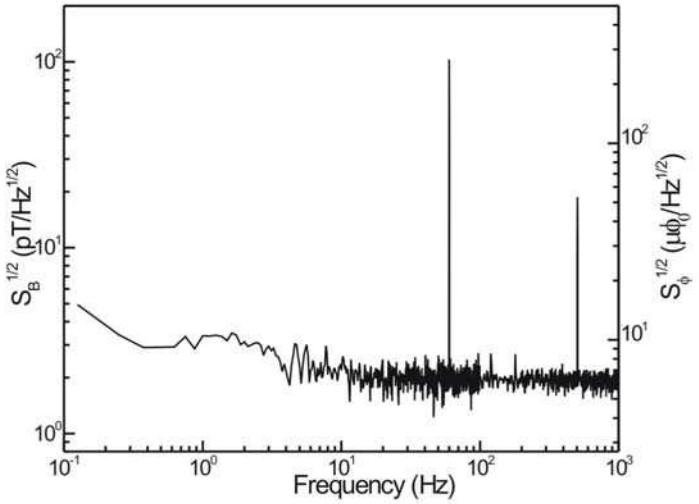

Figure 3.3: Field noise $S_B^{1/2}$ and flux noise $S_\Phi^{1/2}$ spectral density of one of our monolithic SQUID sensors

3.4 References

[1] C. D. Tesche and J. Clarke, "Dc Squid - Noise and Optimization," *J. Low Temp. Phys.*, vol. 29, no. 3-4, pp. 301-331, 1977.

[2] P. D. Colman, "Design, Characterization and Optimization of High-Tc DC SQUIDS." PhD University of Cambridge, 1997.

[3] J. E. Zimmerma and A. H. Silver, "Macroscopic Quantum Interference Effects Through Superconducting Point Contacts," *Physical Review*, vol. 141, no. 1, p. 367-&, 1966.

[4] J. Clarke, "SQUID fundamentals," in *SQUID Sensors: Fundamentals, Fabrication and Applications*. H. Weinstock, Ed. Netherlands: Kluwer Academic Publishers, 1996.

[5] J. Clarke, W. M. Goubau, and M. B. Ketchen, "Tunnel Junction Dc Squid - Fabrication, Operation, and Performance," *J. Low Temp. Phys.*, vol. 25, no. 1-2, pp. 99-144, 1976.

[6] R. H. Koch, J. Clarke, W. M. Goubau, J. M. Martinis, C. M. Pegrum, and D. J. Vanharlingen, "Flicker (1/F) Noise in Tunnel Junction Dc Squids," *J. Low Temp. Phys.*, vol. 51, no. 1-2, pp. 207-226, 1983.

[7] C. T. Rogers and R. A. Buhrman, "Composition of 1/F Noise in Metal-Insulator-Metal Tunnel-Junctions," *Phys. Rev. Lett.*, vol. 53, no. 13, pp. 1272-1275, 1984.

[8] M. B. Ketchen, W. M. Goubau, J. Clarke, and G. B. Donaldson, "Superconducting Thin-Film Gradiometer," *J. Appl. Phys.*, vol. 49, no. 7, pp. 4111-4116, 1978.

[9] J. P. Wikswo, Jr., "High-resolution magnetic imaging: Cellular action currents and other applications," in *SQUID Sensors: Fundamentals, Fabrication and Applications*. H. Weinstock, Ed. The Netherlands: Kluwer Academic Publishers, 1996, pp. 307-360.

[10] J. P. Wikswo, Jr., "High-Resolution Measurements of Biomagnetic Fields," in *Advances in Cryogenic Engineering*. R. W. Fast, Ed. Plenum Publishing, 1988, pp. 107-116.

[11] J. P. Wikswo, Jr. and B. J. Roth, "Magnetic Determination of the Spatial Extent of a Single Cortical Current Source: A Theoretical Analysis," *Electroencephalogr. Clin. Neurophysiol.*, vol. 69, pp. 266-276, 1988.

[12] B. J. Roth, N. G. Sepulveda, and J. P. Wikswo, Jr., "Using a Magnetometer to Image a Two-dimensional Current Distribution," *J. Appl. Phys.*, vol. 65, no. 1, pp. 361-372, 1989.

[13] S. Tan, B. J. Roth, and J. P. Wikswo, Jr., "The Magnetic Field of Cortical Current Sources: the Application of a Spatial Filtering Model to the Forward and Inverse Problems," *Electroencephalogr. Clin. Neurophysiol.*, vol. 76, pp. 73-85, 1990.

[14] S. Tan, "Linear systems imaging and its applications to magnetic measurements by SQUID magnetometers." PhD Vanderbilt University, 1992.

[15] S. Tan, Y. P. Ma, I. M. Thomas, and J. P. Wikswo, Jr., "High resolution SQUID imaging of current and magnetization distributions," *IEEE Trans. Appl. Supercond.*, vol. 3, no. 1, pp. 1945-1948, 1993.

[16] Staton D.J., "Magnetic imaging of applied propagating action currents in cardiac tissue slices: determination of anisotropic electrical conductivities in a two-dimensional bidomain." PhD Vanderbilt University, 1994.

[17] S. Tan, N. G. Sepulveda, and J. P. Wikswo, Jr., "A New Finite-Element Approach to Reconstruct a Bounded and Discontinuous Two-Dimensional Current Image from a Magnetic Field Map," *J. Comput. Phys.*, vol. 122, pp. 150-164, 1995.

CHAPTER IV

HIGH-RESOLUTION ROOM-TEMPERATURE SAMPLE SCANNING SUPERCONDUCTING QUANTUM INTERFERENCE DEVICE MICROSCOPE CONFIGURABLE FOR GEOLOGICAL AND BIOMAGNETIC APPLICATIONS

Luis E. Fong[1], Jenny R. Holzer[1], Krista McBride[1], Eduardo A. Lima[2], Masoud Radparvar[3], Franz Baudenbacher[2]

[1]Department of Physics and Astronomy
[2]Department of Biomedical Engineering
Vanderbilt University, Nashville, TN, 37235

[3]Hypres Inc., Elmsford, NY, 10523

Adapted from:
L. E. Fong, J. R. Holzer, K. McBride, E. A. Lima, M. Radparvar, F. Baudenbacher,
(Accepted for publication in *Review of Scientific Instruments)*
2005

4.1. Abstract

We have developed a scanning superconducting quantum interference device (SQUID) microscope system with interchangeable sensor configurations for imaging magnetic fields of room-temperature (RT) samples with sub-millimeter resolution. The low-critical-temperature (*Tc*) niobium-based SQUID sensors are mounted on the tip of a sapphire rod and thermally anchored to the helium reservoir inside the vacuum space of a cryostat. A 25 μm sapphire window separates the vacuum space from the RT sample. A positioning mechanism allows us to adjust the sample-to-sensor spacing from the top of the Dewar. We achieved a sensor-to-sample spacing of 100 μm, which could be maintained for periods of up to 4 weeks. Different SQUID sensor designs are necessary to achieve the best combination of spatial resolution and field sensitivity for a given source configuration. For imaging thin sections of geological samples, we used a custom-designed monolithic low-*Tc* niobium bare SQUID sensor, with an effective diameter of 80 μm, and achieved a field sensitivity of 1.5 $pT/Hz^{1/2}$ and a magnetic moment sensitivity of 5.4×10^{-18} $Am^2/Hz^{1/2}$ at a sensor-to-sample spacing of 100 μm in the white noise region for frequencies above 100 Hz. Imaging action currents in cardiac tissue requires a higher field sensitivity, which can only be achieved by compromising spatial resolution. We developed a monolithic low-*Tc* niobium multiloop SQUID sensor, with sensor sizes ranging from 250 μm to 1 mm, and achieved sensitivities of 480 – 180 $fT/Hz^{1/2}$ in the white noise region for frequencies above 100 Hz, respectively. For all sensor configurations, the spatial resolution was comparable to the effective diameter and limited by the sensor-to-sample spacing. Spatial registration allowed us to compare high-resolution images of magnetic fields associated with action currents and optical recordings of transmembrane potentials to study the bidomain nature

of cardiac tissue or to match petrography to magnetic field maps in thin sections of geological samples.

4.2. Introduction

Room-temperature (RT) sample scanning superconducting quantum interference device (SQUID) microscopy (SSM) is a very powerful and promising technique for imaging magnetic field distributions [1,2]. In addition to the SQUID's unsurpassed field sensitivity, this technique is completely non-invasive and can be implemented to study a great variety of samples. RT sample SSM is continuing to play an important role in biomagnetism [3-8], non-destructive evaluation [9-14] and geomagnetism [15,16].

Since the field and spatial resolution are highly diminished as the distance between the sample and the sensor increases, the key to this technique is to bring the sensor, held at cryogenic temperatures, as close as possible to the sample. It has been shown that the best combination of spatial resolution and field sensitivity for a specific SQUID geometry occurs when the diameter of the pickup coil is approximately equal to the sample-to-sensor distance [17].

A SQUID sensor measures the integrated magnetic flux over the sensing area. Thus, the SQUID's sensitivity to magnetic fields scales as $1/a^2$, where a is the diameter of the sensing area. The fall-off rate of the magnetic field depends on the type of source. For a current-carrying wire the field scales as $1/r$, and for a magnetic dipole it scales as $1/r^3$, where r is the distance from the source. The best combination of field sensitivity and spatial resolution requires $a = r$. It is easy to show that the signal-to-noise ratio of fields generated by a current-carrying wire is proportional to a and for a magnetic dipole, proportional to $1/a$. Therefore, we have to use

different strategies to optimize the sensor geometry and the sample-to-sensor distance depending on the application. In geomagnetism we are dealing with magnetic dipoles, while biomagnetic signals are typically generated by either axial currents or sheets of current.

In this article, we describe a high-resolution SQUID imaging system that can be configured either with monolithic low-*Tc* directly coupled single turn SQUIDs, multiloop SQUIDs, or miniature pickup coils inductively coupled to commercial low-*Tc* SQUIDs, as sensing elements for different applications. The system is highly stable, user friendly and cost efficient. The system versatility is demonstrated by presenting data on high-resolution magnetic imaging of geological thin sections and magnetic mapping of action current distributions in cardiac tissue.

4.3. Scanning SQUID microscope system design

In the following sections, we present various designs for directly coupled monolithic SQUID sensors, targeting spatial resolutions ranging from 50 μm to 1 mm, their device characteristics, and their incorporation into our SQUID microscope. We also describe a positioning mechanism, which allows the cryogenic sensors to be positioned within 10 μm of a RT sapphire window, and our Dewar design which allows operation of the SQUID microscope with a helium consumption of 1.0 *l*/day.

4.3.1. Directly coupled monolithic SQUID sensors

Our first generation of SQUID microscopes used hand-wound superconducting niobium-wire miniature pickup coils connected directly to the terminals of a flux transformer circuit of commercially available low-*Tc* SQUID sensors [18]. With this configuration (Fig. 4.1), we achieved field sensitivities, for frequencies above 1 Hz, of 850 fT/Hz$^{1/2}$ and 330 fT/Hz$^{1/2}$, using a

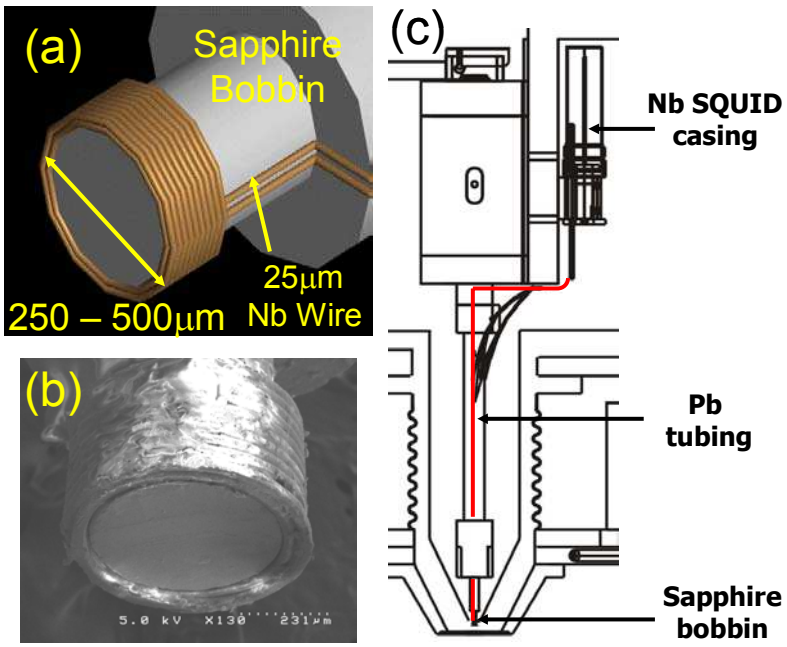

Figure 4.1: (a) Schematic of the 25 μm-Nb-wire hand-wound pickup coil. Typically, pickup coil diameters vary from 250 to 500 μm. (b) SEM image of a double layer 500 μm pickup coil. (c) Cross-sectional schematic of the miniature pickup coil configuration. The pick up coil is inductively coupled to a SQUID hosted inside a Nb casing. The coil leads are twisted and threaded through a thin Pb tube from the pickup coil into the Nb casing.

10-turn 250 μm diameter and a 20-turn 500 μm diameter pickup coil, respectively. However, the miniature pickup coil configuration has two major drawbacks in accomplishing the optimum combination of field sensitivity and spatial resolution. The first limitation is the impedance mismatch between the pickup coil and the flux transformer circuit. For optimum coupling, and therefore, the best possible magnetic field sensitivity, the flux transformer input coil and the pickup coil impedances must be the same. Commercially available low-*Tc* SQUID sensors typically have input coil impedances on the order of 2 μH, which is 20 times higher than the impedance of a 20-turn 500 μm pickup coil. Impedance matching is increasingly difficult as we reduce the pickup coil size and is impractical for spatial resolutions below 250 μm. The second limitation is the spatial integration of the magnetic field over the volume of the pickup coil. For

example, a 20-turn double layer cylindrical coil wound with a 25 μm wire has a minimal height of 250 μm. The taller the pickup coil, the less magnetic flux each turn collects, since the magnetic field decays as we increase the distance from the sample. This integration generally compromises the spatial resolution but leads to higher field sensitivity. However, in terms of sensitivity to dipole moments, a better signal to noise ratio can be achieved if a small coil is brought closer to the sample [19]. In this case, the limiting factor is generally the distance between the sample and the SQUID sensor.

To overcome these drawbacks, we developed different types of thin film monolithic low-*Tc* niobium SQUID sensors, which measure the magnetic field coupled directly into the self inductance of the SQUID. In the first type of sensor, a single SQUID washer acts as the sensing area. Detailed images and an equivalent circuit of this design are shown in Fig. 4.2. In this approach, the sensing area is a two dimensional plane rather than a volume, as in the case of the miniature hand-wound pickup coils. The noise performance of an optimized SQUID sensor is limited by its inductance and is described by the power spectral density of the equivalent flux noise [20]:

$$S_{\phi}(f) = \frac{16 k_B T L^2}{R_n}, \tag{1}$$

where f denotes the frequency, k_B the Boltzmann constant, T the operational temperature, R_n the shunt resistance and L the inductance of the device. The main contribution to the inductance is determined by the sensor size [21]. Therefore, the intrinsic noise of the bare SQUID increases with its geometrical size, so this approach cannot be scaled up to sensor diameters larger than 250 μm [22].

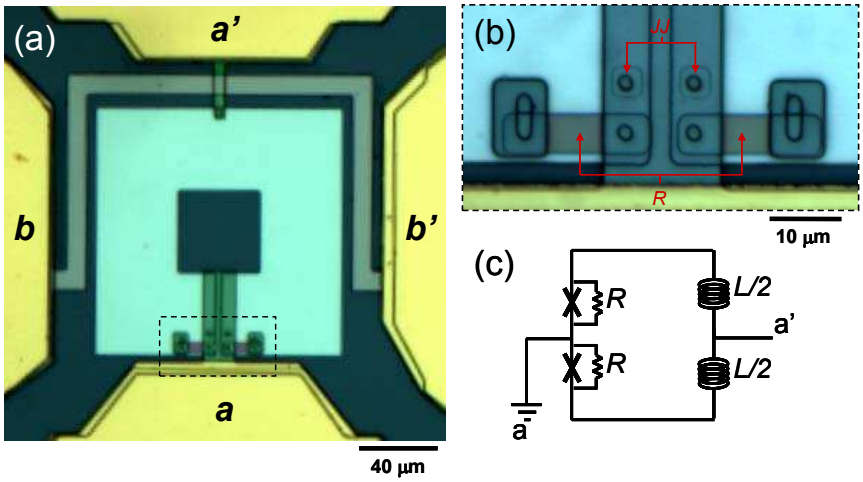

Figure 4.2: (a) Image of our bare SQUID design. The SQUID terminals are labeled ***a*** and ***a'*** and the contact pads for the feedback coil ***b*** and ***b'***. (b) Expanded view of the SQUID connection region. The Josephson Junctions are labeled *JJ* and the shunt resistances *R*. (c) Equivalent electric circuit diagram of the bare SQUID. *R* is the shunt resistance in parallel with the Josephson Junctions and *L* is the inductance of the device.

Using a bare SQUID with a 40 μm hole and a 120 μm square washer, we achieved a flux noise of 4 $\mu\phi_o/Hz^{1/2}$, where ϕ_0 is the magnetic flux quantum, and an equivalent field sensitivity of 1.5 $pT/Hz^{1/2}$ in the white noise region for frequencies above 100 Hz. The bare SQUID design is particularly suited for localized source configurations where the signal decreases rapidly with distance, as is the case for dipolar sources. As we mentioned before, the size of the SQUID washer should be chosen to be comparable to the sensor-to-sample distance for optimum tradeoff between spatial resolution and field sensitivity. The use of the bare SQUID for RT sample SSM is suited for spatial resolutions on the order of tens of microns to 250 μm. (Details of the design and optimization procedure for the bare SQUID are explained in Chapter V).

For imaging applications where higher field sensitivities are required, we have to compromise spatial resolution in order to achieve larger effective areas. This is especially true in the case of imaging weak magnetic fields generated by distributed action currents associated

with bioelectric phenomena. As we have outlined above, the size of the SQUID sensing area cannot be scaled up by using a bare SQUID design. Therefore, in order to overcome these limitations, we used a monolithic low-*Tc* niobium multiloop, or fractional turn, SQUID design. This approach was first implemented by Zimmerman in 1971 [23]. Figure 4.3 shows detailed images of the sensor and the equivalent circuit of one of our designs. The multiloop SQUID is comprised of multiple pickup coils connected in parallel, thereby reducing the self inductance of the SQUID sensor. In this way, the effective sensing area can be increased with little compromise of field sensitivity. Therefore, we have fabricated a series of multiloop SQUID sensors with diameters ranging from 250 μm to 1 mm. For a 250 μm diameter, 5-spoke multiloop SQUID, we achieved a flux noise of 1.7 $\mu\phi_o/Hz^{1/2}$ with an equivalent field sensitivity of 450 $fT/Hz^{1/2}$ in the white noise region for frequencies above 100 Hz [24]. For a larger diameter, we increased the number of spokes. Using a 500 μm, 6-spoke multiloop SQUID, we achieved a flux noise of 4.4 $\mu\phi_o/Hz^{1/2}$ with an equivalent field sensitivity of 240 $fT/Hz^{1/2}$ in the white noise region for frequencies above 100 Hz. The increased field sensitivity of the multiloop SQUID design makes it ideally suited for imaging magnetic fields associated with action current propagation in isolated tissue preparations. (Details of the design and optimization procedure for the multiloop SQUID are explained in Chapter VI). In comparison with the 250 μm miniature pickup coils, the field sensitivity is improved by a factor of two. Furthermore, by reducing the sensing volume to a single plane, we increased our signal-to-noise ratio and our spatial resolution. Table 1.1 summarizes the performance of our different sensing configurations. Table 1.2 shows a review of the magnetic field and spatial resolution range attainable with the new monolithic SQUID sensors and the possible applications where they are expected to play an important role.

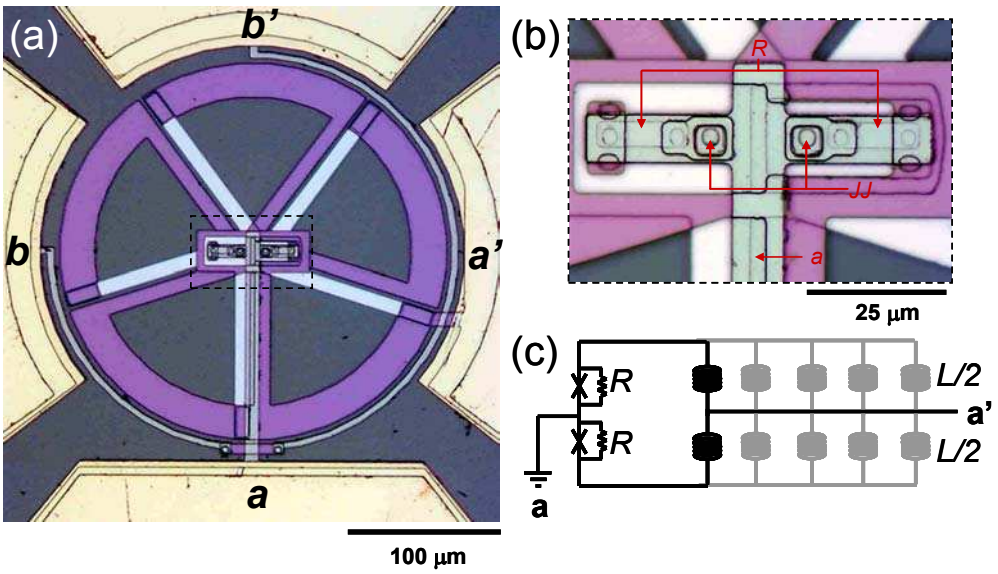

Figure 4.3: (a) Image of our multiloop SQUID design. ***a*** and ***a'*** are the SQUID terminals and *b* and *b'* the contact pads of the integrated feedback coil. (b) Expanded view of the center of the multiloop SQUID. The Josephson Junctions are labeled *JJ*, the shunt resistances *R* and the SQUID upper contacts ***a***, respectively. The purple and white regions represent the two superconducting layers forming each spoke, which are separated by an insulating layer in cross over regions. (c) Equivalent circuit diagram of the multiloop SQUID. *R* represents the shunt resistance in parallel with the *JJ* and *L* is the inductance of each individual spoke (fractional turn). The inductance of the device is inversely proportional to the number of spokes.

Table 4.1: Flux noise and field sensitivity of all our SQUID sensor configurations. $S_\phi^{1/2}(f)$ and $S_B^{1/2}(f)$ are the magnetic flux and field noise per unit bandwidth at the specified frequency.

Sensor Configuration	$S\phi^{1/2}$ (100Hz) ($\mu\phi_o/Hz^{1/2}$)	$S_B^{1/2}$ (1Hz) ($pT/Hz^{1/2}$)	$S_B^{1/2}$ (100Hz) ($pT/Hz^{1/2}$)	$S_B^{1/2}$ (1KHz) ($pT/Hz^{1/2}$)
Bare SQUID 40 μm washer 40 μm hole	4.0	3.5	1.52	1.50
Multiloop SQUID 250 μm diameter 5 spokes	1.7	2.1	0.48	0.45
Multiloop SQUID 500 μm diameter 6 spokes	4.4	1.85	0.28	0.24
Multiloop SQUID 1 mm diameter 8 spokes	6.0	0.94	0.18	0.15
Miniature coils 250 μm diameter 10 turns	2.0	0.85	0.85	0.85
Miniature coils 500 μm diameter 20 turns	2.0	0.33	0.33	0.33

Table 4.2: Review of our two current SQUID designs.

	Bare SQUID	Multiloop SQUID
Magnetic Source:	Magnetic dipolar sources	Spatially distributed current sources
Magnetic Field Resolution:	~ 1 pT	~ 100 fT
Spatial Resolution:	~ 100 μm	~ 250 μm
Possible Applications:	• Paleomagnetic studies • Rock magnetism • Detection of magnetic beads	• Biomagnetic studies • MCG • MEG • Cell electrophysiology

4.3.2. Cryogenic design

The SQUID Dewar provides the cryogenic temperatures and the thermal insulation which allows for operating a low-*Tc* SQUID in close proximity to a RT sample. A schematic of the SQUID Dewar is shown in Fig. 4.4. The cryogenic system is based on a commercially available custom built G-10 fiberglass Dewar (Infrared Laboratories, HDL-8). In order to achieve liquid He and N_2 hold times of three days, we used 4.96 *l* He and 5.88 *l* N_2 reservoirs in our Dewar. The N_2 reservoir is stacked over the He reservoir. An aluminum thermal radiation shield is thermally anchored to the N_2 reservoir. The radiation shield surrounds the He reservoir and extends to the tail of the Dewar [see Fig. 4.4 (Top)]. The aluminum shielding is wrapped with several layers of aluminized Mylar foil. This reduces the radiation load from room temperature, therefore decreasing both the liquid He and N_2 consumption. This design results in He and N_2 consumption rates of 500 and 1100 standard cubic centimeters per minute (sccm), respectively. The consumption rates are monitored for diagnostic purposes during operation using a mass flow meter.

The RT sample and the vacuum space of the Dewar are separated by a 25 μm thick sapphire window. Several scanning SQUID microscope systems, mainly using high-*Tc* superconducting SQUID sensors, have successfully used this approach for the vacuum window [18,25-27]. Sapphire has a low electrical conductivity which is critical in order to avoid sources of Johnson noise close to the sensor. It also has a high elastic modulus, which minimizes the inward deflection of the sapphire due to the pressure difference. Furthermore, sapphire has the advantage of being optically transparent, which facilitates the centering and alignment procedure of the sensor with respect the window. A 1 mm thick sapphire backing window with an outer diameter of 25 mm and inner diameter of 1.5 mm supports the 25 μm thin window to minimize bowing. Following the calculations of Lee et al [25], we have estimated a window bowing on the order of 1 μm.

In order to maintain a good insulation vacuum for longer periods of time and to increase the pumping speeds for water and gases like O_2, N_2, and He, we have incorporated a container filled with activated charcoal, which acts as a cryopump. The container is thermally anchored to the He tank. Figure 4.4 (Bottom) shows its location on the He reservoir.

Our SQUID microscope system can be kept at cryogenic temperatures for periods of over one month without deterioration in performance. During this time range, we performed consecutive 23 hour high-resolution magnetic field scans of geological samples during a demagnetization experiment at a sensor-to-sample distance of 120 μm. The scans were interrupted only by the liquid N_2 and He transfers. Therefore, we confirmed the reliability of the instrument to operate under the identical conditions over long periods of time.

4.3.3. Cold finger design

SQUID microscopes generally have the position of the sensor or pickup coil fixed and it is necessary to adjust the Dewar tail to bring the window as close as possible to the cold sensor. In our experience, this procedure is cumbersome, because not only the distance has to be adjusted but also the tilt between the window and the sensor surface. To overcome part of the problem, we have incorporated a flexure bearing mechanism actuated by a lever arm to precisely and easily control the vertical position of the sensor into our system. A cross section of the Dewar tail with the lever mechanism is shown in Fig. 4.4 (Bottom). The cryogenic positioning system consists of three different main components. On the top of the Dewar a rotary vacuum feed-through is connected to a G-10 rod. The G-10 rod is attached to a lead screw and a slider which converts the screw rotational movement into a vertical displacement. The slider is connected to the lever arm via a Kevlar tread [see Fig. 4.4 (Middle)]. The lever arm pushes against a shaft that is mounted in the center of two flexure bearings, which are spaced 50 mm apart and anchored to an aluminum support structure. The cold finger is clamped to the shaft and extends it towards the vacuum window. The two flexure bearings in the support structure provide mechanical stability and ensure precise vertical displacement. We have measured a vertical displacement of about 40 μm per turn of the rotary vacuum feed-through. Using this mechanism, we can precisely control the vertical position of the SQUID sensor with respect to the sapphire window. We generally set the distance between the sensor and the sample by approaching the window until we notice a small increase in the He boil off rate as measured by a mass flow meter. We then confirm the position of the SQUID with respect to the sapphire window with an inverted optical microscope and adjust the tilt, if necessary, after the cool down procedure. Using

this approach, we found that the distance between the sensor and the sample can be reproducibly adjusted to 100 μm [22].

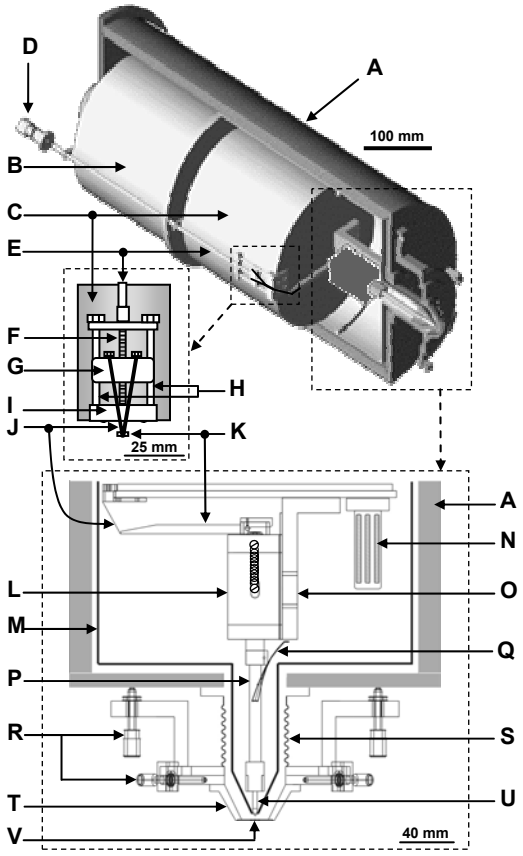

Figure 4.4: Detailed cross-sectional schematic of the SQUID microscope Dewar. (Top) Cryostat (A) G-10 fiberglass Dewar casing, (B) Liquid N2 reservoir, (C) Liquid He reservoir. (Middle) Positioning mechanism . (D) Rotary vacuum feed-through, (E) G-10 rod, (F) Lead screw, (G) Slider, (H) Slider posts, (I) Brass connection, (J) Kevlar tread, (K) Lever arm. (Bottom) SQUID Dewar tail. (L) Aluminum flexure bearing support structure, (M) Aluminum thermal radiation shield, (N) Cryopump, (O) Copper L-shaped bracket, (P) Copper cold finger, (Q) Flexible copper braids, (R) Micrometer positioning screws, (S) Brass bellows, (T) G-10 cone, (U) Sapphire rod, (V) 25 mm thick sapphire window.

The cold finger terminates in a collet which holds a sapphire rod. The collet is tightened using a G10-nut. A thin layer of Apiezon grease on the sapphire rod provides a good thermal contact to the copper cold finger. Additional thermal links to the solid copper L-shaped bracket

mounted on the He reservoir are provided by two flexible copper braids soldered into the center of the cold finger. Depending on the sensor configuration, the sapphire rod has a bobbin machined at the tip (for miniature pickup coils) or is conical shaped (for monolithic sensor chips).

The monolithic SQUID sensor chips are mounted on the tip of the conical shaped sapphire rod. Using a diamond impregnated wire saw, we first cut the edges of the 2.5 × 2.5 mm^2 chip to reduce its diameter to a few hundred microns. This method is very effective in reducing the size of the chip without damaging the gold contact pads that will be used to connect to the SQUID and the integrated feedback line. Then, we mount the SQUID chip on the tip of the sapphire rod using a low-temperature epoxy resin (Stycast). After mounting the chip, we grind and polish the edges of the chip to reduce its diameter and provide a smooth surface around the edge. We deposited 200 nm silver pads to extend the electrical connection around the edges toward the side of the chip. Four 25 μm gold wires are then attached to the silver pads on the sides of the SQUID chip using silver epoxy to connect the SQUID to a cold step-up transformer, the DC bias source and the feedback coil of the Flux-Locked Loop (FLL) electronics. Figure 4.5 shows a SEM image of a SQUID mounted on a sapphire rod.

4.3.4. System integration

Figure 4.6 shows a picture of the entire system. The SQUID microscope Dewar is supported by a wooden structure above the non-magnetic scanning stage. Two high-precision piezoelectric inchworm motors are used to perform the XY-raster scan [18]. The whole system is housed in a three layer, μ-metal shielded room (Vacuumschmelze, Hanau) to eliminate near zero and high frequency background noise. The monolithic DC-SQUID sensors are operated in FLL configuration with custom designed electronics [28], which use a flux modulation frequency of

100 KHz. For a high-sensitivity setup, we typically adjust the feedback resistor to provide a dynamic range of $\pm 10\,\phi_0$, where ϕ_0 is the flux quantum. The output voltage is digitized by a PCI-MIO card (National Instruments) with 16-bit resolution. The stage and acquisition parameters are controlled by software developed using LabVIEW (National Instruments).

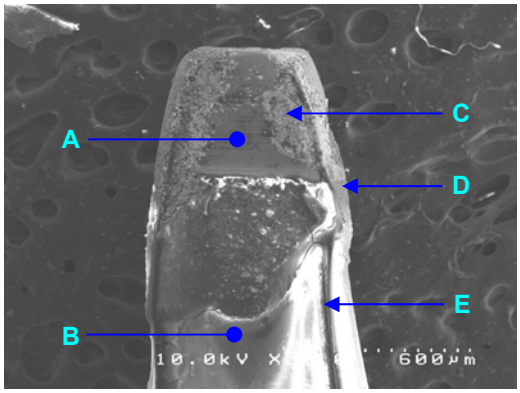

Figure 4.5: SEM image of a monolithic SQUID chip wired and mounted on the tip of a sapphire rod. (A) SQUID chip, (B) sapphire rod, (C) silver epoxy, (D) low-temperature epoxy resin (Stycast) and (E) gold wires connecting the SQUID to the electronics.

Figure 4.6: Photograph of the entire system including the non-magnetic scanning stage and SQUID Dewar wooden support structure. The SQUID microscope system is housed inside a 3 layer μ-metal magnetically shielded room.

4.4. Measurements and applications

In the following sections, we present applications in two areas where our SQUID microscope system leads to new information difficult to obtain with other techniques. As we outlined above, our system can be equipped with different SQUID sensors depending on the particular magnetic source configuration. We first describe applications using SQUID sensors to image magnetic field originating from magnetizations in geological samples, which do not require a compromise between spatial resolution and field sensitivity, provided we can get the sensor close to the sample. Therefore, a monolithic bare SQUID design is the best suited approach. In contrast, when imaging action or injury currents generated by living tissue, the current sources are weak and distributed, requiring sensors with higher sensitivities. In order to achieve these higher sensitivities, we must compromise spatial resolution. The multiloop SQUID sensor is ideal for this application.

4.4.1. Paleomagnetism

One of the major research areas that will benefit from the development of our SQUID microscopes is paleo- and geomagnetism. Kirschvink argued that the many paleomagnetic studies were limited by the sensitivity of current magnetometer systems in use [29]. He showed that magnetizations at the level of 10^{-14} to 10^{-15} Am^2 can be preserved in sedimentary rocks. Current commercially available magnetometers like the 2G Superconducting Rock Magnetometer have moment sensitivities around 10^{-12} Am^2. The sensitivity of our SQUID microscope system can also be expressed as moment sensitivity. For our bare SQUID design with an effective diameter of 80 μm, we calculated a magnetic moment sensitivity of 5.4×10^{-18} $Am^2/Hz^{1/2}$ for frequencies above 100 Hz at a sensor-to-sample spacing of 100 μm.

Superconducting Rock Magnetometers measure the average magnetization in a sensing volume of a 1 in round and 1 in high cylinder. In contrast, SQUID microscopy provides images of the magnetic field above the sample with sub-millimeter resolution. This is especially important for geological samples which are not homogeneously magnetized. We can now study the geomagnetic properties on a grain-by-grain basis in integral geological samples in massively parallel measurements. This results in information which is difficult or impossible to obtain using conventional superconducting rock magnetometers.

Using our first generation SQUID microscope with a 250 μm pickup coil, we imaged the magnetic field associated with the remanent magnetization of the Martian meteorite ALH84001. We performed a thermal demagnetization experiment to determine the maximum temperature the rock has been exposed to since ejected from Mars through a meteoroid impact [15,16]. Since then, we have improved the SQUID microscope, and incorporated our monolithic bare SQUID sensors, which drastically improved the field sensitivity and spatial resolution of the system. Figure 4.7 shows a direct comparison between images obtained with a 250 μm pickup coil and a bare SQUID washer design with an effective diameter of 120 μm. The images show magnetic field distributions resulting from the remanent magnetization of a 30 μm thin section of a basalt pillow from the Kilauea Volcano, Hawaii at a sample-to-sensor distance of 120 μm. In order to show the improvement in spatial resolution, we took a line scan along identical features at the same location in both magnetic images [see Fig. 4.7(d)]. The red line is from the scan measured with the 250 μm pickup coil and the blue line from the bare SQUID with an effective diameter of 120 μm. We can clearly identify smaller features on the order of the effective diameter of the monolithic SQUID sensor, which are averaged in images obtained with the 250 μm pickup coil.

The spatial averaging has both contributions from the larger diameter and the volume of the pickup coil.

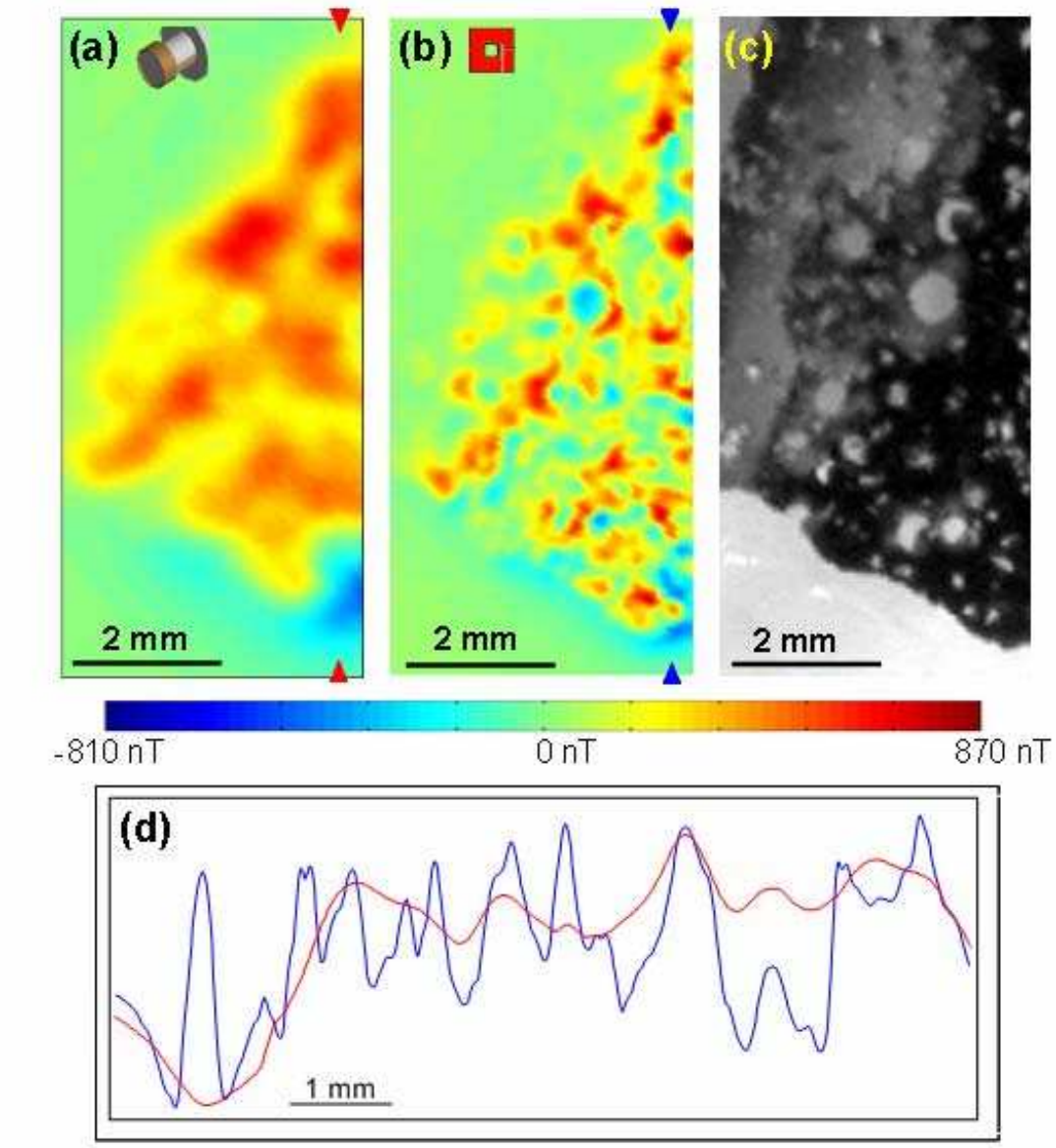

Figure 4.7: Comparative magnetic field maps of a 30 µm thin section of a basalt pillow recorded using (a) a hand wound 9 turns 250 µm diameter pick up coil inductively coupled to a commercial SQUID sensor, (b) bare SQUID design with an effective diameter of 120 µm. and (c) Optical picture of the imaged area. (d) Line scans through both magnetic field images at identical locations as indicated by arrows in (a) and (b). The red line corresponds to image (a) and the blue line to image (b).

Many paleomagnetic techniques require successive recordings of the magnetic field of the sample after demagnetization or remagnetization experiments. For these experiments it is essential to spatially correlate the magnetic field maps after each recording, which requires the sample to be registered with respect to the sensor height and the scanning directions. To address this issue, we developed a spring-loaded mechanism attached to the scanning stage, which allows us to scan a flat thin section in contact with the sapphire window. Figure 4.8 shows a schematic of the mechanism. A rectangular Plexiglas sample holder sits over a pair of rubber bands and fits tight inside a square opening. The mechanism is mounted on top of the pedestal of our scanning stage. In this way, we scan a flat sample in contact with the window and guarantee that the sample will be as close as possible to the sensor. This set up allows us to remove the sample, perform Alternating Field (AF) demagnetization or Isothermal Remanent Magnetization (IRM) steps on the sample and place it in the same location to correlate measurements and identify the underlying petrography.

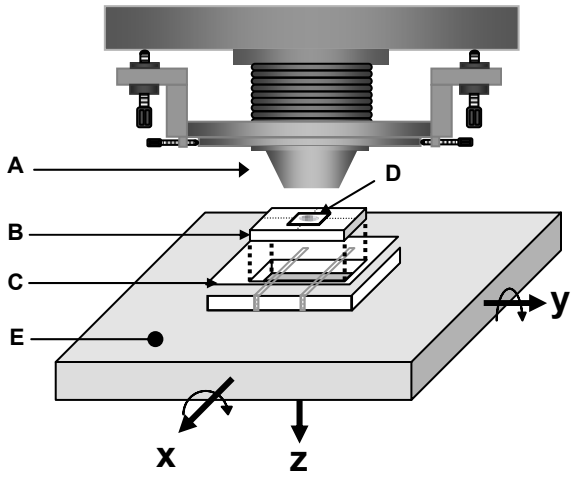

Figure 4.8: Schematic of spring-loaded mechanism mounted on the top of the scanning stage. (A) Tail of the SQUID microscope, (B) sample holder, (C) support frame (D) rubber bands, (E) geological thin section (sample),(F) Plexiglas pedestal attached to base of the scanning stage.

To test the precision of the spring loaded mechanism, we used a 1 μm precision dial indicator to measure the relative tilt between the surface of the window and a flat sample while scanning. Figure 4.9 shows this measurement. First, we measured the relative tilt between the scanning stage and the window, Fig. 4.9(a). The two steps in the scan are caused by the thickness of the thin sapphire window with a thin layer of epoxy. Then, we placed the dial indicator below the sample holder in order to measure the tilt of the holder while scanning against the window, Fig. 4.9(b). Comparing these two measurements, we estimated a relative tilt between the surface of the window and the sample holder of 0.097^{o} while performing a scan.

To register the magnetic field images and correlate them to petrography or a compositional analysis we have developed a spatial registration technique. Figure 4.10 shows an example of the method for a geological thin section. After the sample's magnetic distribution has been acquired, we remove the sample and place a wire in a cross-hair pattern in its place. We then apply an alternating current through the wire and measure its magnetic field pattern using a lock-in amplifier technique over the same area where the sample was located. From the wire magnetic mapping, we can localize the position of the wire by the zero-field crossing. Since both the sample and the wire scan were measured with respect to the same origin defined by the coordinate system of the scanning stage, we can now spatially superimpose these two images. We then take an optical image of the wire pattern and the sample for angular alignment. Using a scale bar we can then adjust the size of the optical image to the magnetic image which was taken using the reference coordinate system of the scanning stage. Using this technique we can overlap and correlate specific features in the magnetic images with the location in the optical image. This registration technique could also be used for a correlation to a compositional or crystallographic analysis.

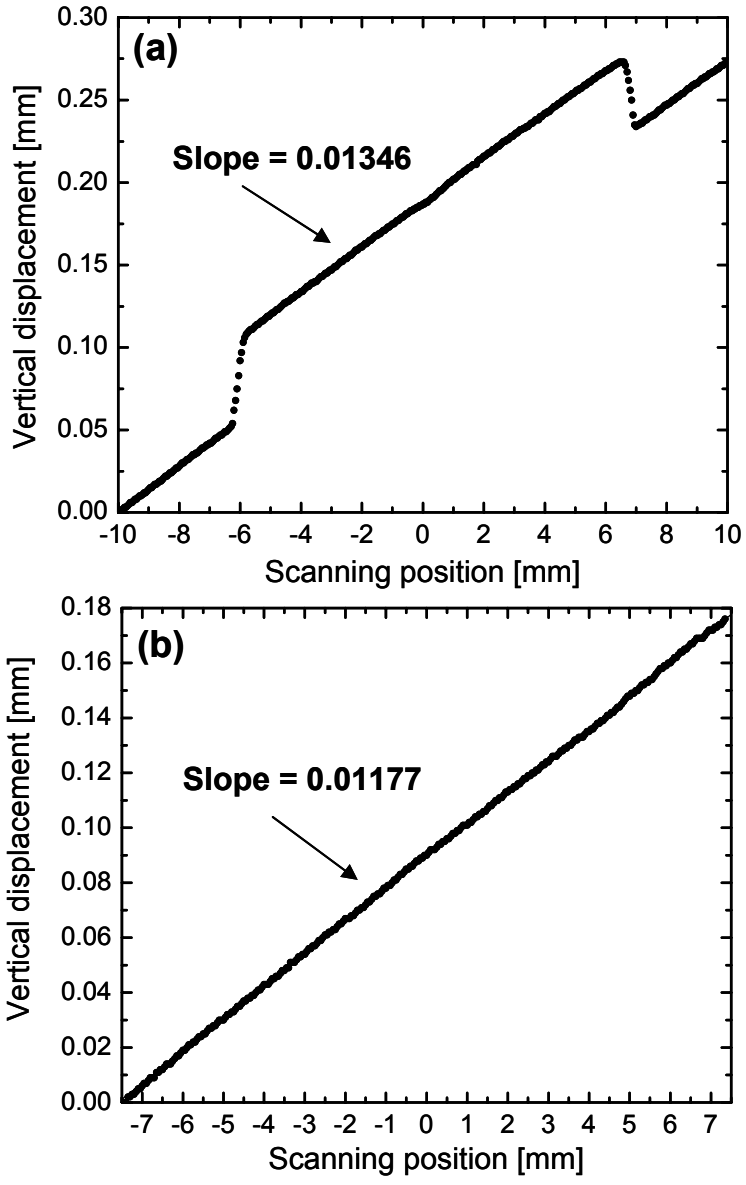

Figure 4.9: (a) Relative height between the scanning stage platform and the vacuum window of the SQUID microscope during a line scan. The steps in the curve result from the thickness of the 25 μm sapphire window and a thin layer of epoxy used to glue the sapphire window to the backing window. (b) Vertical displacement of the sample holder while pressed against the window by the spring loading mechanism during a line scan. From these measurements, we estimated a tilt of 0.097^{o} between the sample surface and the sapphire window.

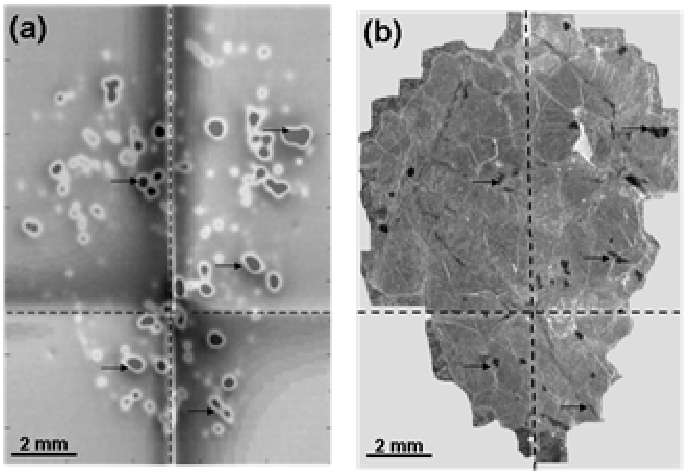

Figure 4.10: (a) Superposition of the magnetic field map from the sample and the magnetic field generated by wires across the sample used for registration purposes. (b) Optical picture of the sample. The dashed line shows the position of the wire. This registration technique allows us to correlate magnetic features with features in the optical image (arrows).

Our sample-to-sensor spacing of around 100 μm limits both our spatial resolution to 100 μm and our moment sensitivity to 10^{-18} Am^2 /$Hz^{1/2}$ in the white noise region for frequencies above 1 Hz. We are currently working to reduce both the sample-to-sensor spacing and the sensor size. We expect to improve our spatial resolution by at least a factor of two and consequently, our moment sensitivity by a factor of eight.

A great variety of rock- and paleomagnetic experiments can now be done on individual grains in standard petrographic thin sections and the measured magnetic field can be matched to the composition and to the petrography of the sample. The incorporation of monolithic bare SQUID sensors into our scanning SQUID microscope allows measurements currently not possible with existing commercially available instrumentation.

4.4.2. Biomagnetism

SQUID magnetometer systems have been widely used to study a great variety of bioelectric and biomagnetic phenomena [12]. Multichannel SQUID systems with pickup coil

diameters of 10 to 30 mm with a similar sample-to-sensor spacing are generally used in human studies. These systems do not provide the spatial resolution necessary to study the generation of the magnetic activity or injury currents at tissue and cellular scales. In excitable tissue extracellular potentials, transmembrane potentials, or action currents are interrelated. To make model predictions, one should at least measure more than one of these quantities, especially in tissues with different anisotropies in the intra- and extracellular space. The extracellular potentials are typically recorded using microneedle arrays. However, the insertion of microneedles influences the measurement results [30] and is impractical to achieve sub-millimeter spatial resolutions. Our approach is to record the transmembrane potential optically and the action currents using SQUID microscopy, which allows us to obtain more detailed information on the generation of the magnetocardiogram (MCG). High-resolution biomagnetic imaging provides insights that will improve existing mathematical models of biological tissue.

By using a 6-spoke 500 μm diameter multiloop SQUID, we recorded magnetocardiograms (MCGs) on the surface of a perfused isolated rabbit heart. Figure 4.11 shows a photograph of a perfused isolated rabbit heart in a tissue bath under the tail of the Dewar. A bath temperature of 38° C is maintained by a second perfusion system and a heat exchanger. The heart was stimulated at a frequency of 3.33 Hz using a single coaxial electrode placed on the posterior left ventricular (LV) wall. The amplitude of the stimulation pulse was 2 mA, which is just above the threshold for diastolic stimulation. The anterior depolarization wave fronts generated by the stimulation pulse were imaged using a membrane bound fluorescent dye and a high-speed CCD camera [31]. After recording the transmembrane potential optically, the isolated rabbit heart was positioned under the tail of the SQUID microscope and lightly pressed against the sapphire window to minimize the sample-to-sensor spacing. One-second long time

traces of the magnetic field generated by the excitation were recorded at 144 locations on a 12 mm × 12 mm grid with a step size of 1 mm. The data acquisition was triggered on the stimulation pulse, allowing for synchronization of the magnetic field traces to produce a time series of two-dimensional field maps.

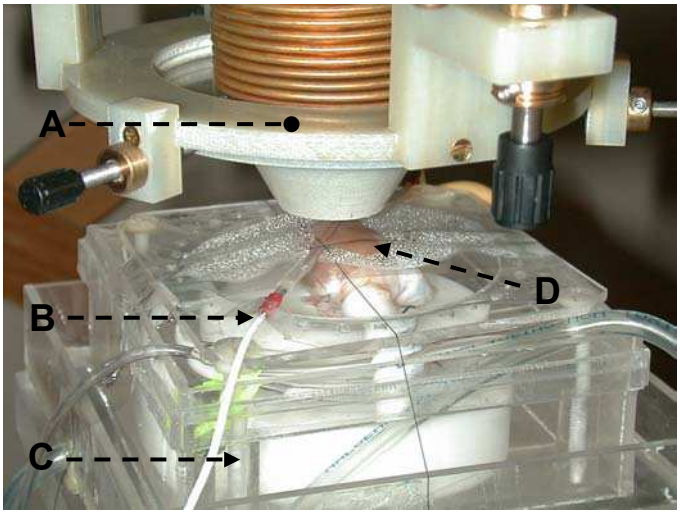

Figure 4.11: Photograph of the experimental setup to record the magnetocardiogram on the surface of an isolated rabbit heart. (A) Tail of the SQUID microscope, (B) isolated rabbit heart, (C) tissue bath and (D) registration wires.

Figure 4.12 (a) depicts the areas for the optical (blue) and the magnetic (red) recordings in relation to the anatomical features of the isolated heart. Time traces of the transmembrane potential and the magnetic field at the marked location are shown in Figure 4.12 (b). An optical image of the propagating depolarization wave front 53 ms after stimulation can be seen in Figure 4.12 (c). The optical data are offset by the resting potential and normalized by the maximum amplitude of the transmembrane potential. The wave fronts can be identified as the boarder between depolarized ($V/V_{max} \sim 1$) and resting tissue ($V/V_{max} \sim 0$). As shown in the image, two wave fronts originating from the posterior point stimulus are about to collide. A magnetic field

map of an area on the left ventricle, as marked by the white square in Figure 4.12 (c), is shown in Figure 4.12 (d).

In a previous study, we used a line stimulus in close proximity to the imaging area to generate a plane wave. We found that a reversal of magnetic field polarity is associated with the depolarization wave front [7]. The data presented here show that the wave front geometry can not be accurately predicted by a contour line between areas of opposite field polarity. This suggests that action currents flow over larger distances and therefore, the wave fronts influence each other over larger distances than suggested by the depolarization contours of the transmembrane potential maps.

It is clear from our observations that the intra- and interstitial potentials, and therefore, the currents are not scaled versions of the local transmembrane potential. The currents are determined by the transmembrane potential throughout the tissue and a local description in terms of a generator model is not applicable [32,33]. A detailed analysis of the data, a reduction in dimensionality to reduce the influence of fiber orientation, and well-defined wave front geometries are required to make more precise model predictions.

The improvement in field sensitivity achieved by using monolithic multiloop SQUID sensors allows us to study in more detail the relationship between extracellular potentials, transmembrane potentials and action currents, especially in thin layers of connective cardiac or brain tissue. We hope to achieve a higher sensitivity by optimizing the process parameters to lower the critical currents of the Josephson Junction of our multiloop SQUID sensors. For an optimized 1 mm multiloop SQUID sensor, we expect to achieve field sensitivities on the order of 20 $fT/Hz^{1/2}$.

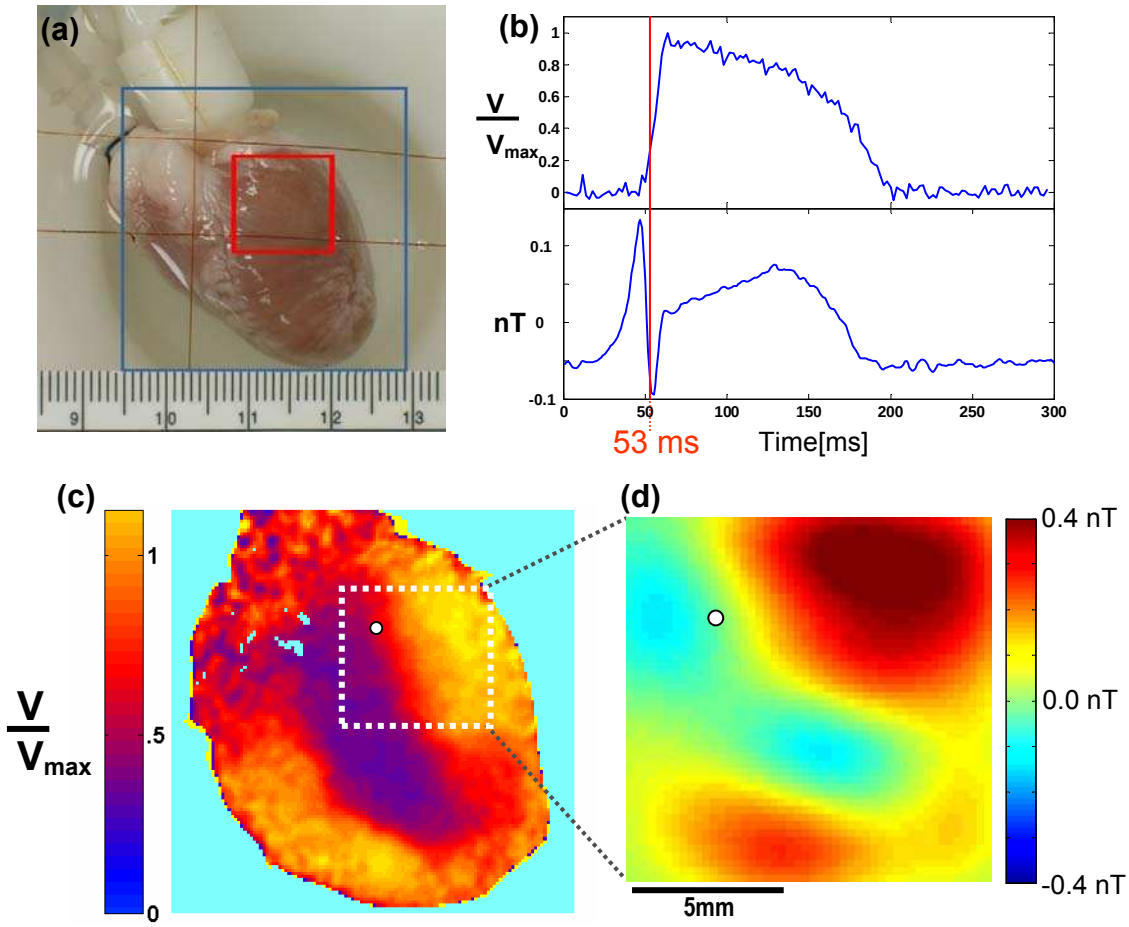

Figure 4.12: (a) Optical image of a Langendorff perfused rabbit heart indicating the imaging areas used to record transmembrane potentials (blue square) and magnetic fields (red square) associated with action currents. (b) Time trace of the transmembrane potential and the magnetic field recorded from the same location on the surface of the heart. (c) Image of the transmembrane potential distribution 53ms after stimulation. The two wave front from opposite sides are about to collide. (d) Magnetic field image composed of time traces 53 ms after the stimulus from the area indicated by a white dashed square in (c).

4.5. Acknowledgments

The authors would like to thank Ben Weiss, Joseph Kirschvink, and John Wikswo for fruitful discussion. This work was supported in part by NIH Grants (1-R43-RR16157-01 and 2-R01-HL58241-06), NSF – Earth Science (EAR-0004101) and DARPA (DSR # 16966).

4.6. References

[1] J. R. Kirtley, "SQUID microscopy for fundamental studies," *Physica C-Superconductivity and Its Applications*, vol. 368, no. 1-4, pp. 55-65, 2002.

[2] J. R. Kirtley and J. P. Wikswo, Jr., "Scanning SQUID microscopy," *Annual Reviews of Material Science*, vol. 29, pp. 117-148, 1999.

[3] J. P. Wikswo, Jr., "High-resolution magnetic imaging: Cellular action currents and other applications," in *SQUID Sensors: Fundamentals, Fabrication and Applications*. H. Weinstock, Ed. The Netherlands: Kluwer Academic Publishers, 1996, pp. 307-360.

[4] I. M. Thomas, S. M. Freake, S. J. Swithenby, and J. P. Wikswo, "A Distributed Quasi-Static Ionic Current Source in the 3-4 Day-Old Chicken-Embryo," *Physics in Medicine and Biology*, vol. 38, no. 9, pp. 1311-1328, 1993.

[5] Y. R. Chemla, H. L. Grossman, T. S. Lee, J. Clarke, M. Adamkiewicz, and B. B. Buchanan, "A New Investigation of Bacterial Motion: Superconducting Quantum Interference Device Microscopy of Magnetotactic Bacteria," *Biophys. J.*, vol. 76, pp. 3323-3330, 1999.

[6] F. Baudenbacher, N. T. Peters, P. Baudenbacher, and J. P. Wikswo, "High resolution imaging of biomagnetic fields generated by action currents in cardiac tissue using a LTS-SQUID microscope," *Physica C: Super.*, vol. 368, no. 1-4, pp. 24-31, Mar.2002.

[7] Holzer J.R., Fong L.E., Sidorov V.Y., Wikswo J.P., and Baudenbacher F., "Magnetic and fluorescent imaging of plane waves in cardiac tissue reveals currents parallel to the wave front," *Accepted to Biophysical Journal*, 2004.

[8] Baudenbacher F., Fong L.E., Thiel G., Wacke M., Jazbinsek V., Holzer J.R., Stampfl A., and Trontelj Z., "Intracellular Axial Current in Chara corallina Reflects the Altered Kinetics of Ions in Cytoplasm under the Influence of Light," *Biophys. J.*, 2004.

[9] S. Chatraphorn, E. F. Fleet, F. C. Wellstood, L. A. Knauss, and T. M. Eiles, "Scanning SQUID microscopy of integrated circuits," *Appl. Phys. Lett.*, vol. 76, no. 16, pp. 2304-2306, 2000.

[10] E. F. Fleet, S. Chatraphorn, F. C. Wellstood, and L. A. Knauss, "HTS scanning SQUID microscopy of active circuits," *IEEE Trans. Appl. Supercond.*, vol. 9, no. 2, pp. 4103-4106, 1999.

[11] H. Weinstock, "A Review of Squid Magnetometry Applied to Nondestructive Evaluation," *IEEE Trans. Mag.*, vol. 27, no. 2, pp. 3231-3236, 1991.

[12] J. P. Wikswo, Jr., "Applications of SQUID magnetometers to biomagnetism and nondestructive evaluation," in *Applications of Superconductivity*. H. Weinstock, Ed. Netherlands: Kluwer Academic Publishers, 2000, pp. 139-228.

[13] U. Klein, M. E. Walker, C. Carr, D. M. McKirdy, C. M. Pegrum, G. B. Donaldson, A. Cochran, and H. Nakane, "Integrated low-temperature superconductor SQUID gradiometers for nondestructive evaluation," *IEEE Trans. Appl. Supercond.*, vol. 7, no. 2, pp. 3037-3039, 1997.

[14] A. Abedi, J. J. Fellenstein, A. J. Lucas, and J. P. Wikswo, "A superconducting quantum interference device magnetometer system for quantitative analysis and imaging of hidden corrosion activity in aircraft aluminum structures," *Rev. Sci. Instrum.*, vol. 70, no. 12, pp. 4640-4651, 1999.

[15] B. P. Weiss, H. Vali, F. J. Baudenbacher, J. L. Kirschvink, S. T. Stewart, and D. L. Shuster, "Records of an ancient Martian magnetic field in ALH84001," *Earth and Planetary Science Letters*, vol. 201, no. 3-4, pp. 449-463, 2002.

[16] B. P. Weiss, J. L. Kirschvink, F. J. Baudenbacher, H. Vali, N. T. Peters, F. A. Macdonald, and J. P. Wikswo, "A low temperature transfer of ALH84001 from Mars to Earth," *Science*, vol. 290, no. 5492, pp. 791-795, 2000.

[17] B. J. Roth, N. G. Sepulveda, and J. P. Wikswo, Jr., "Using a Magnetometer to Image a Two-dimensional Current Distribution," *J. Appl. Phys.*, vol. 65, no. 1, pp. 361-372, 1989.

[18] F. Baudenbacher, N. T. Peters, and J. P. Wikswo, Jr., "High Resolution Low-Temperature Superconductivity Superconducting Quantum Interference Device Microscope for Imaging Magnetic Fields of Samples at Room Temperatures," *Rev. Sci. Instrum.*, vol. 73, no. 3, pp. 1247-1254, 2002.

[19] B. P. Weiss, F. J. Baudenbacher, J. P. Wikswo, and Kirschvink J.L., "Magnetic Microscopy Promises a Leap in Sensitivity and Resolution," *Eos Trans. AGU*, vol. 82, pp. 513-518, 2001.

[20] C. D. Tesche and J. Clarke, "Dc Squid - Noise and Optimization," *J. Low Temp. Phys.*, vol. 29, no. 3-4, pp. 301-331, 1977.

[21] J. M. Jaycox and M. B. Ketchen, "Planar Coupling Scheme for Ultra Low-Noise Dc Squids," *IEEE Trans. Mag.*, vol. 17, no. 1, pp. 400-403, 1981.

[22] F. Baudenbacher, L. E. Fong, J. R. Holzer, and M. Radparvar, "Monolithic low-transition-temperature superconducting magnetometers for high resolution imaging magnetic fields of room temperature samples," *Appl. Phys. Lett.*, vol. 82, no. 20, pp. 3487-3489, 2003.

[23] J. E. Zimmerman, "Sensitivity Enhancement Of Superconducting Quantum Interference Devices Through Use Of Fractional-Turn Loops," *J. Appl. Phys.*, vol. 42, no. 11, pp. 4483-4487, 1971.

[24] L. E. Fong, J. R. Holzer, K. McBride, E. A. Lima, F. Baudenbacher, and M. Radparvar, "High-resolution imaging of cardiac biomagnetic fields using a low-transition-

temperature superconducting quantum interference device microscope," *Appl. Phys. Lett.*, vol. 84, no. 16, pp. 3190-3192, 2004.

[25] T. S. Lee, E. Dantsker, and J. Clarke, "High-transition temperature superconducting quantum interference device microscope," *Rev. Sci. Instrum.*, vol. 67, no. 12, pp. 4208-4215, 1996.

[26] F. Gruhl, M. Muck, M. von Kreutzbruck, and J. Dechert, "A scanning superconducting quantum interference device microscope with high spatial resolution for room temperature samples," *Rev. Sci. Instrum.*, vol. 72, no. 4, pp. 2090-2096, 2001.

[27] Black R.C., "Magnetic Microscopy using a Superconducting Quantum Interference Device." PhD University of Maryland, 1995.

[28] J. Clarke, W. M. Goubau, and M. B. Ketchen, "Tunnel Junction Dc Squid - Fabrication, Operation, and Performance," *J. Low Temp. Phys.*, vol. 25, no. 1-2, pp. 99-144, 1976.

[29] Kirschvink J.L., "How sensitivite should a rock magnetometer be for use in paleomagnetism?," in *SQUID Applications to Geophysics*. H. Weinstock and Overton W.C., Eds. 1981, pp. 111-114.

[30] D. M. Langrill and B. J. Roth, "The effect of plunge electrodes during electrical stimulation of cardiac tissue," *IEEE Trans. Biomed. Eng.*, vol. 48, no. 10, pp. 1207-1211, 2001.

[31] S.-F. Lin, R. A. Abbas, and J. P. Wikswo, Jr., "High-resolution High-speed Synchronous Epifluorescence Imaging of Cardiac Activation," *Rev. Sci. Instrum.*, vol. 68, no. 1, pp. 213-217, 1997.

[32] R. Plonsey and R. C. Barr, "Current Flow Patterns in Two-dimensional Anisotropic Bisyncytia with Normal and Extreme Conductivities," *Biophys. J.*, vol. 45, pp. 557-571, 1984.

[33] R. Plonsey and Y. Rudy, "Electrocardiogram Sources in a 2-dimensional Anisotropic Activation Model," *Medical & Biological Engineering & Computing*, vol. 18, pp. 87-94, 1980.

CHAPTER V

MONOLITHIC LOW-TRANSITION-TEMPERATURE SQUID MAGNETOMETERS FOR HIGH RESOLUTION IMAGING MAGNETIC FIELDS OF ROOM TEMPERATURE SAMPLES

Franz Baudenbacher[1], Luis E. Fong[1], Jenny R. Holzer[1], Masoud Radparvar[2]

[1]Department of Physics and Astronomy
Vanderbilt University, Nashville, TN, 37235

[2]Hypres Inc., Elmsford, NY, 10523

Adapted from:
F. Baudenbacher. L.E. Fong, J.R., Holzer, M. Radparvar, *Applied Physics Letters*
Vol. 82, No. 20, pp. 3487- 3489, May 2003.

5.1. Abstract

We have developed a monolithic Low-Temperature Superconducting Quantum Interference Device (SQUID) magnetometer and incorporated the device in a scanning microscope for imaging magnetic fields of room temperature samples. The instrument has a ~100 μm spatial resolution and a 1.4 pT/Hz$^{1/2}$ field sensitivity above a few Hertz. We discuss design constraints on and potential applications of the SQUID microscope.

5.2. Introduction

Scanning superconducting quantum interference device (SQUID) microscopy is a powerful technique for imaging magnetic field distributions. SQUID magnetometers have unsurpassed energy sensitivity but are subject to trade offs between field sensitivity and spatial resolution. The spatial resolution is optimal when the spacing between the cryogenic sensor and the sample is comparable to the sensor diameter [1]. SQUID microscopes using high-temperature superconductivity (HTS) have achieved 15–50 μm separations and 50 μm spatial resolution [2,3]. HTS SQUIDs have intrinsic white noise levels that are 4–5 times higher than that of low-temperature superconductivity (LTS) SQUIDs and suffer from excess 1/*f* noise at low frequencies associated with flux motion in the bulk superconductor or critical current fluctuations [4] in the Josephson junctions (JJ). Hence, HTS SQUIDs have not yet provided the combined low frequency and high spatial resolution required for magnetic imaging of bioelectric currents in living tissue or weak remnant magnetization in geological samples [5]. In contrast, magnetic imaging techniques using scanning electron microscopy with polarization analysis would provide a resolution on the order of 10 nm; however, the technique is highly surface

sensitive and requires the sample to be placed in vacuum, which is incompatible with biological samples [6,7].

Here we describe a SQUID microscope using thin-film niobium LTS SQUID sensors providing spatial resolution comparable to HTS SQUID instruments but increased sensitivity. Furthermore, our LTS SQUID technology allows the fabrication of apodized sensor coils [8], miniature susceptometers [9], multiloop miniature SQUIDs [10], or other multilayer circuits, which will add sensitivity and functionality to SQUID microscopy of room temperature (RT) samples.

5.3. Methods

Our LTS SQUID microscope is based on our previous cryogenic design [11], with the hand-wound superconducting niobium wire pickup coil and in-vacuum commercial SQUID replaced by a monolithic SQUID sensor chip [Fig. 5.1(a)]. The SQUID chip is mounted on the conical tip of a sapphire rod, and is contacted using thin silver films that extend the contact pads around the edges onto the sapphire rod. The sapphire is thermally anchored to the He reservoir with a copper cold finger on a flexure bearing assembly. This allows the tip of the sapphire to be placed within a few tens of microns of a 25 μm thick sapphire window separating the RT sample from the cryostat vacuum space. Dewar-tail details are shown in Fig. 5.1(b). The sapphire rod is surrounded by a nitrogen-cooled fiber-glass cone wrapped with aluminized mylar to intercept RT radiation. Liquid helium is consumed at 1.4 l/day. The sample is scanned in close proximity to the window by a precision piezoelectric nonmagnetic scanning stage. The microscope is housed in a three layer, μ-metal magnetically shielded room to reduce magnetic interference.

To obtain a high spatial resolution, our dc-SQUID sensor directly detects the sample's magnetic field. Figure 5.1(c) shows the layout and the integrated feedback line. The resistively shunted JJs were fabricated using a Nb/Al trilayer process with Mo thin film shunt resistors. Our photolithographic process imposes a minimum JJ diameter on 3.5 μm, which results in a self-capacitance, C of 0.4 pF/JJ, and a critical current $I_C \sim 25$ μA at a process-specific critical current density of ~ 100 A/cm^2.

The optimum sensitivity for a dc SQUID operated at 4.2 K requires that the JJ parameters and the SQUID inductance, L are chosen to satisfy the two constraints, $\beta c = 2\pi I_C R^2 C/\Phi_o \leq 0.7$ and $\beta_L = 2LI_C/\Phi_o \approx 1$, where $\Phi_o \sim 2 \times 10^{-15}$ Wb is the flux quantum, I_C is the JJ critical current, and R is the shunt resistance. The first constraint eliminates hysteresis and ensures a single-valued average voltage across the SQUID for a given external field. The second parameter, β_L, is a measure of the modulation depth of the critical current, $\Delta I_m = 2I_C / (1+\beta_L)$, as a function of applied flux. For $\beta_L > 1$, the current modulation depth becomes smaller, while for $\beta_L < 1$ the modulation depth approaches the limit $\Delta I_m = 2I_C$. The equivalent flux noise has a power spectral density:

$$S_\Phi(f) = \frac{S_V(f)}{\left(\frac{\partial V}{\partial \Phi}\right)^2} \tag{5.1}$$

which for an optimized SQUID with $\beta_L = 1$ and $\beta_C < 0.7$ is frequency independent down to low frequencies and given by[12]:

$$S_\Phi(f) = \frac{16 k_B T L^2}{R} = 16 k_B T L \sqrt{\frac{\pi LC}{\beta_C}} \tag{5.2}$$

In this case, the voltage-to-flux transfer function is $\partial V/\partial\Phi \approx R/L$. Here f denotes the frequency, $S_V(f)$ is the voltage noise, k_B is the Boltzman constant, and T is the temperature. The optimization for a bare SQUID is straightforward and requires reducing T, L, and C. Since the junction size determines C and I_C, R needs to be adjusted to keep $\beta_C < 0.7$ for a given L. Our SQUID design [Fig. 5.1(c)] decreases to $L = 1.25\mu_o d$ and becomes independent of line width of the washer, w if $w \geq d$, where μ_o is the permeability of free space and d is the hole diameter [13].

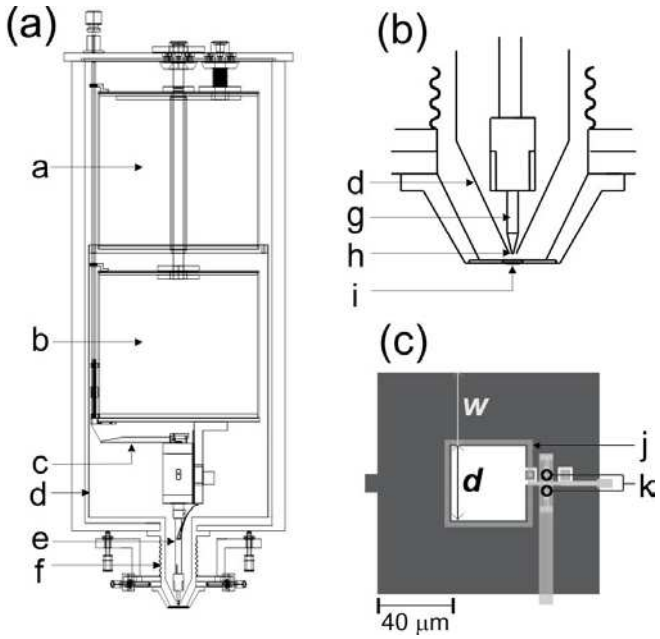

Figure 5.1: Schematic diagram of our SQUID microscope dewar: (a) [liquid N_2 (a) and He (b) vessels, lever mechanism (c), N_2-cooled radiation shield (d), Cu cold finger (e) and bellows mechanism (f)]; (b) close-up of the dewar tail [N_2-cooled radiation shield (d), sapphire finger (g), SQUID magnetometer (h), sapphire window (i)], and (c) layout of our single-chip LTS SQUID magnetometer [feedback and modulation coil (j), Josephson Junctions (k)].

5.4. Results

We fabricated and characterized three different square washer SQUIDs with d of 40, 60, and 80 μm to achieve an optimal compromise between spatial resolution and magnetic field

sensitivity. The effective area A_{eff} was measured in a uniform field and agrees with the geometrical area $A_{\mathrm{geo}} = (d + w)^2$. The voltage noise was recorded in a flux-locked loop. Figure 5.2 shows the field noise for a SQUID sensor with a 80 μm hole diameter, which is white up to the roll-off frequency of the electronics for all designs and increases only slightly at low frequencies. Table I lists the characteristics of the different SQUIDs. For the measured value of $\partial V/\partial \Phi$, the noise level of the 40 μm design agrees reasonably well with the theory. For the larger diameters, the noise increases and deviates significantly since $\beta_L > 1$. The increased flux noise is compensated by the increased effective area, leading to an almost constant field sensitivity of $\sim$ 1.5 pT/Hz$^{1/2}$ for all our designs. Given our junction size and critical current, the optimum design has $d = 40$ μm and $w = 40$ μm. Reduction of the junction size and I_C will lead to a further improvement of the SQUID performance.

Operation of the SQUID chips close to the room temperature window neither reduced the I_C nor increased the noise, demonstrating that the sensor temperature is close to 4.2 K. We verified the sample-to-sensor spacing of 100 ± 5 μm by scanning a current-carrying wire and fitting the data by numerically integrating over the geometrical area with the height as parameter [Fig. 5.3].

As a demonstration of this technique, Fig. 5.4 shows SQUID microscope measurements of the remnant magnetization of a 50 μm geological thin section taken from the Alan Hills Martian meteorite ALH84001. The image was acquired with a scan rate of ten points per second and a step size of 10 μm. From the line scan we can identify features that are comparable to the sensor size, as expected from our close sample-to-coil spacing. Registration of the magnetization images allows us to correlate the magnetization of particular grains with the petrography [14], a methodology applicable to numerous problems in material science and paleomagnetism.

Table 5.1: Parameters for representative bare SQUID magnetometers [Fig. 1 (c)]. (a) A_{eff} is the effective sensing area, $A_{\text{geo}} = (d + w)^2$ is the geometrical area, L the SQUID inductance, I_C the critical current, R the resistance of the shunt, ΔV peak-to-peak modulation depth, $\beta_L = 2LI_C/\Phi_o$. (b) $S_\Phi^{1/2}(f)_{\text{theo}}$ is the theoretical value according to Eq.(2) $S_\Phi(f)^{1/2}$ and $S_B(f)^{1/2}$ are the magnetic flux and field noise per unit bandwidth at the specified frequency.

(a)

d	A_{eff}	A_{geo}	L	I_C	R	ΔV	β_L
[μm]	[mm^2]	[mm^2]	[pH]	[μA]	[Ω]	[μV]	
40	$7.40*10^{-3}$	$6.40*10^{-3}$	58.1	21.81	2.6	16	1.22
60	$1.50*10^{-2}$	$1.44*10^{-2}$	87.2	25.94	2.6	14	2.19
80	$2.60*10^{-2}$	$2.56*10^{-2}$	116.3	23.73	2.4	11	2.67

(b)

d	$S_\Phi^{1/2}{}_{theo}$	$S_\Phi^{1/2}$(1KHz)	$S_B^{1/2}$(1Hz)	$S_B^{1/2}$(1KHz)
[μm]	[$\mu\phi_o$/Hz$^{1/2}$]	[$\mu\phi_o$/Hz$^{1/2}$]	[pT/Hz$^{1/2}$]	[pT/Hz$^{1/2}$]
40	1.53	5	3.5	1.4
60	1.75	12.1	3.0	1.6
80	2.14	17.1	2.4	1.4

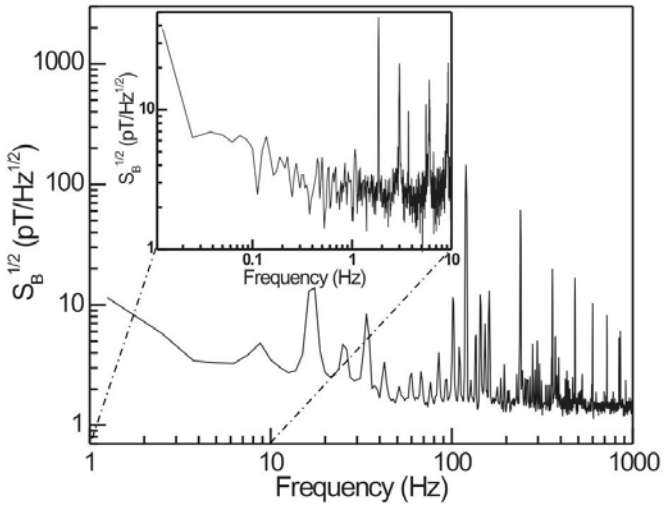

Figure 5.2: rms field noise of a monolithic LTS-SQUID magnetometer chips.

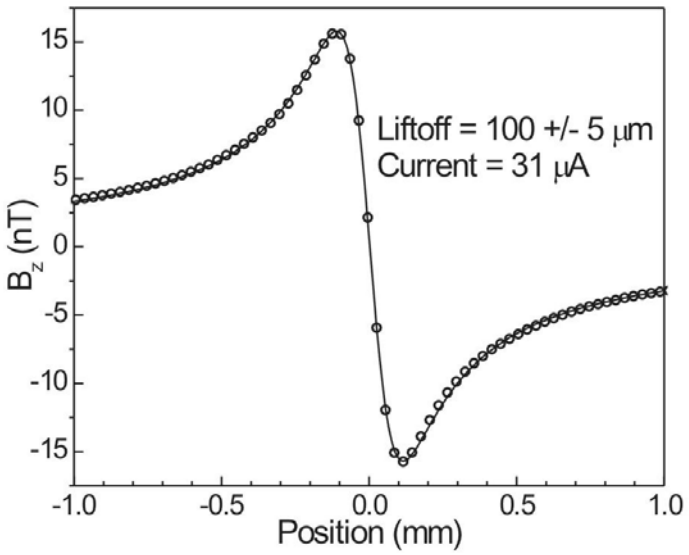

Figure 5.3: Sensor-to-sample distance assessment through measuring and, subsequently fitting the magnetic field of a thin film wire.

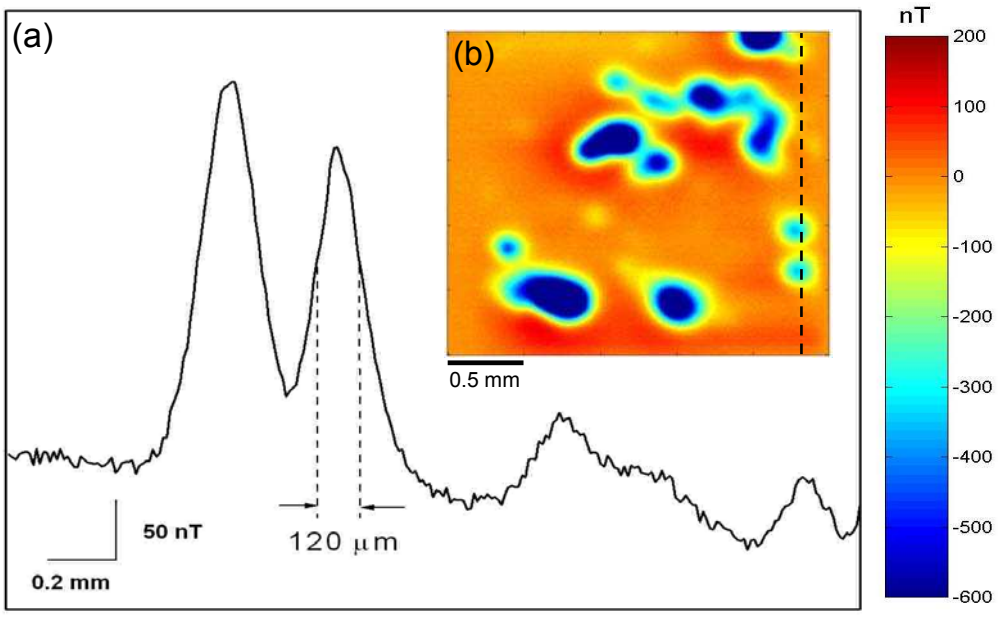

Figure 5.4: Magnetic image of a homogeneously-magnetized, 50 μm-thick geological thin section taken from the Martian meteorite ALH84001, and a line scan through the image showing a feature size of 120 μm.

5.5. Conclusion

In conclusion, we have developed a LTS SQUID microscope using Nb thin-film monolithic SQUID sensors to image the magnetic fields of RT samples with a field sensitivity of 1.4 pT/Hz$^{1/2}$ and a spatial resolution of ~ 80 μm. The sensitivity exceeds the values reported by Lee *et al.* [3] of 20 pT/Hz$^{1/2}$ for a HTS SQUID microscope with a comparable 30 μm hole and w = 10 μm. Reduction of the capacitance and our JJ I_C will further improve our sensitivity. We anticipate applications of our LTS SQUID microscope in areas such as biomagnetism and geomagnetism, where high sensitivities are required, especially at low frequencies.

5.6. Acknowledgments

The authors thank Ben Weiss, Joseph Kirschvink, and especially John Wikswo for fruitful discussions. The work was partly supported by NIH (1-R43-RR16157-01) and NSF-Earth Science (EAR-0004101).

5.7. References

[1] B. J. Roth, N. G. Sepulveda, and J. P. Wikswo, Jr., "Using a Magnetometer to Image a Two-dimensional Current Distribution," *J. Appl. Phys.*, vol. 65, no. 1, pp. 361-372, 1989.

[2] R. C. Black, A. Mathai, F. C. Wellstood, E. Dantsker, A. H. Miklich, D. T. Nemeth, J. J. Kingston, and J. Clarke, "Magnetic Microscopy Using A Liquid-Nitrogen Cooled Yba2Cu3O7 Superconducting Quantum Interference Device," *Appl. Phys. Lett.*, vol. 62, no. 17, pp. 2128-2130, 1993.

[3] T. S. Lee, Y. R. Chemla, E. Dantsker, and J. Clarke, "High-T-c SQUID microscope for room temperature samples," *IEEE Trans. Appl. Supercond.*, vol. 7, no. 2, pp. 3147-3150, 1997.

[4] E. Dantsker, S. Tanaka, P. A. Nilsson, R. Kleiner, and J. Clarke, "Low excess flux noise in YBa2Cu3O7-x dc SQUIDs cooled in static magnetic fields," *IEEE Trans. Appl. Supercond.*, vol. 7, no. 2, pp. 2772-2775, 1997.

[5] B. P. Weiss, F. J. Baudenbacher, J. P. Wikswo, and Kirschvink J.L., "Magnetic Microscopy Promises a Leap in Sensitivity and Resolution," *Eos Trans. AGU*, vol. 82, pp. 513-518, 2001.

[6] E. D. Dahlberg and R. Proksch, "Magnetic microscopies: the new additions," *Journal of Magnetism and Magnetic Materials*, vol. 200, no. 1-3, pp. 720-728, 1999.

[7] H. P. Oepen, G. Steierl, and J. Kirschner, "Scanning electron microscope with polarization analysis: Micromagnetic structures in ultrathin films," *Journal of Vacuum Science & Technology B*, vol. 20, no. 6, pp. 2535-2538, 2002.

[8] B. J. Roth and J. P. Wikswo, "Apodized Pickup Coils for Improved Spatial-Resolution of Squid Magnetometers," *Rev. Sci. Instrum.*, vol. 61, no. 9, pp. 2439-2448, 1990.

[9] M. B. Ketchen, T. Kopley, and H. Ling, "Miniature Squid Susceptometer," *Appl. Phys. Lett.*, vol. 44, no. 10, pp. 1008-1010, 1984.

[10] D. Drung, H. Matz, and H. Koch, "A 5-Mhz Bandwidth Squid Magnetometer with Additional Positive Feedback," *Rev. Sci. Instrum.*, vol. 66, no. 4, pp. 3008-3015, 1995.

[11] F. Baudenbacher, N. T. Peters, P. Baudenbacher, and J. P. Wikswo, "High resolution imaging of biomagnetic fields generated by action currents in cardiac tissue using a LTS-SQUID microscope," *Physica C: Super.*, vol. 368, no. 1-4, pp. 24-31, Mar.2002.

[12] C. D. Tesche and J. Clarke, "Dc Squid - Noise and Optimization," *J. Low Temp. Phys.*, vol. 29, no. 3-4, pp. 301-331, 1977.

[13] J. M. Jaycox and M. B. Ketchen, "Planar Coupling Scheme for Ultra Low-Noise Dc Squids," *IEEE Trans. Mag.*, vol. 17, no. 1, pp. 400-403, 1981.

[14] B. P. Weiss, H. Vali, F. J. Baudenbacher, J. L. Kirschvink, S. T. Stewart, and D. L. Shuster, "Records of an ancient Martian magnetic field in ALH84001," *Earth and Planetary Science Letters*, vol. 201, no. 3-4, pp. 449-463, 2002.

CHAPTER VI

HIGH RESOLUTION IMAGING OF CARDIAC BIOMAGNETIC FIELDS USING A LOW TRANSITION TEMPERATURE SUPERCONDUCTING QUANTUM INTERFERENCE DEVICE MICROSCOPE

Luis E. Fong[1], Jenny R. Holzer[1], Krista McBride[1], Eduardo A. Lima[2], Masoud Radparvar[3], Franz Baudenbacher[2]

[1]Department of Physics and Astronomy
[2]Department of Biomedical Engineering
Vanderbilt University, Nashville, TN, 37235

[3]Hypres Inc., Elmsford, NY, 10523

Adapted from:
L. E. Fong, J. R. Holzer, K. McBride, E. A. Lima, M. Radparvar, F. Baudenbacher, *Applied Physics Letters*
Vol. 84, No. 16, pp. 3190- 33192, April 2004.

6.1. Abstract

We have developed a multiloop low-temperature superconducting quantum interference device (SQUID) sensor with a field sensitivity of 450 fT/Hz$^{1/2}$ for imaging biomagnetic fields generated by action currents in cardiac tissue. The sensor has a diameter of 250 μm and can be brought to within 100 μm of a room-temperature sample. Magnetic fields generated by planar excitation waves are associated with a current component parallel to the wave front, in agreement with predictions of the bidomain model. Our findings provide a new basis for interpreting the magnetocardiogram.

6.2. Introduction

Superconducting Quantum Interference Device (SQUID) magnetometers have been used successfully to study a wide variety of bioelectric phenomena [1]. Of particular interest are magnetic fields generated by currents in the heart and the brain. Diagnostic multichannel systems detect the magnetic far field outside the body and extrapolate to the source configuration. To address the validity of the source configuration, we have to study the magnetic activity at the tissue level with cellular-scale spatial resolution [2]. High resolution imaging of biomagnetic fields will ultimately lead to a better understanding of how the magnetocardiogram (MCG) and the magnetoencephalogram (MEG) are generated and their diagnostic value. To attain high spatial resolution, the sensor must be in close proximity to the room-temperature (RT) sample. Even though high transition temperature SQUID microscopes have achieved a sample to sensor distance of 15 μm [3,4], they lack the required field sensitivity to measure the weak magnetic fields due to the distributed sources associated with bioelectric phenomena.

We recently addressed this by using sub-millimeter superconducting pickup coils supported within the vacuum space of a cryostat and coupled to the flux transformer circuit of a commercial SQUID sensor [5,6]. Although this configuration achieved a sample-to-sensor spacing of 100 μm with field sensitivities of 330 fT/Hz$^{1/2}$ for a 500 μm diameter pickup coil with 20 turns, it suffers from two major drawbacks. First, the impedance mismatch between the pick up coil and the flux transformer input coil limits the field sensitivity. Second, the cylindrical pickup coil results in a spatial averaging along the coil axis, degenerating the spatial resolution and reducing the flux due to the decay of the magnetic field with distance from the source.

6.3. Methods

One approach to overcome these drawbacks is to use Nb thin-film monolithic SQUID sensors and detect the flux induced in the bare SQUID. However, this sensor configuration is limited by small SQUID self inductances and therefore the achievable sensitivity of a few pT/Hz$^{1/2}$ is best suited for high-resolution imaging of magnetic dipole sources. In order to increase the field sensitivity further, one has to sacrifice spatial resolution and increase the effective area without increasing the inductance of the SQUID. A design, which achieves large effective areas, is a multiloop magnetometer, also known as fractional turn SQUID. This configuration was first introduced by Zimmerman [7], and later adapted by Drung *et al*.[8] who developed monolithic niobium thin-film sensors with 8 mm pickup coils for biomagnetic multichannel systems to record human MCGs and MEGs [9] and 1.5 mm diameter sensors with integrated flux transformer for nuclear magnetic resonance [10,11]. We have adapted this design and fabricated Nb thin film monolithic multiloop SQUID sensors with sub-millimeter resolutions

and field sensitivities < 1 pT/Hz$^{1/2}$, which are ideally suited for imaging biological tissue preparations.

In our approach, we use five input coils (spokes) connected in parallel with the Josephson Junctions (JJ) located in the center of the device forming the SQUID sensor. An image of our sensor is shown in Fig. 6.1. A loop around the device is used to feedback magnetic flux for operation in a flux-locked loop (FLL) configuration.

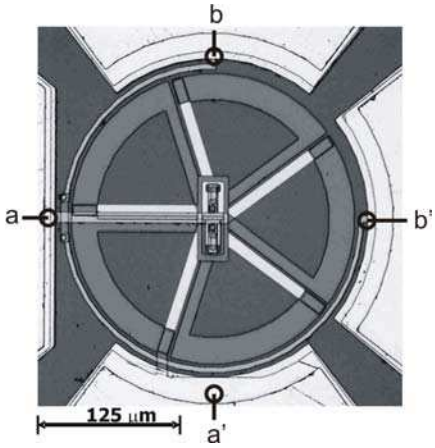

Figure 6.1: Optical picture of the multiloop magnetometer. The SQUID terminals are labeled a and a' and the integrated feedback terminals b and b'.

The noise performance of a SQUID sensor depends on its total inductance [12], and is given by the power spectral density of the equivalent flux noise:

$$S_\phi(f) = \frac{16 k_B T L^2}{R_n}, \tag{6.1}$$

where f denotes the frequency, k_B the Boltzman constant, T the operational temperature, R_n the shunt resistance and L the inductance of the device. Equation (6.1) is only approximately valid for $\beta_L = 2LI_c/\phi_0$ close to unity and in the limit of small thermal fluctuations both of

which conditions apply to our SQUID sensors. I_C denotes the critical current per junction and ϕ_0 the flux quantum. A detailed inductance calculation of the multiloop SQUID configuration, L, and the geometric effective area, A_{eff}^*, are given by[13]

$$L = \frac{L_p}{N^2} + \frac{L_s}{N} + L_j, \; A_{eff}^* = \frac{A_p}{N} - A_s, \tag{6.2}$$

where L_p and A_p are the inductance and area of the circular coil without spokes, L_s and A_s are the inductance and area of one spoke, L_j is the small parasitic inductance of the Josephson junction connection lines and N the number of spokes. Based on the optimization procedure outlined by Drung *et al*.[13] and calculations by Moya *et al*. [14], we evaluated the field sensitivity for different numbers of spokes and a fixed sensor diameter of 250 μm. The best field sensitivity was achieved with 5 spokes resulting in a total inductance of 24 pH and a geometric effective area of 7.85×10^{-3} mm^2.

The Josephson Junctions (JJs) were fabricated using a Nb/Al0x/Nb trilayer process with Mo thin film shunt resistors. With our photolithographic process, we achieved a JJ size of 2 × 2 μm^2, a JJ self-capacitance C of 0.6 pF/JJ, and a critical current per junction I_c of 15 μA at a process-specific critical current density of ~100 A/cm^2. The parameters of our device are listed in Table 6.1 and were taken from both the current-voltage (I-V) and voltage-flux (V-Φ) characteristics at 4.2 K. The noise performance was measured inside a three layer, μ-metal magnetically shielded room by operating the device in the FLL with a modulated flux of 100 kHz and a DC bias current. By using a pair of Helmholtz coils, we applied a homogeneous field which allowed us to determine the effective area, A_{eff}, of 7.86×10^{-3} mm^2, which is in good agreement with the geometrical area, A_{eff}^*.

Table 6.1: Parameters for a representative multiloop SQUID magnetometer. A_{eff} is the effective sensing area, A^*_{eff} is the geometrical area (calculated using equation 6.2), L is the SQUID inductance, I_c is the critical current, R is the shunt resistance per junction, ΔV is the peak-to-peak voltage modulation, $\beta_L = 2LI_c/\Phi_0$ is the reduced inductance parameter.

A_{eff} [mm^2]	A^*_{eff} [mm^2]	L [pH]	I_c [μA]	R [Ω]	ΔV [μV]	β_L
$7.85*10^{-3}$	$7.86*10^{-3}$	24.1	15.5	2.2	32.9	0.36

6.4. Results

Figure 6.2 shows both the magnetic field and flux noise power spectral density of our multiloop SQUID for frequencies from 0.1Hz to 1 kHz. The peaks in the spectrum are mainly associated with noise induced through the power supply of the feedback electronics and can be eliminated with tighter specifications. We achieved a magnetic flux noise, $S_\Phi^{1/2}$, of 1.7 μΦo/$Hz^{1/2}$ and an equivalent magnetic field noise, $S_B^{1/2}$, of 450 fT/$Hz^{1/2}$, both in the white noise region. We found that the 1/f noise, which generally appears for frequencies below 1 Hz, begins around 50 Hz. It has been shown that there are two main sources of 1/f noise in DC SQUIDs [15,16]: the motion of flux lines trapped in the body of the SQUID and fluctuations in the JJ critical current. At present, it is not clear which type of these most likely sources are responsible for the observed 1/f noise in our devices. However, we expect the component due to I_C fluctuations to be reduced by implementing a bias current reversal scheme [15].

The multiloop SQUID sensor was incorporated into the vacuum space of our cryostat and brought within 50-100 μm of a 25 μm thick RT sapphire window separating the sample and the vacuum space. Details of the chip mounting procedure, the cryogenic design, the magnetic

shielding and the scanning stage are described elsewhere [5,17]. The imaging properties of the sensor have been evaluated using high resolution scans of a 10 μm thin film wire with opposite scan directions. We have found no directional dependence of the image, suggesting isotropic flux collection.

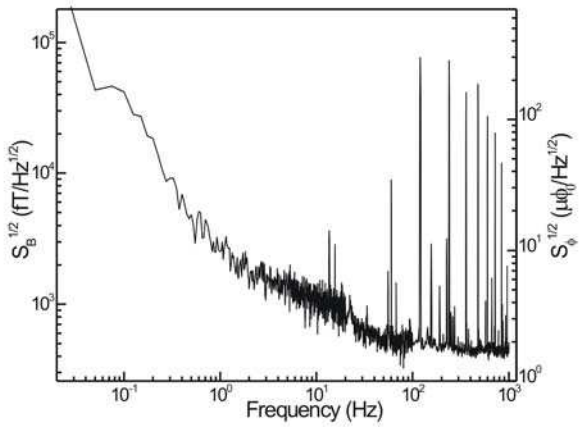

Figure 6.2: Field noise and flux noise spectral density of our multiloop SQUID magnetometer chip

To investigate the source of the MCG and validate current cardiac models, we mapped the magnetic field associated with planar excitation wave fronts on the left ventricle (LV) of a reversely perfused isolated rabbit heart pressed lightly against the sapphire window of the SQUID microscope. Using a line of three bipolar stimulation electrodes, we induced a propagating planar wave front onto the LV. The wave front geometry and position was confirmed using an optical imaging system and a voltage-sensitive dye as describe by Lin *et al.*[18] The location of the imaging area and the electrode configuration are shown in Fig. 6.3a.

In order to override the internal pacemaker, we stimulated the heart at frequencies around 3 Hz with current amplitudes of 1-2 mA, which is typically 1.5 times the diastolic stimulation

threshold. The stimulation pulse triggers the recording of a MCG. Figure 6.3a shows a typical MCG time trace (z-component) of three beats recorded with a bandwidth of 0.1 – 100 Hz. The largest peaks are due to the stimulation current and precede the actual heart beats. We estimated a signal-to-noise ratio (SNR) of 10:1 referenced to the amplitude of the heart beats. The SNR can be improved by post processing using a comb filter centered on each harmonic. The first 50 harmonics are isolated in the frequency domain and used to reconstruct the MCG. Figure 6.3c displays the MCG after signal processing.

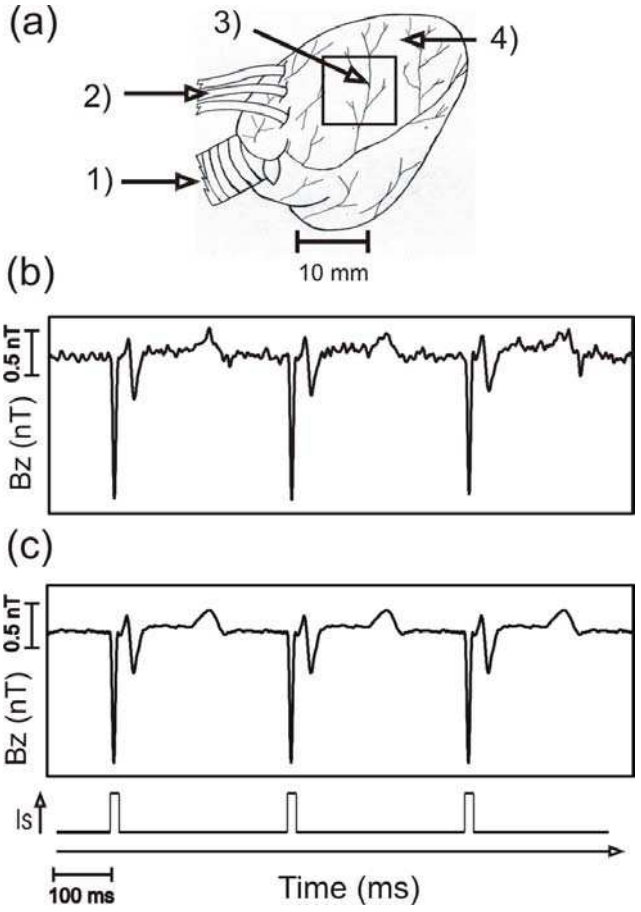

Figure 6.3: (a) Langendorff-perfused rabbit heart preparation: 1) temperature controlled perfuse inlet, 2) line of three bipolar electrodes, 3) heart's left ventricle (LV), 4) imaging area. MCG recording of three consecutive heart beats. (b) Raw and (c) post processed data. The largest peaks are from the stimulus current and are followed by ventricular depolarization and repolarization signals.

We recorded MCGs at 400 locations on a 10 mm×10 mm grid with a step size of 0.5 mm. Figure 6.4 shows the magnetic field generated by the excitation wave front 40 ms after the stimulation. The overlaid arrows represent schematically the direction and the amplitude of the action currents generating the magnetic field. The currents were calculated under the assumption of two-dimensional current distribution, as described by Roth *et al*.[19] The leading edge of the excitation wave front can be identified by a reversal of the sign of the magnetic field amplitude. The main component of the corresponding current is parallel to the depolarization wave front, which was confirmed using membrane bound voltage sensitive fluorescent dyes. This current component can only be explained in the framework of the bidomain model for cardiac tissue. In this model [19,20], cardiac tissue is represented by a three-dimensional electrical cable with distinct intracellular and extracellular spaces separated by the cell membrane. The electrical conductivities and their anisotropies in the intra- and extracellular spaces are different. The magnetic field is a superposition from currents in the intra- and extracellular space. Our experiments are the first that demonstrate the importance of the bidomain approach in describing plane wave propagation in cardiac tissue. These observations are a sensitive test of the bidomain model and are in qualitative agreement with theoretical predictions [21].

6.5. Conclusion

In conclusion, we have developed and fabricated monolithic multiloop SQUID sensors with a diameter of 250 μm and a field sensitivity of 450 $fT/Hz^{1/2}$. The SQUID sensor was incorporated in a SQUID microscope and brought within less than 100 μm of the epicardium of isolated rabbit hearts to image the action current distributions of plane waves. We found a current component parallel to the wave front which is in agreement with predictions of the

bidomain model. Consequently, the bidomain model should be the basis for forward calculations of the MCG. We anticipate the use of our system to study a wide variety of biomagnetic phenomena at the tissue level.

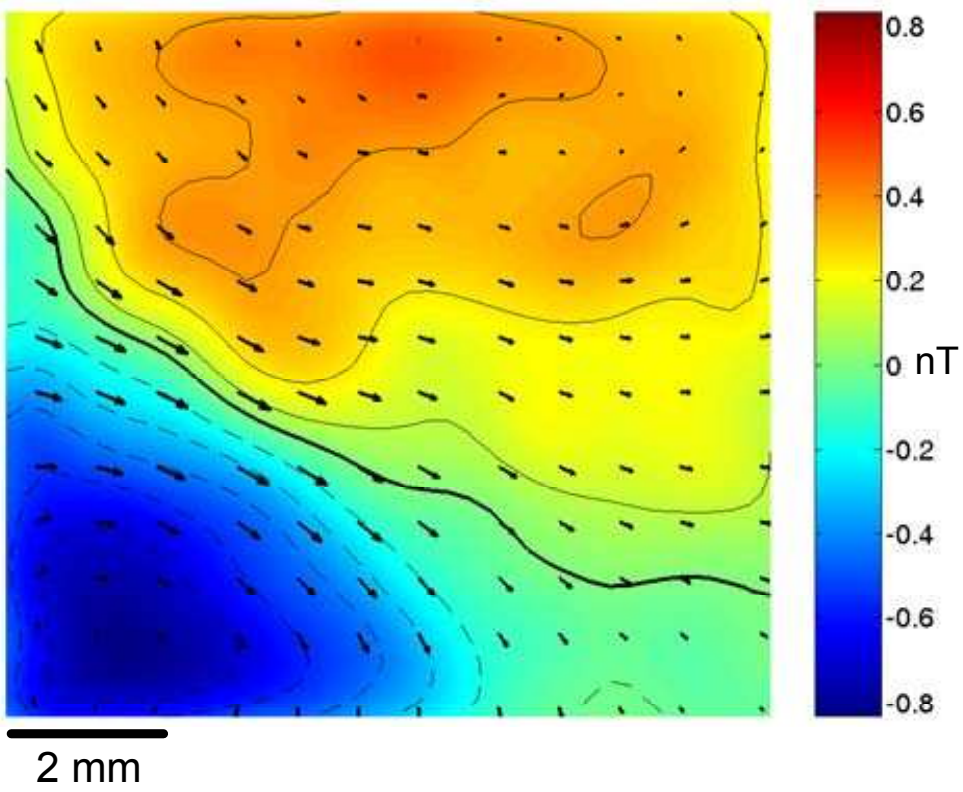

Figure 6.4: Magnetic field map 40 ms after stimulation with the corresponding isocontour lines, dashed lines represent negative fields, solid lines represent positive fields. The thick line is the zero field contour and is associated with the leading edge of the depolarization wave front. The arrows represent the calculated action current distribution.

6.6. Acknowledgments

We thank Venja Siderov and especially John Wikswo for fruitful discussions. The work was partly supported by NIH (1-R43-RR16157-01 and 2-R01-HL58241-06) and NSF – Earth Science (EAR-0004101).

6.7. References

[1] J. P. Wikswo, Jr., "Applications of SQUID magnetometers to biomagnetism and nondestructive evaluation," in *Applications of Superconductivity*. H. Weinstock, Ed. Netherlands: Kluwer Academic Publishers, 2000, pp. 139-228.

[2] J. P. Wikswo, Jr., "High-resolution magnetic imaging: Cellular action currents and other applications," in *SQUID Sensors: Fundamentals, Fabrication and Applications*. H. Weinstock, Ed. The Netherlands: Kluwer Academic Publishers, 1996, pp. 307-360.

[3] T. S. Lee, E. Dantsker, and J. Clarke, "High-transition temperature superconducting quantum interference device microscope," *Rev. Sci. Instrum.*, vol. 67, no. 12, pp. 4208-4215, 1996.

[4] Y. R. Chemla, H. L. Grossman, T. S. Lee, J. Clarke, M. Adamkiewicz, and B. B. Buchanan, "A New Investigation of Bacterial Motion: Superconducting Quantum Interference Device Microscopy of Magnetotactic Bacteria," *Biophys. J.*, vol. 76, pp. 3323-3330, 1999.

[5] F. Baudenbacher, N. T. Peters, and J. P. Wikswo, Jr., "High Resolution Low-Temperature Superconductivity Superconducting Quantum Interference Device Microscope for Imaging Magnetic Fields of Samples at Room Temperatures," *Rev. Sci. Instrum.*, vol. 73, no. 3, pp. 1247-1254, 2002.

[6] F. Baudenbacher, N. T. Peters, P. Baudenbacher, and J. P. Wikswo, "High resolution imaging of biomagnetic fields generated by action currents in cardiac tissue using a LTS-SQUID microscope," *Physica C: Super.*, vol. 368, no. 1-4, pp. 24-31, Mar.2002.

[7] J. E. Zimmerman, "Sensitivity Enhancement Of Superconducting Quantum Interference Devices Through Use Of Fractional-Turn Loops," *J. Appl. Phys.*, vol. 42, no. 11, pp. 4483-4487, 1971.

[8] D. Drung, R. Cantor, M. Peters, T. Ryhanen, and H. Koch, "Integrated Dc Squid Magnetometer with High Dv/Db," *IEEE Trans. Mag.*, vol. 27, no. 2, pp. 3001-3004, 1991.

[9] D. Drung, R. Zimmermann, R. Cantor, S. N. Erne, H. Koch, K. P. Matthies, M. Peters, H. J. Scheer, and D. Stollfuss, "A 37-Channel Dc-Squid Magnetometer System," *Clin. Phys. Physiol. Meas.*, vol. 12, pp. 21-29, 1991.

[10] A. Casey, B. Cowan, M. Digby, H. Dyball, R. Korber, J. Li, C. Lusher, V. Maidanov, J. Nyeki, J. Saunders, D. Drung, and T. Schurig, "Nuclear magnetic resonance using DC SQUIDs with APF," *Physica C-Superconductivity and Its Applications*, vol. 399, no. 3-4, pp. 93-97, 2003.

[11] D. Drung, "High-performance DC SQUID read-out electronics," *Physica C-Superconductivity and Its Applications*, vol. 368, no. 1-4, pp. 134-140, 2002.

[12] C. D. Tesche and J. Clarke, "Dc Squid - Noise and Optimization," *J. Low Temp. Phys.*, vol. 29, no. 3-4, pp. 301-331, 1977.

[13] D. Drung, S. Knappe, and H. Koch, "Theory for the Multiloop Dc Superconducting Quantum Interference Device Magnetometer and Experimental-Verification," *J. Appl. Phys.*, vol. 77, no. 8, pp. 4088-4098, 1995.

[14] A. Moya, F. J. Baudenbacher, J. P. Wikswo, Jr., and F. C. Wellstood, "Design of high resolution HTS-SQUID magnetometers for biomagnetic imaging," *IEEE Trans. Appl. Supercond.*, vol. 9, no. 2, pp. 3511-3514, 1999.

[15] R. H. Koch, J. Clarke, W. M. Goubau, J. M. Martinis, C. M. Pegrum, and D. J. Vanharlingen, "Flicker (1/F) Noise in Tunnel Junction Dc Squids," *J. Low Temp. Phys.*, vol. 51, no. 1-2, pp. 207-226, 1983.

[16] C. T. Rogers and R. A. Buhrman, "Conductance Fluctuations and Low-Frequency Noise in Josephson-Junctions," *IEEE Trans. Mag.*, vol. 19, no. 3, pp. 453-457, 1983.

[17] F. Baudenbacher, L. E. Fong, J. R. Holzer, and M. Radparvar, "Monolithic low-transition-temperature superconducting magnetometers for high resolution imaging magnetic fields of room temperature samples," *Appl. Phys. Lett.*, vol. 82, no. 20, pp. 3487-3489, 2003.

[18] S.-F. Lin, R. A. Abbas, and J. P. Wikswo, Jr., "High-resolution High-speed Synchronous Epifluorescence Imaging of Cardiac Activation," *Rev. Sci. Instrum.*, vol. 68, no. 1, pp. 213-217, 1997.

[19] B. J. Roth and J. P. Wikswo, Jr., "A Bidomain Model for the Extracellular Potential and Magnetic Field of Cardiac Tissue," *IEEE Trans. Biomed. Eng.*, vol. BME-33, No.4, pp. 467-469, 1986.

[20] C. S. Henriquez, "Simulating the Electrical Behavior of Cardiac Tissue using the Bidomain Model," *Crit. Rev. Biomed. Eng.*, vol. 2, no. 1, pp. 1-77, 1993.

[21] B. J. Roth and M. C. Woods, "The magnetic field associated with a plane wave front propagating through cardiac tissue," *IEEE Trans. Biomed. Eng.*, vol. 46, no. 11, pp. 1288-1292, 1999.

CHAPTER VII

HIGH RESOLUTION IMAGING OF MARTIAN ANCIENT MAGNETIC FIELDS

Luis E. Fong[1], Hojatollah Vali[3], Franz Baudenbacher[2], Benjamin P. Weiss[4]

[1]Department of Physics and Astronomy
[2]Department of Biomedical Engineering
Vanderbilt University, Nashville, TN, 37212

[3]Department of Earth & Planetary Sciences
McGill University, QC Canada H3A2B2

[4]Department of Earth, Atmospheric and Planetary Sciences
Massachusetts Institute of Technology, Cambridge, MA 02139

Adapted from:
L. E. Fong, H. Vali, F. Baudenbacher, B. P. Weiss,
(Manuscript in preparation)

7.1. Abstract

Magnetic measurements from the Mars Global Surveyor (MGS) of the Martian crust suggest that an intense magnetic field existed on Mars several billion years ago (Ga). ALH84001, the only Martian meteorite older than 1.3 billion years (Gyr), possesses a stable magnetization dating to 4.0 Ga or earlier. Previous paleomagnetic studies with SQUID moment magnetometers on bulk ALH84001 grains have estimated that the paleointensity of the field which magnetized was between 0.1 times that of the Earth's present field. These estimates must be treated with caution because the orientation of the magnetization in ALH84001 is spatially heterogeneous on the submillimeter scale. Because none of these methods have sufficient spatial resolution and magnetic field sensitivity to spatially resolve the microscale heterogeneous magnetization, they likely only represent lower limits on the true paleointensity. New advances in SQUID microscopy allow us to better resolve the heterogeneities. We estimate paleofield within a factor of several of that of the present-day Earth. This field could have been crustal or dynamo in origin.

7.2. Introduction

Unlike the Earth, Mars does not possess a global dynamo-driven magnetic field. However, the Mars Global Surveyor (MGS) has detected intense magnetic fields originating from the planet's crust [1]. The magnetization which is the source of these fields is most likely the product of an earlier Martian dynamo that was sufficiently vigorous to magnetize the planet's crust ~3 or more billion years ago (Ga). Figure 7.1 shows the current magnetic field distribution over the planet's surface. The magnetic field is located mainly in the ancient, heavily cratered southern hemisphere. The strongest magnetic fields, localized close to the Terra Cimmeria and

Terra Sirenium areas, reach values around 1500 nT at altitudes of ~ 200 km. Assuming the Martian crust has the same amount of ferromagnetic minerals as the Earth, such large magnetization (at least 5 Am^{-1} and likely ~10– 30 Am^{-1}) implicates an ancient core dynamo with a surface field at least one order magnitude stronger than that of the current Earth.

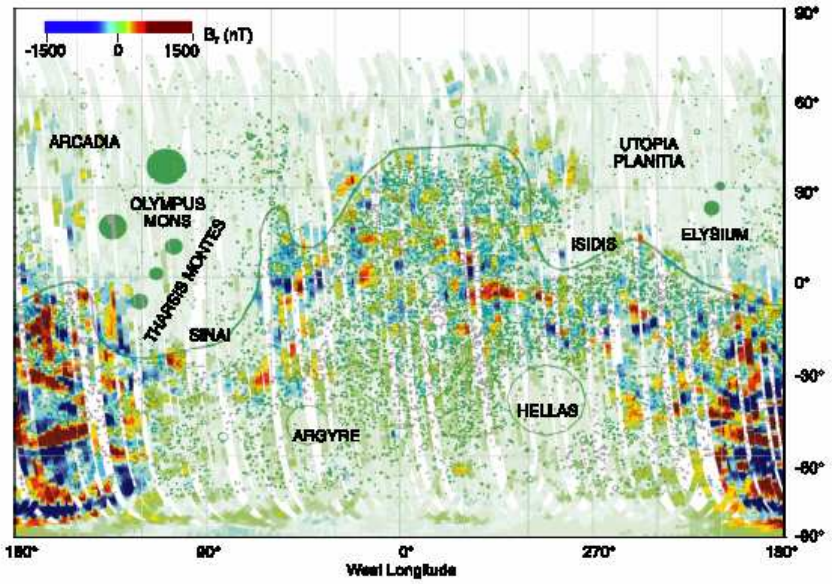

Figure 7.1: Map showing the intense magnetic fields originating from Mar's crust (Taken from [1]).

It is thought that the Martian core dynamo likely originated not long after the planet formed 4.6 billion years ago (Ga) and probably did not last more than several hundred million years. During this time, the rocks forming the crust cooled through their blocking temperatures and acquired a thermal remanent magnetization. Most arguments point towards ancient acquisition around 4.2 Gyr or earlier. Stevenson [2] presents three main arguments for an early acquisition. The first one is the lack of any magnetic signature at the ~3.9 Ga impact structure Hellas [1]. Second, it is difficult to imagine a scenario later in Mars' history where the southern

regions of Mars went through extensive heating without creating differences in the appearance of the surface with respect to regions that were not heated. This argument is supported also by the necessity of huge volumes of crust in order to explain the strong observed magnetization, rather than a thin layer of remagnetized material. Third, Weiss *et al*. [3] identified an ancient and stable magnetization (4.0 Gyr old or earlier) in Martian meteorite ALH84001.

ALH84001 is an orthopyroxene cumulate (deep-seated intrusive igneous rock) which crystallized at ~ 4.5 Ga. [4]. It was subjected to a major impact event at 4.0 Ga [5] which reset its $^{40}Ar/^{39}Ar$ chronometer [6]. Subsequently, it was ejected from Mars' surface by another impact at 15 Ma [5] and eventually landed in Antarctica, around 13,000 years ago [7]. Because of its ancient age and magnetization, ALH84001 provides a glimpse of the Martian magnetic field's early history. Recently, Weiss *et al.* [8] has shown that the interior of the meteorite has not been heated above ~ 40^{o} C for even short periods of time (< 10 min) during its ejection form Mars and transfer to the surface of the Earth.

The magnetic carriers of the meteorite are predominantly magnetite and to a lesser extent, pyrrhotite [8-10] and chromite [3]. The magnetite and pyrrhotite in ALH84001 carbonates have probably not been remagnetized since the last shock event ~ 4.0 Ga [6]. On the other hand, chromite, which is thought to be 4.5 Gy old, could provide us with information about the Martian magnetic field at even earlier times in Martian history if some grains escaped heating from the 4 Ga shock event [11]. Regardless, there is no evidence that the meteorite has been heated close to its Curie point since the formation of the magnetite in the 4.0 Gyr event. Therefore, ALH84001 preserves a stable record of an ancient Martian magnetic field.

An important caveat is that because the Martian crustal fields on the surface today reach several tens of μT, it is possible that ALH84001 was magnetized by these fields (rather than a

dynamo field originating from the core) if they were present 4 billion years ago when the meteorite was last strongly heated. Nevertheless, because their intensity still suggests that they themselves originated from a dynamo field, the magnetization in ALH84001 implies that the Martian dynamo existed at or before 4 Ga. Because we do not know whether the dynamo was still active at 4 Ga, we do not know whether paleointensity experiments on ALH84001 constrain the dynamo field or crustal fields at this time.

Several paleomagnetic studies have concluded the field intensity that magnetized the ALH84001 meteorite was around one order of magnitude smaller that the present geomagnetic field [12,13]. If ALH84001 was magnetized by a dynamo (see caveat above), then these results are very difficult to reconcile with the measurement from the actual Martian field taken with the MGS [1] since a field one order magnitude larger than the geomagnetic field is required to achieve such magnetization of the crust if the crust has a similar magnetic mineral content as the Earth. We believe that these estimates are in fact lower limits given the heterogeneous magnetic orientation of the sources in the meteorite.

Current techniques measure the magnetic field on bulk samples, which might be composed of spatially distributed magnetic dipolar sources oriented in different directions. Therefore, given the vector nature of the magnetic field and the heterogeneous spatially orientation of the magnetic sources, the measurement of the bulk sample will be the vector sum of all the microscopic sources and as a result of this, a lower limit in the estimation of the total magnetization is expected [14].

Recently, Fong *et al*. [15] have developed a new Superconducting Quantum Interference Devices (SQUID) microscope system capable of measuring the magnetic field of room temperature (RT) samples with a spatial resolution of ~ 100 μm. The system uses a monolithic

low-transition temperature niobium-based SQUID sensor. The sensor achieves field sensitivities of 1 $pT/Hz^{1/2}$, has an effective diameter of 50 μm and measures the vertical component of the magnetic field 100 μm from a RT sample. This instrument will allow us to better resolve the fine-scale magnetization in ALH84001 to infer a more accurate paleointensity reading.

7.3. Measurements and results

The sample used in our study is an oriented 30 μm thin section taken from near the meteorite's fusion crust. The thin section was mounted on a highly pure quartz glass slide using cyanoacrylic cement at room temperature in order to preserve its natural remanent magnetization (NRM). Figure 7.2 shows an optical picture of the sample.

The SQUID sensor used for the study was a bare SQUID with a 40 μm hole and a 10 μm washer, at a sample-to-sensor distance of 120 μm. The scanning area was a matrix of 437 by 225 points, with a step size of 40 μm. We first image the natural remanent magnetization of the sample. Figure 7.3 shows the NRM high resolution magnetic field map. This resolution enables us to identify clearly that the orientation of the magnetization inside the meteorite is highly heterogeneous, in agreement with our previous lower resolution images studies [3,8]. We can also recognize the fusion crust which formed during passage through Earth's atmosphere during which it was strongly magnetized by the Earth's field. The fusion crust extends $\sim \leq 1$ mm into the interior of the meteorite

One of the key features of this new technique is that it allows us to identify the magnetic components and match them with the minerals present in the sample. By comparing the NRM high resolution magnetic map to backscattered SEM (BSEM) images, we find that the magnetization in this sample is carried mostly by the fusion crust, carbonates (containing

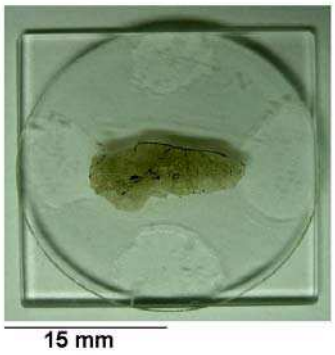

Figure 7.2: Picture of the 30 μm thin section sample of the Martian meteorite ALH84001 mounted on a highly pure quartz glass slide.

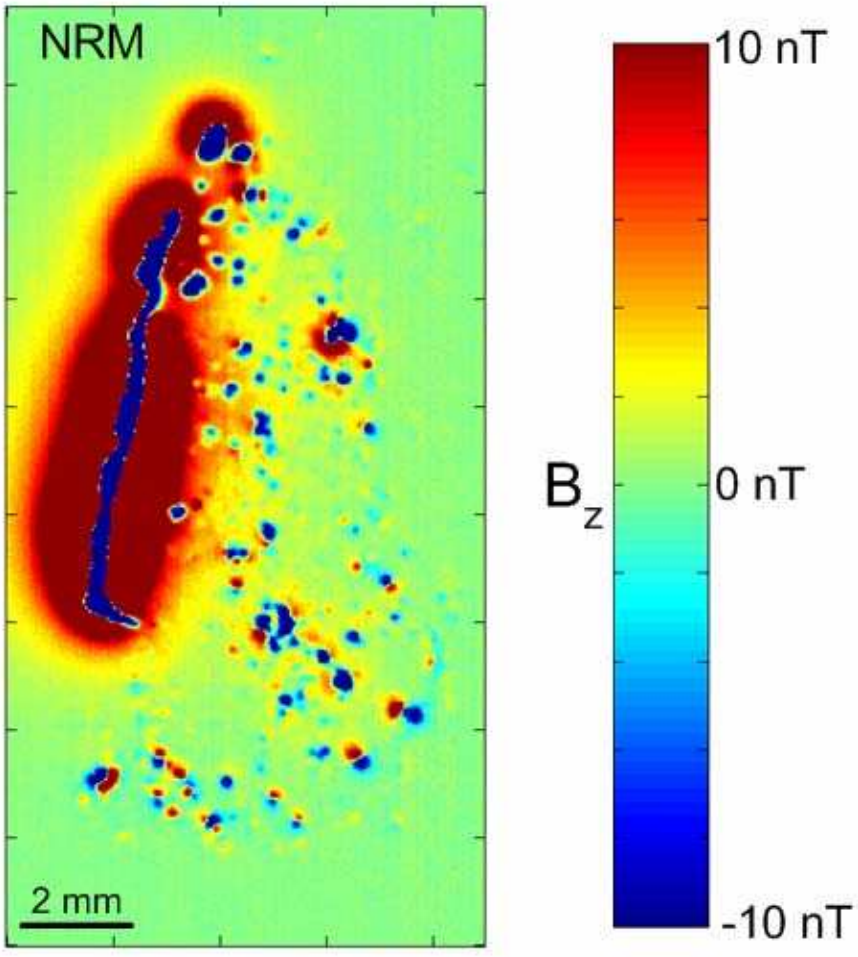

Figure 7.3: High resolution magnetic field map of the sample's NRM.

magnetite and pyrrhotite) and chromites. Figure 7.4 shows the BSEM image of the whole thin section, the superposition of the NRM magnetic map over the BSEM image, as well as some zones associated with the fusion crust, the carbonates and the chromites.

Using the SQUID microscope, we conducted standard rock magnetic studies including progressive three-axis alternating field (AF) demagnetization, progressive single-axis isothermal remanent magnetization (IRM_Z) and three-axis IRM saturation (sIRM) acquisition. These measurements provide information about the magnetization stability and also facilitate the identification of the minerals present in the sample. Figure 7.5 shows the series of AF measurements ranging from 5 mT to 100 mT. For the series of IRM_Z steps, we progressively pulse magnetized the sample in a single direction perpendicular to the surface with fields ranging from 20mT to a saturation field of 545 mT. Figure 7.6 shows the series of IRM_Z measurements. Finally, we remagnetized the sample using the same saturation field oriented in each of the other two orthogonal directions ($sIRM_x$ and $sIRM_y$). Figure 7.7 shows these measurements including the $sIRM_Z$.

The spatial resolution of the SQUID microscope allows us to correlate the magnetic image from each of the rock magnetic studies (AF, IRM_Z and sIRM acquisition) with a particular mineral present in the sample. This provides a substantial advantage, since gives us the possibility of choosing a zone associated with a mineral and keep track of its magnetic dynamics. Figure 7.8 shows the changes in individual magnetic features from some of the progressive AF demagnetization field maps.

The AF demagnetization acquisition provided indication of a strong and resistant magnetization originated at the time of the meteorite formation ~ 4 Ga. Despite the strongest AF demagnetization step at 100 mT, the sample preserves the magnetic heterogeneities (Fig. 7.6).

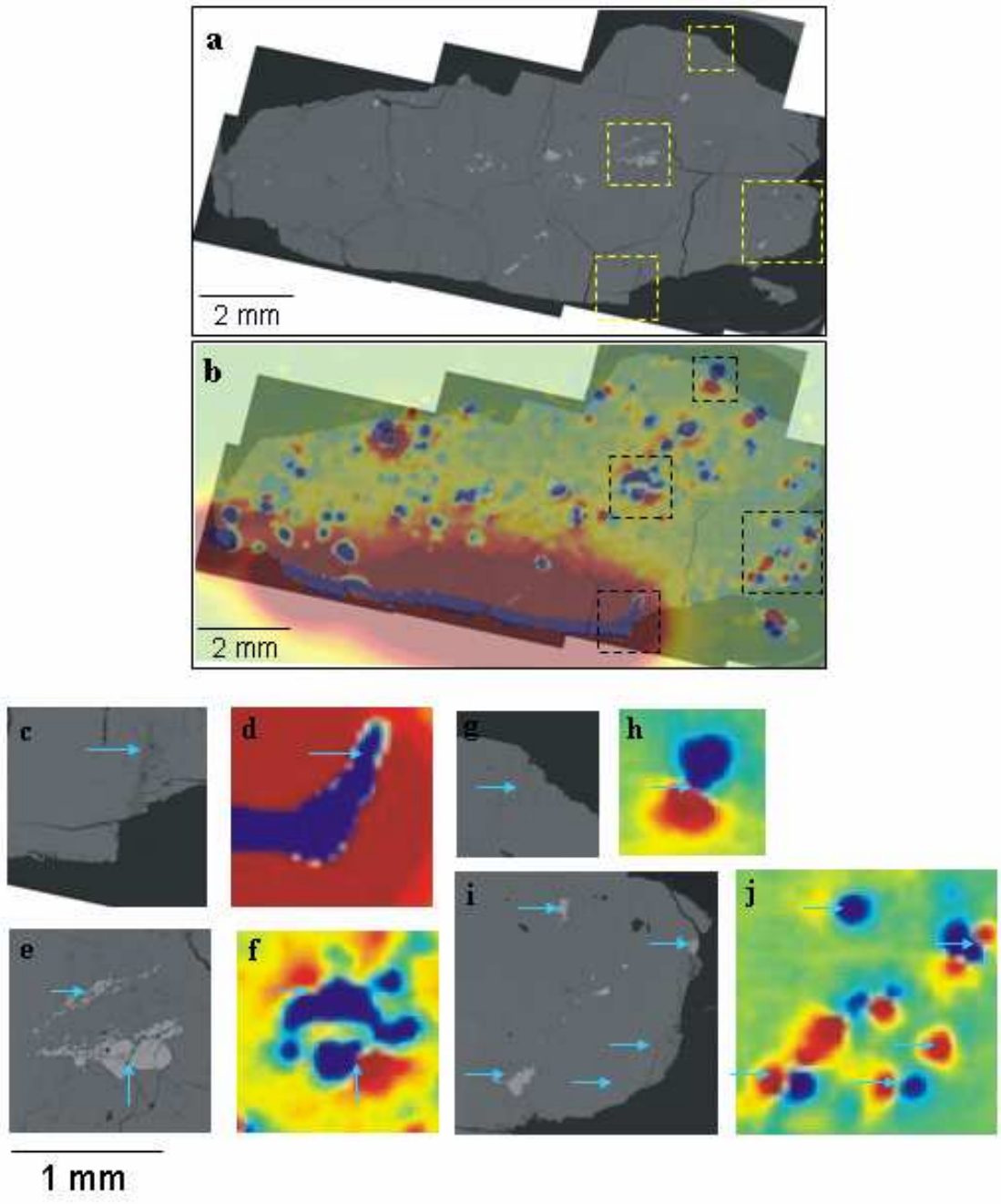

Figure 7.4: (a) Backscattered SEM image of the sample. (b) High resolution NRM magnetic field map superimposed on BSEM image. The boxed regions correspond to the selected zones shown afterwards. (c-j) Compositional and magnetic field maps of regions associated with the fusion crust (c,d) and with the presence of chromites (e,f,i,j) and carbonates (g,h,i,j). The arrows point out the same location in both images. The color scale in the magnetic field maps goes from -10 nT (blue) to 10 nT (red).

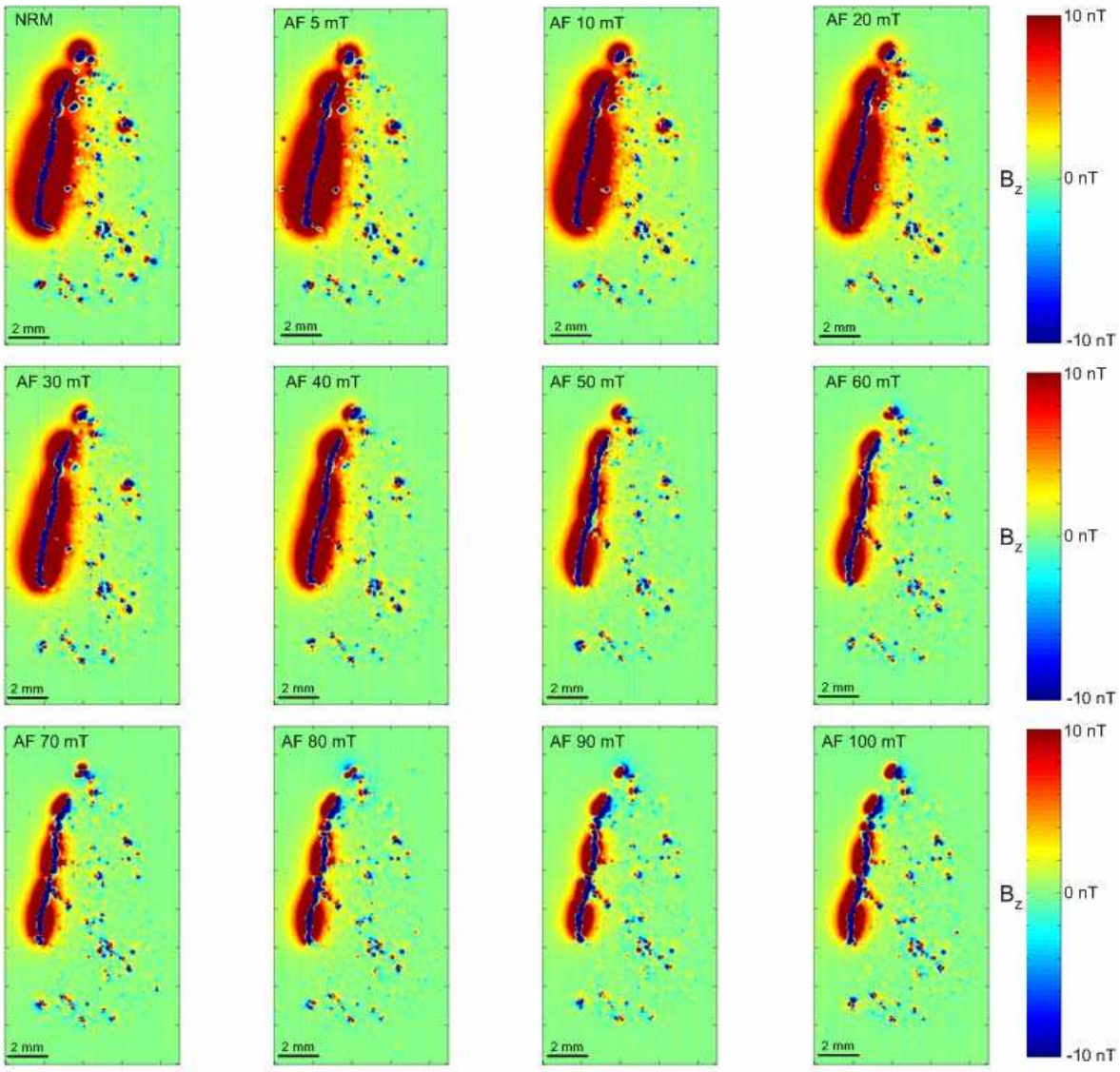

Figure 7.5: High resolution magnetic field maps of progressive three-axis alternating field (AF) demagnetization ranging from 5 mT to 100 mT.

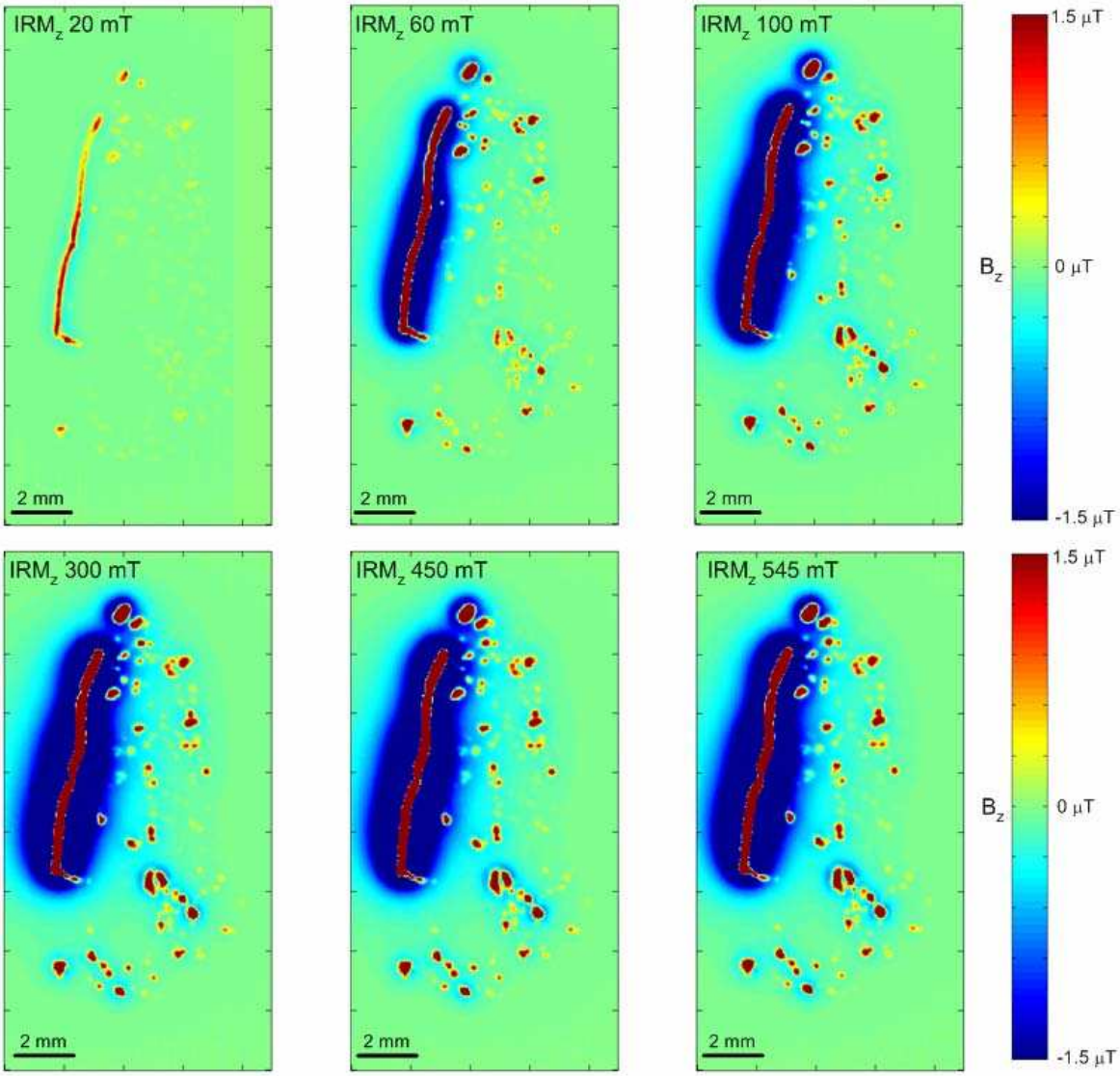

Figure 7.6: High resolution magnetic field maps of progressive single-axis isothermal remanent magnetization (IRM_Z) ranging from 2 mT up to a saturation field of 545 mT.

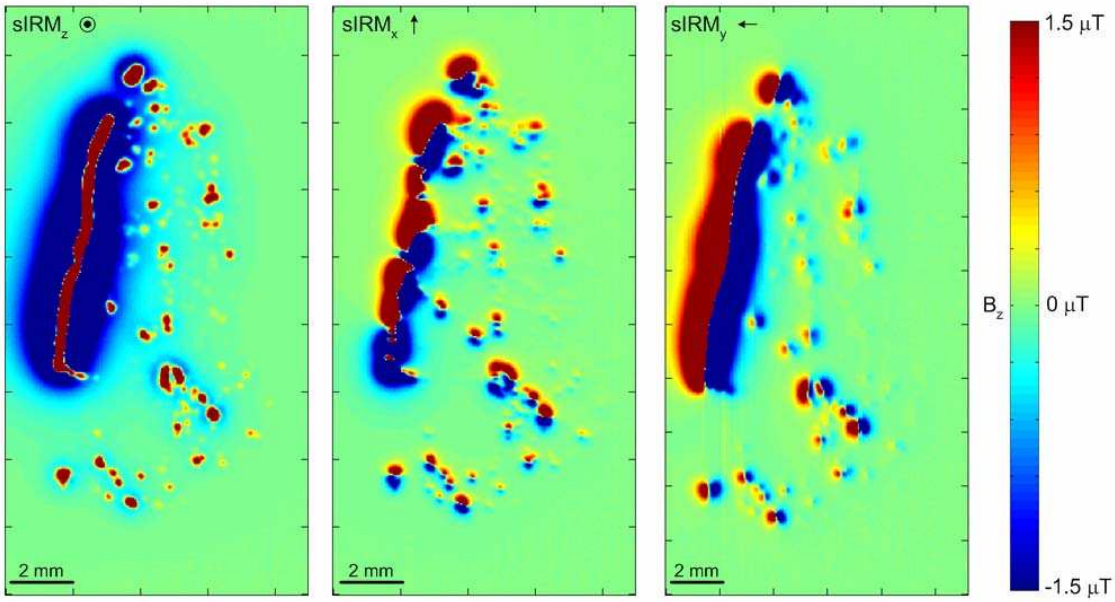

Figure 7.7: High resolution magnetic field maps of three-axis IRM saturation (sIRM) acquisition at a field of 545 mT

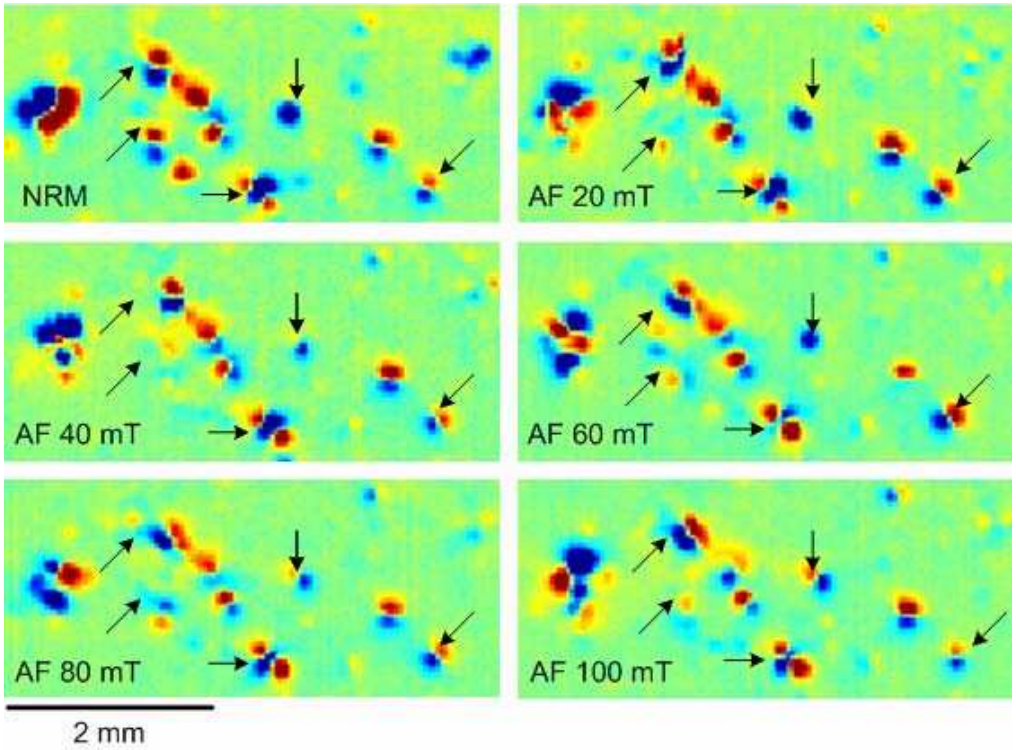

Figure 7.8: Selected region in the series of AF demagnetization maps showing the magnetic field changes of individual features (arrows).

For that reason, they were most likely created by a thermal remanent magnetization when cooled down in the presence of a Martian magnetic field and not by viscous magnetization from been exposed to an external field in the course of its travel through space or during its lifetime on Earth.

Antretter *et al*. [13] suggested that internal anisotropies might be the cause of the variable direction of magnetization in the sample. This would invalidate the conglomerate test of Weiss *et al.* [8] and also render our paleointensity experiments inaccurate. However, the three-axis sIRM acquisition (Fig. 7.7) shows that the sample perfectly magnetizes in the direction of the applied field in all three orthogonal directions. This demonstrates that ALH84001 is not significantly magnetically anisotropic. This is consistent with bulk rock anisotropy experiments using SQUID moment magnetometers [16].

A first approximation for the intensity of the field that magnetized ALH84001 is given by the NRM to sIRM ratio. Although this involves the ratio of two magnetization quantities (each of which has units of Am^2), the SQUID Microscope does not actually measure these quantities but instead measures magnetic field (with Tesla units). An inversion is required to obtain magnetization from these data. However, because magnetic field linearly depends on magnetization, a rough approximation of the NRM to sIRM ratio is obtained by dividing the NRM field map by the sIRM field map. Figure 7.9 shows the NRM to $sIRM_Z$ percent ratio. The result is presented in a logarithmic scale, since the ratio changes by several orders of magnitude at different zones. This result shows ratios in the order of ~ 0.3 to 3 % in most of the sample and ~ 3% to 30 % in some magnetic features. The results demonstrate an intense magnetic field at the time of the meteorite formation, in agreement with results previously shown by Weiss *et al.* [3], Kirschvink *et al*. [9] and recently by Gattacceca *et al*. [17]

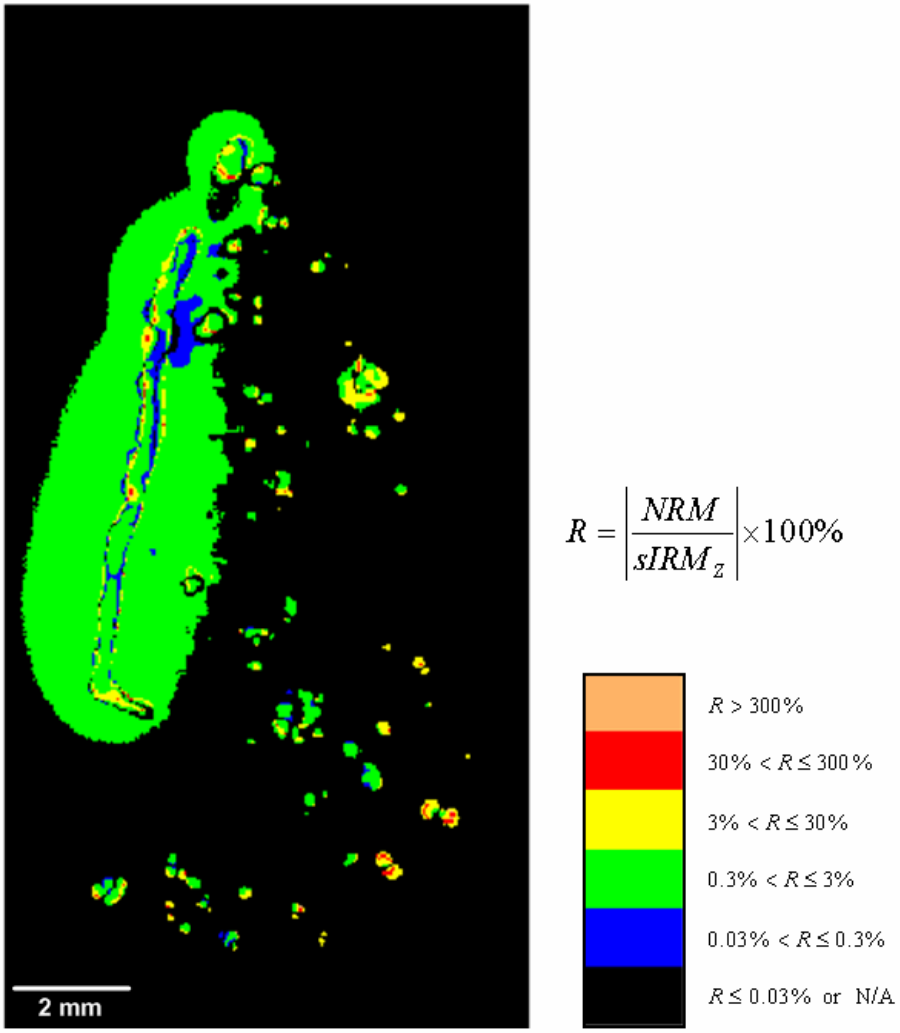

Figure 7.9: NRM to $sIRM_Z$ ratio shows an intense magnetic field at the time of the meteorite formation.

Finally, our new high resolution magnetic field data conclusively confirm the suggestion by Weiss *et al.* [3] that 4.5 Ga chromites in ALH84001 carry a stable remanent magnetization. The fact that this magnetization persists even after AF demagnetization to 100 mT shows that the magnetization has coercivities in excess of 100 mT and therefore is not a viscous remanent magnetism but rather originated on Mars. That the sample efficiently acquires IRM in the direction of the magnetizing field shows that it is not dominated by magnetic anisotropy and is

not a zero field single crystal remanence. The mechanism of magnetization in the chromite is mysterious given that many ALH84001 chromites have a Curie point of only 90 K and so should not retain a room temperature remanence [18]. We suspect that there are trace exsolved and/or spinodal ferromagnetic phases within the chromites that carry this room temperature remanence. We are currently conducting a transmission electron microscopy study of the chromites to test this hypothesis.

7.4. Conclusions

The high spatial resolution and high field sensitivity of our system allows us to make standard rock magnetism studies in individual grains at high rates in a petrographic thin section of the ALH84001 Martian meteorite for the first time. Our analysis provides supportive evidence of an intense (~50 μT) magnetic field at the time of the meteorite formation, but does not distinguish between a dynamo and a crustal field. Perhaps the most exciting result of this study is that we have now firmly established that chromites, among the most ancient grains in the meteorite, retain stable magnetization. Although the age of their magnetization remains unknown, this opens up the possibility that some of these chromites may retain records of magnetism on Mars even older than that found in the 4 Ga carbonates. Such a possibility may seem remote given that much of the meteorite was clearly strongly heated at 4 Ga as specified by whole rock $^{40}Ar/^{39}Ar$ chronometry [19]. Nevertheless, the fact that a few regions of the meteorite may have $^{40}Ar/^{39}Ar$ laser probe ages of 4.4 Ga suggests that this is not impossible. The age of the magnetization in the chromites will be a subject of future work and will likely require extensive joint magnetic studies and noble gas dating.

7.5. Glossary

Domain: the region within a crystal in which electrons align together in a single direction as a result of quantum mechanical exchange interactions.

Natural remanent magnetism (NRM): the magnetization that is observed in a ferromagnetic material prior to laboratory treatment.

Isothermal remanent magnetization (IRM): a magnetization that is acquired during short exposure to strong magnetic fields at constant temperature (e.g., by a lightning strike or in the lab from an artificial magnet). By determining the IRM field intensity required to saturate a rock's magnetization, one can infer the mineralogy of the ferromagnetic material in the rock (for example, magnetite typically saturates at 300 mT, but pyrrhotite saturates at 1000 mT).

Alternating field (AF) demagnetization: an artificial way of demagnetizing a rock by exposing it to an alternating field whose amplitude slowly decays to zero.

Coercivity: The field intensity required to remagnetize a ferromagnetic crystal at room temperature.

Curie point: the highest possible blocking temperature for a given ferromagnetic material. The Curie points of magnetite and pyrrhotite are 580ºC and 320ºC, respectively.

Saturation Isothermal remanent magnetization (sIRM): The IRM acquired after exposure to a field so intense that it magnetizes all domains in the same direction as the field. The sIRM is the maximum possible IRM that a rock can acquire.

Viscous remanent magnetism (VRM): a magnetization accumulated during long exposures to ambient magnetic fields at constant temperature. Rocks that contain a primary (e.g., thermo-) remanence typically acquire a small, younger VRM overprint that mostly affects

the grains with the smallest coercivities (< 1 mT). This occurs because remagnetization is ultimately a time- as well as temperature-dependant process.

7.6. Acknowledgments

The authors thank Eduardo Andrade Lima for stimulating discussions and for his support in the image processing and analysis. B. P. Weiss was supported by the NASA Mars Fundamental Research program and the NSF Geophysics program.

7.7. References

[1] M. H. Acuna, J. E. P. Connerney, N. F. Ness, R. P. Lin, D. Mitchell, C. W. Carlson, J. McFadden, K. A. Anderson, H. Reme, C. Mazelle, D. Vignes, P. Wasilewski, and P. Cloutier, "Global distribution of crustal magnetization discovered by the Mars Global Surveyor MAG/ER experiment," *Science*, vol. 284, no. 5415, pp. 790-793, 1999.

[2] D. J. Stevenson, "Mars' core and magnetism," *Nature*, vol. 412, no. 6843, pp. 214-219, 2001.

[3] B. P. Weiss, H. Vali, F. J. Baudenbacher, J. L. Kirschvink, S. T. Stewart, and D. L. Shuster, "Records of an ancient Martian magnetic field in ALH84001," *Earth and Planetary Science Letters*, vol. 201, no. 3-4, pp. 449-463, 2002.

[4] L. E. Nyquist, B. M. Bansal, H. Wiesmann, and C.-Y. Shih, ""Martians" Young and Old:" Zagami and ALH 84001," *Lunar and Planetary Science*, vol. 26, pp. 1065-1066, 1995.

[5] L. E. Nyquist, D. D. Bogard, C. Y. Shih, A. Greshake, D. Stoffler, and O. Eugster, "Ages and geologic histories of Martian meteorites," *Space Science Reviews*, vol. 96, no. 1-4, pp. 105-164, 2001.

[6] B. P. Weiss, D. L. Shuster, and S. T. Stewart, "Temperatures on Mars from Ar-40/Ar-39 thermochronology of ALH84001," *Earth and Planetary Science Letters*, vol. 201, no. 3-4, pp. 465-472, 2002.

[7] A. J. T. Jull, C. J. Eastoe, S. Xue, and G. F. Herzog, "Isotopic Composition of Carbonates in the Snc Meteorites Allan-Hills-84001 and Nakhla," *Meteoritics*, vol. 30, no. 3, pp. 311-318, 1995.

[8] B. P. Weiss, J. L. Kirschvink, F. J. Baudenbacher, H. Vali, N. T. Peters, F. A. Macdonald, and J. P. Wikswo, "A low temperature transfer of ALH84001 from Mars to Earth," *Science*, vol. 290, no. 5492, pp. 791-795, 2000.

[9] J. L. Kirschvink, A. T. Maine, and H. Vali, "Paleomagnetic evidence of a low-temperature origin of carbonate in the Martian meteorite ALH84001," *Science*, vol. 275, no. 5306, pp. 1629-1633, 1997.

[10] P. Rochette, J. P. Lorand, G. Fillion, and V. Sautter, "Pyrrhotite and the remanent magnetization of SNC meteorites: a changing perspective on Martian magnetism," *Earth and Planetary Science Letters*, vol. 190, no. 1-2, pp. 1-12, 2001.

[11] G. Turner, S. F. Knott, R. D. Ash, and J. D. Gilmour, "Ar-Ar chronology of the Martian meteorite ALH84001: Evidence for the timing of the early bombardment of Mars," *Geochimica et Cosmochimica Acta*, vol. 61, no. 18, pp. 3835-3850, 1997.

[12] D. W. Collinson, "Magnetic properties of Martian meteorites: Implications for an ancient Martian magnetic field," *Meteoritics & Planetary Science*, vol. 32, no. 6, pp. 803-811, 1997.

[13] M. Antretter, M. Fuller, E. Scott, M. Jackson, B. Moskowitz, and P. Solheid, "Paleomagnetic record of Martian meteorite ALH84001," *Journal of Geophysical Research-Planets*, vol. 108, no. E6 2003.

[14] B. P. Weiss, F. J. Baudenbacher, J. P. Wikswo, and Kirschvink J.L., "Magnetic Microscopy Promises a Leap in Sensitivity and Resolution," *Eos Trans. AGU*, vol. 82, pp. 513-518, 2001.

[15] Fong L.E., Holzer J.L., K. McBride, E. A. Lima, M. Radparvar, and Baudenbacher F., "High-resolution room-temperature-sample scanning superconducting quantum interference device microscope configurable for geological and biomagnetic applications," *Rev. Sci. Instrum.*, vol. (Accepted for publication) 2005.

[16] P. Rochette, J. Gattacceca, V. Chevrier, V. Hoffmann, J. P. Lorand, M. Funaki, and R. Hochleitner, "A synthesis on the magnetic properties of Martian meteorites,", XXXVI ed 2005.

[17] J. Gattacceca and P. Rochette, "Toward a robust normalized magnetic paleointensity method applied to meteorites," *Earth and Planetary Science Letters*, vol. 227, no. 3-4, pp. 377-393, 2004.

[18] B. P. Weiss, S. S. Kim, J. L. Kirschvink, R. E. Kopp, M. Sankaran, A. Kobayashi, and A. Komeili, "Magnetic tests for magnetosome chains in Martian meteorite ALH84001," *Proceedings of the National Academy of Sciences of the United States of America*, vol. 101, no. 22, pp. 8281-8284, 2004.

[19] D. H. Garrison and D. D. Bogard, "Isotopic composition of trapped and cosmogenic noble gases in several Martian meteorites," *Meteoritics & Planetary Science*, vol. 33, no. 4, pp. 721-736, 1998.

CHAPTER VIII

DISCRIMINATION OF SINGLE MAGNETIC PARTICLES BY A SUPERCONDUCTING QUANTUM INTERFERENCE DEVICE FOR MAGNETIC FLOW CYTOMETRY

Luis E. Fong[1], Eduardo A. Lima[2], David K. Schaffer[1], Franz Baudenbacher[2]

[1]Department of Physics and Astronomy
[2]Department of Biomedical Engineering
Vanderbilt University, Nashville, TN, 37235

Adapted from:
L. E. Fong, E. A. Lima, D. K. Schaffer, F. Baudenbacher,
(in preparation to be submitted to Applied Physics Letters)

8.1. Abstract

We combined microfluidic based and low-temperature superconducting quantum interference devices to identify a moving single ferromagnetic particle with a magnetic moment of 10^{-14} Am^2 at a sensor bandwidth of 2.5 KHz and a sensor-to-particle spacing of 95 μm. The channel geometry provided a mechanical modulation, which together with a detailed model lead to the identification of the amplitude and direction of the magnetic moment at each instant in time. The ability to discriminate magnetic labels according to the magnetic moment could potentially be used in high content flow cytometry applications.

8.2. Introduction

Magnetic microbeads are used in a great variety of biological and chemical assays.[1,2] Typically separation techniques can not discriminate according to the magnetic moment and can only isolate magnetically tagged analytes from their non-magnetic counterparts. Many applications, especially cell sorting, would benefit from the ability to detect and discriminate a single moving magnetic bead. Several sensors technologies with magnetic field resolutions ranging from $\mu T/Hz^{1/2}$ to several $nT/Hz^{1/2}$ have been used to detect a static single magnetic bead: giant magnetoresistance (GMR) arrays,[3] spin valve sensors,[4] Hall sensors,[5] Magnetic Force Microscopy,[6] and AMR rings.[7] All these techniques require the magnetic particle to be directly placed on or bond to the surface of the sensor. However, in applications like flow cytometry it is not possible to bring the agglomerate of cell and magnetic label in such close proximity to the sensor.

Therefore, sensors with a higher sensitivity are required to detect the agglomerates flowing pass the sensor. Superconducting Quantum Interference Device (SQUID) sensors provide higher sensitivity but have not been yet employed to detect a single magnetic bead.

Microfluidics combined with SQUID microscopy can provide the sensitivity necessary to discriminate magnetic microparticles according to their magnetic moments. This technology could have a large impact in high content cell screening applications. In this letter, we demonstrated not only the detection of a moving single magnetic particle confined in a microfluidic device, but also predicted the total magnetic moment of the particle at each instant in time.

8.3. Methods

As magnetic sensor, we use a directly-coupled low-temperature niobium based SQUID sensor with a 30 μm hole and 60 μm washer. We described the design and the characteristics of our monolithic thin film sensors previously. [8] The key parameters of our SQUID sensor are summarized in Table 8.1. The SQUID sensor is located in the vacuum space of the dewar, separated by a 25 μm thick sapphire window from a room temperature sample. We achieved sensor-to-sample distances of approximately 100 μm. [8-10] The microfluidic device structure was fabricated using poly(dimethylsiloxane) (PDMS) and replication molding.[11-13] We chose a serpentine channel geometry to provide a periodic mechanical modulation of the bead as it travels along the path of the channel. The dimensions of the channel were 25 μm wide and 15 μm deep to accommodate single magnetic particle. Figure 8.1(a) shows an image of the microfluidic serpentine channel superimposed with a picture of our SQUID sensor in the configuration used in our experiments.

We used ferromagnetic beads (SPHERO - CFM-60-5, Spherotec, Inc) as our magnetic test particles. These beads are made of chromium dioxide (CrO_2) uniformly coated with polystyrene forming micron sized particles. We chose particles with a size between 6 and 8 μm

in diameter (CFM-60-5), which have a CrO_2 content of 20 % of the total bead volume.[14] We diluted the original concentration to a 0.005 % weight to volume ratio using distilled water. The bead suspension was placed in an ultra-sonic bath for several minutes to disperse aggregates. Prior to the experiment, the suspension was magnetized using an impulse magnetizer (IM-10-30 ASC Scientific) with a pulse amplitude of 545 mT. The suspension was injected into the microfluidic channels using a static pressure generated by compressed N_2 gas. The pressure was varied in the range from 6.9 KPa to 34.5 KPa to adjust the fluid velocity. The concentration of beads was as such that in almost all cases only a single bead traveled through the channel, which we confirmed using a video camera on an inverted microscope to observe the beads flowing in the serpentine channel.

8.4. Results

The microfluidic device was auto-adhered to the 25 μm- thick sapphire vacuum window and mechanically clamped to the tail of the Dewar. Figure 8.1(b) shows a cross sectional schematic of the experimental set up. Once we have introduced the beads into the microfluidic device, we started to record time trace of the magnetic field component perpendicular to the plane of the serpentine channel. We recorded magnetic signatures of single beads traveling through the channels with an average signal-to-noise ratio of 10:1. Figure 8.2(a) and (b) shows two such magnetic signatures observed at a pressure of 27.6 KPa at a sensor bandwidth of 500 Hz and 2.5 KHz, respectively. The time traces are significantly different in shape but have common features. This can be inferred from a comparable time separation between local extrema. We also observed that the time traces were fairly symmetrical around a well defined point in time. The symmetry results from geometrical constraints and the assumption that the

magnetic beads maintain the orientation of their magnetic moments or cyclically change their moment along the serpentine channels. The geometrical constrains are the symmetrical channel layout and the position of the sensor in the center between two straight segments as shown in Fig. 8.1(a). The amplitude of the signatures varied by less than one order of magnitude. To further investigate the characteristics of the signatures, we devised a numerical model to reproduce the time traces recorded by the SQUID sensor so as to recover the magnetic moment as the bead travels through the channel.

In our model a single bead was represented as a magnetic dipole moving along a parameterized path on the *x*-*y* plane of the microfluidic channel reproducing the serpentine geometry. The simulated sensor predicted the *z*-component of the magnetic field integrated over the area of the sensor. We investigated two different schemes for the movement of the bead inside the channel. In the first one, the bead only experiences translational movement and the direction of the simulated dipole in space was kept constant along the trajectory. In the second scheme, in addition to the translational movement, the bead experiences rotation in the *x*-*y* plane while traveling the curved segments of the path. The fluid velocity is larger on the inner radius compared to the outer radius of the turns in the serpentine, which could lead to a rotation of the particle. Figure 8.3(a) and (b) shows the change in the direction of the magnetic moment of the particle through the curved segments of the path for each case.

As the particle flows through the channel we calculated, for each time instant the magnetic flux at the position of the SQUID by means of a 64-point two-dimensional Gaussian Quadrature integration algorithm evaluated over the effective area of the sensor. In total, our model is based on eight parameters: time offset, bead speed, *x* and *y* coordinates of the SQUID sensor, lift-off distance, and *x*, *y* and *z* components of the magnetic moment of the bead. The

Table 8.1: Characteristics of the SQUID sensor used for the detection of single magnetic particles. A_{eff} is the effective sensing area, $S_{\Phi}^{1/2}, S_B^{1/2}$ and $S_m^{1/2}$ are the magnetic flux noise, field resolution and moment sensitivity per unit bandwidth at 1Hz.

A_{eff}	$S_{\Phi}^{1/2}$ **(1Hz)**	$S_B^{1/2}$ **(1Hz)**	$S_m^{1/2}$ **(1Hz)** @ 100 μm
(mm^2)	($\mu\phi_O/Hz^{1/2}$)	($pT/Hz^{1/2}$)	($Am^2/Hz^{1/2}$)
6.64×10^{-3}	4.0	1.8	9.0×10^{-18}

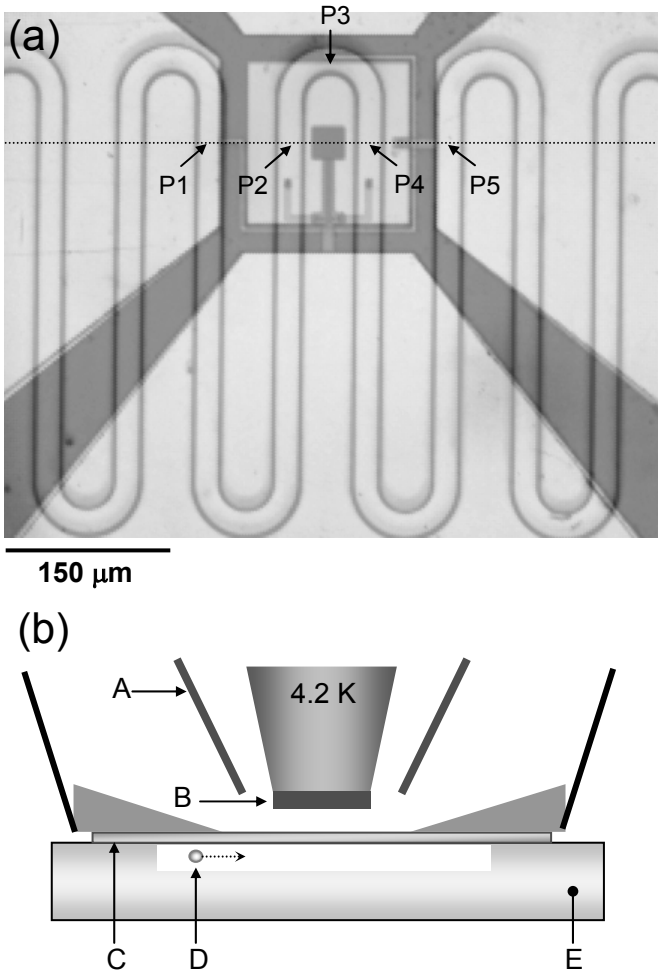

Figure 8.1: (a) Superimposed images of the microfluidic serpentine channel and the SQUID sensor. P1, P2, P3, P4 and P5 are reference points along the magnetic bead trajectory. (b) Cross sectional schematic of the microfluidic device attached to the dewar tail: (A) Radiation shield, (B) SQUID sensor, (C) 25 μm thick sapphire window, (D) Magnetic microbead and (E) Microfluidic device.

model parameters were obtained using the Nelder-Mead nonlinear optimization method to minimize the least squares difference between simulated and experimental signals. The noise on the recordings was represented in the model as white noise within the bandwidth set by the SQUID electronics.

Figure 8.3(d) shows the simulated time trace based on the assumption of a constant dipole orientation, where as Fig. 8.3(e) shows the time trace for the case where the moment changes direction according to the turns of the serpentine channels. The angle of the dipole in relation to the tangent of the trajectory was kept constant. Comparing these simulations to the experimental trace of Fig. 8.2(a), it clearly shows that the orientation of the magnetic moment does not stay constant. Another example of modeling a magnetic signature of a single particle traveling through the serpentine channel is shown in Fig. 8.3(f), which was obtained based on the measured time trace depicted in Fig. 8.2(b). Figure 8.3(c) shows the projection of the magnetic moment onto the *x-y* plane of the particle along the trajectory. These data also support a cyclic change in the direction of the orientation to be a better description of the behavior of the particle inside the microfluidic channel. (For details about the theoretical analysis of the identification of a single particle, the confirmation of the uniqueness of the solution and the minimum distance between consecutive particles for successful identification; I will recommend the reader to explore Appendix A)

The data modeling allowed us also to recover all three components of the magnetic moment which gave a total magnetic moment of $4.7 * 10^{-14}$ Am^2 and $2.8 * 10^{-14}$ Am^2 for Fig. 8.2(a) and (b), respectively. The spread in magnetic moment could be caused by field inhomogeneities during the pulse magnetization and non uniform particle characteristics. The fitting procedure was very consistent for predicting the speed of the particle and the lift-off or the

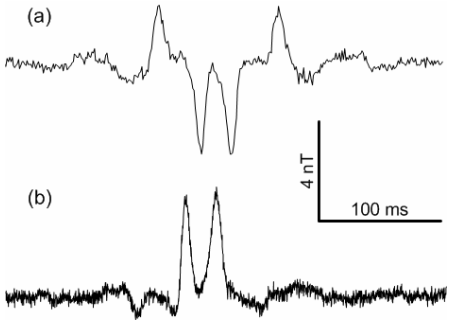

Figure 8.2: (a) and (b) Measured time traces of the magnetic field from two different magnetic particles moving through the serpentine channel.

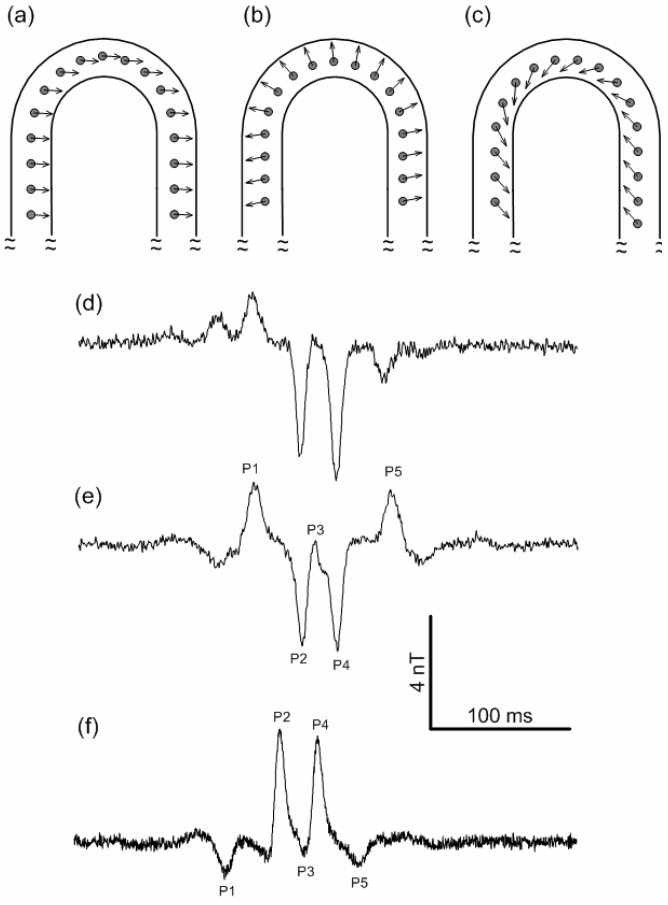

Figure 8.3: Simulated magnetic time traces and corresponding projected magnetic moments to model the experimental observations of single particles moving in the serpentine channels. (a) particle 1 fixed direction; (b) particle 1 the angle between the magnetic moment and the tangent of the path stays constant (c) particle 2 direction changes as in (b). (d), (e) and (f) time traces of the *z*-component of the magnetic field corresponding to the configuration in (a), (b) and (c), respectively. The labels P1-P5 correspond to the reference points in Fig. 8.1.

distance between the sensor and the plane of the trajectory. For the particle speed we obtained 16.3 mm/s and 15.9 mm/s, respectively. The lift-off was 95 ±3 μm. Such small variation could be expected for a 6 μm bead moving in a 15 μm high channel.

8.5. Conclusion

LTS SQUID microscopy in combination with a flow path modulation in a microfluidic device provided the sensitivity to detect and identify the magnetic moment of a single 6 μm sized ferromagnetic particle in flight with a magnetic moment in the order of 10^{-14} A m^2. Our approach will significantly enhance flow cytometry, allowing the discrimination of tagged cells according to the magnetic moment of the label for high content applications.

8.6. Acknowledgments

The authors thank John. P. Wikswo, Joseph Kirschvink, Benjamin Weiss, Anne Fu and Stephen R. Quake for stimulating discussions. The work was partly supported by the Vanderbilt Institute for Integrative Biosystems Research and Education (VIIIBRE).

8.7. References

[1] U. Häfeli, W. Schütt, J. Teller, and M. Zborowski, *Scientific and Clinical Applications of Magnetic Carriers*. New York: Plenum Press, 1997.

[2] I. Safarik and M. Safarikova, "Use of magnetic techniques for the isolation of cells," *Journal of Chromatography B*, vol. 722, no. 1-2, pp. 33-53, 1999.

[3] J. C. Rife, M. M. Miller, P. E. Sheehan, C. R. Tamanaha, M. Tondra, and L. J. Whitman, "Design and performance of GMR sensors for the detection of magnetic microbeads in biosensors," *Sensors and Actuators A: Physical*, vol. 107, no. 3, pp. 209-218, Nov.2003.

[4] H. A. Ferreira, D. L. Graham, P. P. Freitas, and J. M. S. Cabral, "Biodetection using magnetically labeled biomolecules and arrays of spin valve sensors (invited)," *J. Appl. Phys.*, vol. 93, no. 10, pp. 7281-7286, 2003.

[5] P. A. Besse, G. Boero, M. Demierre, V. Pott, and R. Popovic, "Detection of a single magnetic microbead using a miniaturized silicon Hall sensor," *Appl. Phys. Lett.*, vol. 80, no. 22, pp. 4199-4201, 2002.

[6] D. R. Baselt, G. U. Lee, K. M. Hansen, L. A. Chrisey, and R. J. Colton, "A high-sensitivity micromachined biosensor," *Proceedings of the Ieee*, vol. 85, no. 4, pp. 672-680, 1997.

[7] M. M. Miller, G. A. Prinz, S. F. Cheng, and S. Bounnak, "Detection of a micron-sized magnetic sphere using a ring-shaped anisotropic magnetoresistance-based sensor: A model for a magnetoresistance-based biosensor," *Appl. Phys. Lett.*, vol. 81, no. 12, pp. 2211-2213, 2002.

[8] F. Baudenbacher, L. E. Fong, J. R. Holzer, and M. Radparvar, "Monolithic low-transition-temperature superconducting magnetometers for high resolution imaging magnetic fields of room temperature samples," *Appl. Phys. Lett.*, vol. 82, no. 20, pp. 3487-3489, 2003.

[9] Holzer J.R., Fong L.E., Sidorov V.Y., Wikswo J.P., and Baudenbacher F., "Magnetic and fluorescent imaging of plane waves in cardiac tissue reveals currents parallel to the wave front," *Accepted to Biophysical Journal*, 2004.

[10] F. Baudenbacher, N. T. Peters, and J. P. Wikswo, Jr., "High Resolution Low-Temperature Superconductivity Superconducting Quantum Interference Device Microscope for Imaging Magnetic Fields of Samples at Room Temperatures," *Rev. Sci. Instrum.*, vol. 73, no. 3, pp. 1247-1254, 2002.

[11] D. C. Duffy, J. C. McDonald, O. J. A. Schueller, and G. M. Whitesides, "Rapid prototyping of microfluidic systems in poly(dimethylsiloxane)," *Analytical Chemistry*, vol. 70, no. 23, pp. 4974-4984, 1998.

[12] Y. N. Xia and G. M. Whitesides, "Soft lithography," *Annual Review of Materials Science*, vol. 28, pp. 153-184, 1998.

[13] A. Y. Fu, C. Spence, A. Scherer, F. H. Arnold, and S. R. Quake, "A microfabricated fluorescence-activated cell sorter," *Nature Biotechnology*, vol. 17, no. 11, pp. 1109-1111, 1999.

[14] "Product catalogue, Spherotech, Inc. Libertyville, IL,*www.spherotech.com*," 2004.

CHAPTER IX

INTRACELLULAR AXIAL CURRENT IN CHARA CORALLINA REFLECTS THE ALTERED KINETICS OF IONS IN CYTOPLASM UNDER THE INFLUENCE OF LIGHT

F. Baudenbacher[2], L. E. Fong[1], G. Thiel[3], V. Jazbinsek[3], J. R. Holzer[1], A. Štampfl[4], Z. Trontelj[4]

[1]Department of Physics and Astronomy
[2]Department of Biomedical Engineering
Vanderbilt University, Nashville, TN, 37235

[3]Institute for Botany, Plant Biophysics
Darmstadt University of Technology, D- 64287,
Darmstadt, Germany

[4]Physics Department
IMFM, University of Ljubljana, 1000-Ljubljana, Slovenia

Adapted from:
L. E. Fong, J. R. Holzer, K. McBride, E. A. Lima, M. Radparvar, F. Baudenbacher, *Biophysical Journal*
Vol. 88, pp. 690–697, January 2005.

9.1 Abstract

Recent experiments demonstrate that the concentration of Ca^{2+} in cytoplasm of *Chara corallina* internodal cells plays important role in electrical excitation of the plasma membrane. The concentration of free Ca^{2+} in the cytoplasm $[Ca^{2+}]c$ is also sensitive to visible light. Both phenomena were simultaneously studied by noninvasive measuring action potential (AP) and magnetic field with a superconducting quantum interference device magnetometer in very close vicinity of electrically excited internodal *C. corallina* cells. A temporal shift in the depolarization maximum, which progressively occurred after transferring cells from the dark into the light, can be explained by the extended Othmer model. Assuming that the change in membrane voltage during the depolarization part of AP is the direct consequence of an activation of $[Ca^{2+}]c$ sensitive Cl^- channels, the model simulations compare well with the experimental data. We can say that we have an example of electrically elicited AP that is of biochemical nature. Electric and magnetic measurements are in good agreement.

9.2. Introduction

The green algae from the family of the *Characeae* have a long history as a model system for ion transport in plants [1-4]. Experimental work was favorable given the very large geometry of a single internodal cell and the many possibilities of manipulating these cells with microsurgery [5,6]. In this sense, the species *Chara corallina* is the plant equivalent to the squid axon in the study of ion transport in plants.

The recent phylogenetic analysis of the *Characeae* has again strengthened the model character of *Chara*. This family of green algae is now seen as the ancestor of higher plants [7,8]. Hence, an investigation of the physiological processes in *Chara* is interesting from an

evolutionary point of view. Also, data from the simple single-cell system can be seen as a common primitive mechanism for comparable effects in higher plants.

The plasma membrane of *Chara corallina* is electrically excitable. Depolarization of the membrane more positive than a critical threshold elicits a propagated action potential (AP) [9]. The bulk rise in membrane conductance, which underlies this transient membrane depolarization, is due to a short-lasting activation of Cl^- and K^+ channels [10,11]. Because of the thermodynamic conditions, this leads to an efflux of KCl from the cytoplasm into the external medium [12]. Hence, the plant action potential is different from the AP in animal cells; it is osmotically active. This osmotic activity seems to be fundamental for the physiological role of the AP in *Chara* where it is apparently involved in the regulation of the internal pressure (turgor pressure) in the cell [13,14].

The mechanism underlying the electrical stimulation of the AP is still not fully understood, but a rise in cytoplasmic Ca^{2+} undisputedly plays a key role [15-17]. This rise in Ca^{2+} is thought to activate Ca^{2+}-sensitive Cl^- channels [10,18]—the process that generates the depolarization. The activation of K^+ channels, which support repolarization, follows either as a result of the depolarization or in response to the rise in Ca^{2+} [10,11].

The classical view is that Ca^{2+} enters the cytoplasm via voltage-dependent channels [19]. Other investigations have revealed that the threshold for excitation is posed by a quasi all-or-none type liberation of Ca^{2+} from internal stores [17,20]. In this sense, the AP in *Chara* occurs not to function like a classical Hodgkin Huxley (HH) type AP. This means that the AP is not entirely based on the time- and voltage-dependent activation properties of plasma membrane ion channels but on a complex signal transduction cascade. Similar mechanisms of membrane

excitation, which are based on Ca^{2+} release from internal stores, are also well known from animal cells where they are found in muscles [21] and even some neurons [22].

The latter type of a ‘‘chemical’’ action potential was in the past well-described by models, which include a nonlinear dynamic interplay of cytosolic Ca^{2+} ($[Ca^{2+}]c$) and second messenger-stimulated release of Ca^{2+} from internal stores [23]. The same modeling approach was also suitable to simulate a large spectrum of phenomena related to membrane excitation in *Chara* [20]. One parameter in this model, which is predicted to effect the kinetics of Ca^{2+} mobilization and hence the kinetics, is the cytoplasmic concentration of Ca^{2+} before stimulation.

To further prove the validity of the model, we therefore examine in this study the kinetics of the AP under conditions in which $[Ca^{2+}]c$ is altered. This can be easily done by transferring the plants from the dark into the light, because it is known that $[Ca^{2+}]c$ is in these cells reduced under the influence of light [24,25].

This work also has a methodological aspect because the AP in *Chara* is examined with a noninvasive method by recording the magnetic field in the vicinity of a *C. coralline* internodal cell under different illumination conditions. According to Ampere’s or the Biot-Savart law, measured magnetic field in the vicinity of intra- and extracellular currents carries information on these currents. Measurement of cellular magnetic field is also connected to the AP [26,27] and can be thus a supplemental method to other electrophysiological investigations.

9.3. Materials and methods

C. corallina was cultured in the laboratory in a 90-liter aquarium (~60 cm high) filled with artificial pond water (APW) (0.1 mM KCl, 0.5 mM $CaCl_2$, 1 mM NaCl). The plants were grown on a layer of lake mud. A single internodal cell was prepared a day or two before the

experiments and placed in APW + 2 HEPES, pH = 6.8–7.0 (NaOH). All salts were from Sigma Chemical (St. Louis, MO).

The internodal cell was held in a horizontal Plexiglas half-tube, similar to that previously described [28] and is schematically shown in Fig. 9.1 (*side view*) and Fig. 9.2 A (*top view*) . The leveling stage allowed the bath to be moved up and down to adjust the distance between the cell and the tail of the superconducting quantum interference device (SQUID) microscope Dewar vessel. A 10 μm thick Mylar film prevented contact between the cell and the SQUID microscope sapphire window and stabilized the position of the internodal *C. corallina* cell during scanning. One end of the internodal cell was mounted in a small Plexiglas compartment so as to electrically isolate this end of the cell (the left end in Fig. 9.1) from the bath with a petroleum jelly seal (Fig. 9.1). The Plexiglas compartment was filled with 100 mM KCl that served as a reference electrode (the K^+ anesthesia technique) for parallel electrical measurements of the AP [28]. We had to apply this technique so as not to disturb the SQUID sensor with ferromagnetic impurities of microelectrodes and the cell manipulating device. The Plexiglas half-tube with the internodal *C. corallina* cell and the 100 mM KCl compartment was submerged in a shallow Plexiglas container with the dimensions $20 \times 14 \times 4$ cm^3 (Fig. 9.1). Using Ag/AgCl electrodes, we measured the resting potential as the potential difference between the APW and the KCl compartment before stimulation. Before the measurements, both recording electrodes were immersed in the KCl compartment to cancel the junction and offset potential. We needed *C. corallina* internodal cells that were at least 8 cm long to allow simultaneous measurement of the electric potential differences (AP) and the associated magnetic field due to action currents (AC). For the measurements reported here, we selected internodal cells that were up to 15 cm long with diameters between 0.8 and 1.1 mm. The amplitude of the square wave electric stimulus with

duration of 40–80 ms was adjusted above the threshold for the AP eliciting. The inter-stimulus interval was at least 120 s, and most cells were responsive to several tens of stimulations.

The bath temperature was carefully monitored during each experiment and was maintained at 20.0^{o}C. All measurements were performed in an air-conditioned, magnetically shielded room. During an average 2-h measuring session, the temperature varied by only 0.2^{o}C.

The cell illumination was provided by a light source with a spectrum similar to daylight with 5–10 Wm^{-2} delivered to the cell by a fiber-optic bundle that passed through an opening into the magnetically shielded room to eliminate power supply noise of the light source.

By measuring magnetic fields in the vicinity of a *C. corallina* internodal cell after the AP was electrically elicited, we basically measure the contribution of total ionic current, associated with the propagating AP. The measured internodal *C. corallina* cell is in APW bath, and extracellular ionic currents, caused by the AP propagation along the cell, are spread through the whole APW volume. Their density is very small and their contribution to the measured magnetic field is negligible. Practically only the magnetic field due to axial intracellular current—we can call it the action current—can be measured. Taking the maximal intracellular current 1 μA and the distance from the cell geometrical axis 2 mm, we obtain by applying Ampere's law for the maximal value of magnetic field 10^{-10} T = 100 pT. To measure this magnetic field or even smaller magnetic fields, a very sensitive magnetic field sensor is needed. We can choose between a SQUID magnetometer [29], covering an area of several 100 cm^2 and a single SQUID magnetometer with a small detection coil (usually called a pickup coil) in a configuration that comes extremely close to the measured object—SQUID microscope [30]. The second alternative enables us to obtain a high signal/noise ratio (small distance from the detection coil to the cell) and high spatial resolution (due to the small diameter of detection coil).

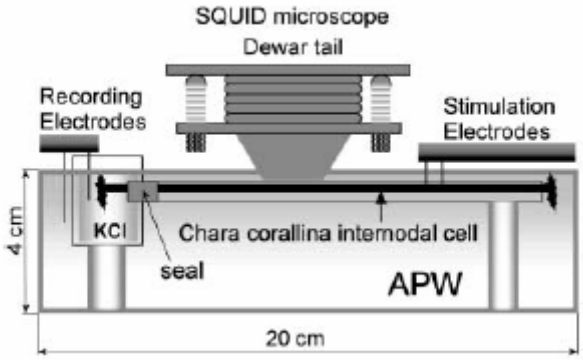

Figure 9.1: Schematic experimental setup (*side view*) used for electric and magnetic measurements on *Chara corallina* internodal cell. The Plexiglas holder supporting the cell is terminated on the left side in a sealed compartment to record the transmembrane potential.

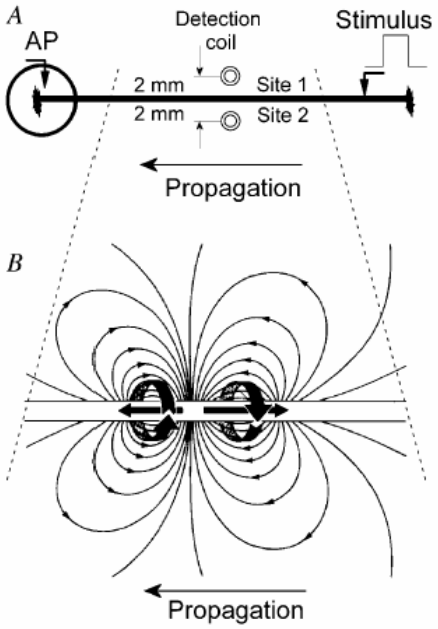

Figure 9.2: (*A*) Schematic of *Chara corallina* internodal cell (*top view*) indicating the location of the stimulus, the AP, and the magnetic field measurement sites. (*B*) Schematic distribution of intracellular current (two current dipoles within the internodal cell) and extracellular current (*thin lines*) for a propagating AP along the *Chara corallina* internodal cell. The contribution of the extracellular current to the measured magnetic field is negligible in an extended bath. The magnetic field due to the intracellular current in the vicinity of the internodal cell is represented as a ring around the cell. The depolarized part of the cell is shown on the left side, the repolarized on the right side.

In our SQUID microscope design, a hand-wound niobium detection coil is coupled to a commercially available low temperature SQUID sensor. The SQUID sensor and the detection coil are in the vacuum space of the cryostat separated typically by ~ 100 μm from the room-temperature sample by a thin sapphire window. A computerized nonmagnetic scanning stage with submicron resolution in combination with a tripod leveling system allows samples to be scanned at levels of 10 μm below the sapphire window. For a 20-turn 500 μm diameter detection coil, we achieve a field sensitivity of 350 $fT/Hz^{-1/2}$ and for a 40-turn 1 mm diameter coil, 50 $fT/Hz^{-1/2}$ for frequencies above 1 Hz for the vertical component of the magnetic field. The voltage output of the SQUID electronics corresponding to the vertical magnetic field component generated by propagating AC was recorded at a bandwidth of DC-500 Hz for a period of 30 s at a position along the cell where the magnetic signal was maximal. The SQUID microscope, the sample, and the scanning stage were housed in a three layer, μ-metal magnetically shielded room (Vacuumschmelze, Hanau, Germany) to eliminate the influence of near-DC and higher frequency noise sources.

9.4. Results

9.4.1. Measurements

Before the first measurement, the optimal position of the SQUID microscope detection coil has been determined. The coil was positioned 1–2 mm lateral and ~ 200 μm above the *C. corallina* internodal cell (Fig. 9.2 *A*) where the vertical component of the magnetic field was readily detectable (at least several 10 pT at maximum). The sapphire window of the SQUID microscope was positioned ~ 100 μm above the cell surface, resulting in a distance between the detection coil and the cell surface of ~ 200 μm. The signal/noise ratio was 5:1 or better for a

single scan. A high temporal density of measurement points allowed us to improve the signal/noise ratio by averaging. We regularly confirmed that the signal reversed polarity (as expected for this geometry) after the scan crossed the geometrical axis of the cell.

Keeping the SQUID magnetometer's detection coil in position, denoted as ''Site 1'' in Fig. 9.2 *A*, we measured the magnetic field as a function of time. The result is shown in Fig. 9.3 *A*. Moving the bath with the *C. corallina* internodal cell so that the detection coil reaches position ''Site 2'' in Fig. 9.2 *A* causes the signal polarity to change (Fig. 9.3 *B*). Small differences in peak amplitudes between Fig. 9.3 *A* and *B* reflect scattering between two measuring sessions; a small deviation from symmetrically located measuring points possibly contributes to these differences as well.

The AP was measured simultaneously at a point along the cell 50 mm away from the detection coil position and is shown in Fig. 9.3 *C*. The separation of magnetic and electric measuring points leads to a time shift of 1.1–1.2 s. From these values, the AP propagation velocity can be calculated to be ~ 4 cm/s, which is in good agreement with the previous results [28]. Before and during these measurements, the *C. corallina* internodal cell was kept in darkness for at least 1 h. The detection coil was placed 2 mm (Fig. 9.3 *B*) and –2 mm (Fig. 9.3 *A*) lateral to the internodal cell surface. The vertical distance from the detection coil to the cell surface was 200 μm. The measurements shown in Fig. 9.3 are a single-shot measurement with no averaging of the data.

The dotted line in Fig. 9.2 *A* denotes a small part of the internodal cell, which we assume is sufficiently long to cover both the repolarized and the depolarized area in this part of the internodal cell. The corresponding AC is in the form of two current dipoles (called also axial current elements) and is drawn as two thick arrows within the cell (Fig. 9.2 *B*). The left one

belongs to the depolarized part and the right one to the repolarized part of the cell. The magnetic field around each current element is for clarity shown as one broad line in the ring form around the current element according to Ampere's law. Both magnetic fields have different directions since the current elements are pointing in opposite directions. Considering the constant AP propagation velocity c of 4 cm/s and the duration of depolarization 1 s, we get for the depolarized part of the cell $x = ct = 4$ cm. This means that for measurements very close to the *C. corallina* internodal cell, we have a similar situation as in the case of observing the magnetic field of a straight wire that is conducting electric current.

The relation between AP and AC (and corresponding magnetic field) in different nerve cells [27,31,32] and also in an excited single internodal cell of *C. corallina* [28,33] was studied in detail. Briefly, in all studied cases, we observe that the peak forward action current occurs approximately simultaneously with the maximum time derivative of the AP, and the maximum backward action current occurs at the most rapid change in the AP during repolarization. The time of the peak AP corresponds to the zero-crossing between the forward and backward phases of the AC. The correlation of these AP and AC features are more pronounced in our measurements in this study since the small SQUID microscope detection coil can be placed closer to the cell. Fig. 9.3 illustrates these relations. However, we have to take into account in this particular case that AP and magnetic field were not measured at the same point along the cell (there is ~ 1.1 s time difference between both signals).

Under constant illumination and temperature, the transmembrane potential and the magnetic field generated by AC revealed only small variations either when different cells or when one *C. corallina* internodal cell was measured repetitively.

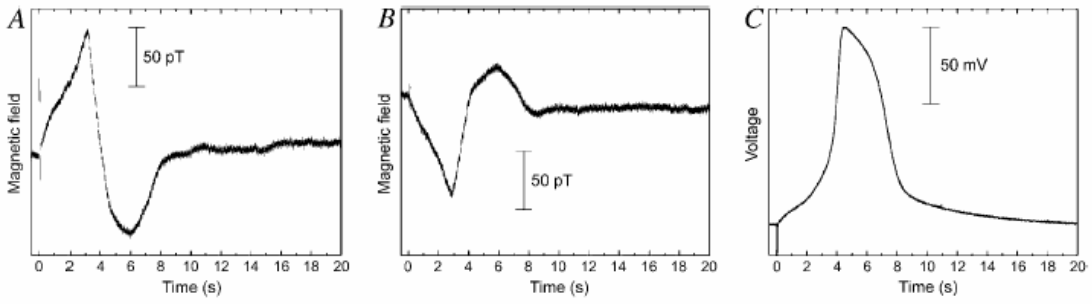

Figure 9.3: (*A*) Magnetic field measured at Site 2 as indicated in Fig. 9.2 *A*. (*B*) As in Fig. 9.3 *A* but at Site 1 indicated in Fig. 9.2 *A*. (*C*) AP recorded by the K^+ anesthesia technique.

Fig. 9.4, traces ***a–i***, show the time dependence of the vertical component of magnetic field measured at $y = 2$ mm lateral to the cell's geometrical axis under different illumination conditions. In this series of experiments, the internodal cell was in darkness for 60 min before the first measurement of AP propagation. Fig. 9.4, trace a, shows the magnetic field generated by AC just before the light was turned on. Subsequent recordings were done under constant illumination after particular time intervals as shown in Fig. 9.4, traces ***b–e***. It can be seen that, as a response to illumination, the temporal evolution of the magnetic field changes over a period of < 1 h before reaching a new steady state. Most pronounced is the time shift of the positive peak of the magnetic signal associated with the depolarization. The negative peak associated with the repolarization is less expressed.

The temporal characteristic of the magnetic field is reversible. Upon transferring the cell back from light into darkness, the temporal field changes became progressively closer to the initially measured magnetic field as shown in the sequence Fig. 9.4, traces ***f–i***.

Parallel electrical measurements (Fig. 9.5, traces ***b–e*** and ***f–i***) demonstrate a similar dependence of the AP time evolution on light/darkness. A transition of a cell from darkness to light prolonged the duration of the membrane depolarization for ~ 2 s after a transitional period

of ~ 20–30 min on average. The depolarization time prolongation was accompanied by an increase in the depolarization peak of ~ 10–15%. This can be attributed to the hyperpolarization of the resting potential under illumination [34].

The time shifts extracted from the magnetic measurements from eight cells are shown in Fig. 9.6. To better compare different cells, we introduced a normalization as a dimensionless quantity, $\alpha = \Delta t/to$. Here, Δt is the light-induced delay with respect to the initial AC measured as the temporal shift in the depolarization maximum and to the time of the depolarization maximum for a particular illumination/darkness condition relative to the stimulus. We see that an increases with the duration of illumination when cells are transferred from darkness into constant light. Fig. 9.7 summarizes the dependence of the average value of the normalized time delay a as a function of illumination time obtained from AP measurements on 15 *C. corallina* internodal cells. Figs. 9.6 and 9.7 demonstrate the behavior of α obtained from magnetic field (AC) and AP measurements of cells exposed to different durations of illumination. Both curves are almost identical. In addition, we also see that error bars in Fig. 9.7 are shorter (here were considered more cells).

The reversible effect of light/dark transitions on the kinetics of membrane excitation suggests a coupling between photosynthesis and membrane excitation. To examine this hypothesis, we have measured the influence of a common photosynthesis inhibitor, DCMU (3,-(3,4-dichlorophenyl)-1, 1-dimethylurea), at a concentration of 10 μM on the kinetics of excitation. In this case, a *C. corallina* cell was exposed to light for a period of 60 min in the presence of DCMU in the bath solution. After ~ 20 min, the magnetic signal intensity started to decrease in a way reminiscent of the behavior in the dark, as expected from our data in the illumination studies. Two cells were tested with both showing the same behavior.

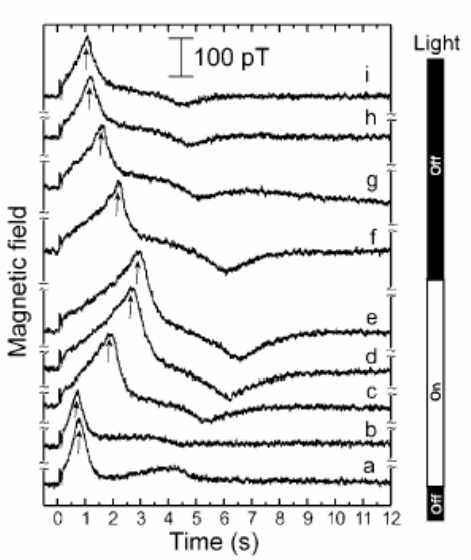

Figure 9.4: Recordings of the time-dependent vertical component of the magnetic field generated by a propagating AC measured as a function of illumination starting after 1 h dark accommodation. Trace **a**, light off; trace **b**, 10 min light on; trace **c**, 20 min light on; trace **d**, 30 min light on; trace **e**, 40 min light on (here we waited for an additional 20 min to complete 1 h in the light accommodation); trace **f**, 10 min light off; trace **g**, 20 min light off; trace **h**, 30 min light off; and trace **i**, 40 min light off. Small arrows indicate where the temporal shift was observed.

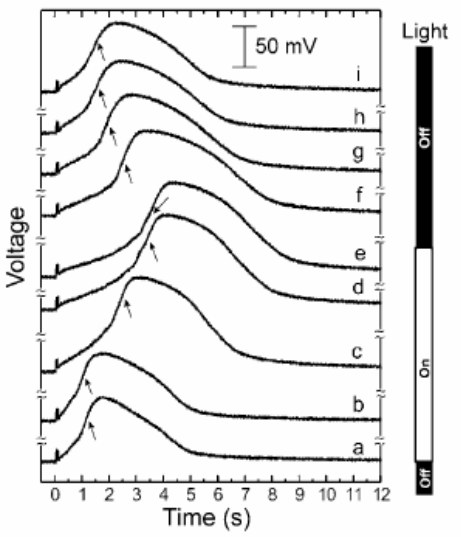

Figure 9.5: Recordings of the time dependence of the AP measured as a function of illumination simultaneous with magnetic measurements starting after 1 h dark accommodation. Trace **a**, light off; trace **b**, 10 min light on; trace **c**, 20 min light on; trace **d**, 30 min light on; trace **e**, 40 min light on (here we waited for an additional 20 min to complete 1 h in the light accommodation); trace **f**, 10 min light off; trace **g**, 20 min light off; trace **h**, 30 min light off; and trace **i**, 40 min light off. Small arrows indicate the points, corresponding to those that were observed in Fig. 9.4.

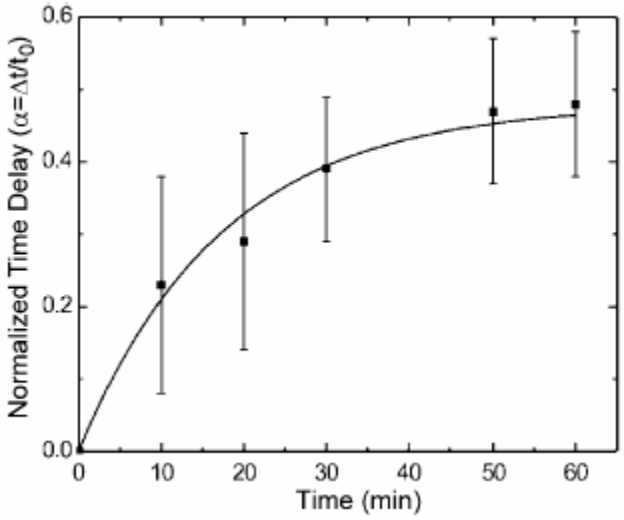

Figure 9.6: Averaged normalized temporal shift of the maximum of the measured magnetic field (AC) with increasing illumination exposure time. Eight cells were considered.

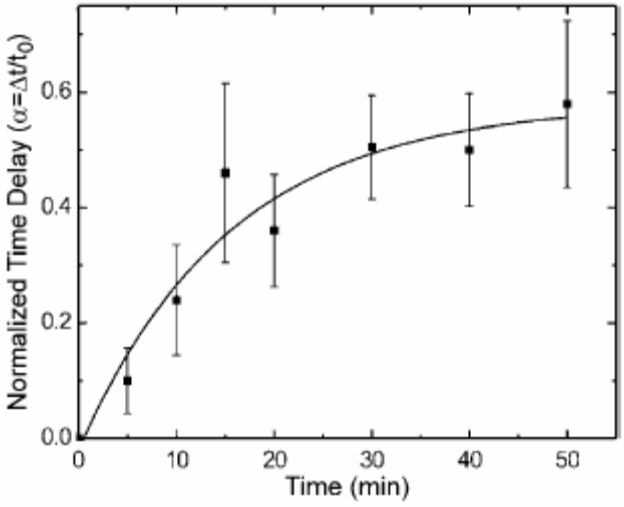

Figure 9.7: Averaged normalized temporal shift of the maximum of the measured AP with increasing illumination exposure time. Fifteen cells were considered.

9.4.2. Modeling

C. corallina internodal cells are, to a very good approximation, cylindrically symmetric and therefore ideally suitable for electrophysiological model studies. Several models followed the HH work on the nerve axon [35] and were adapted to *C. corallina* internodal cells [36] or were devoted to studies of relations between AP, AC, and associated magnetic field [26,27,33]. Here we will try to show that AP in *C. corallina* internodal cells experiences similarity to AP in those animal cells (heart, brain) where the ‘‘biochemical AP’’ is known to exist in addition to HH AP.

The HH type model is based purely on the kinetics of plasma membrane channels and the electrical properties of membrane but does not account for changes in $[Ca^{2+}]c$. This factor, however, requires consideration in the context of this study because alterations in $[Ca^{2+}]c$ were observed experimentally under the influence of light/dark transitions [24] and are in qualitative agreement with our model prediction. We have used an extended model of Othmer [20], which describes the dynamics of $[Ca^{2+}]c$ in the context of a second messenger system. In that model, the AP in *Chara* is successfully described by an electrically stimulated release of Ca^{2+} from internal stores. The resulting changes in membrane conductance are the direct consequence of this dynamic change in $[Ca^{2+}]c$. In this extended model, the thresholdlike dependence of Ca^{2+} mobilization on electrical stimulation can be simulated by combining the following two processes:

i. The voltage-dependent synthesis/breakdown of the second messenger inositol 1,4,5-trisphosphate (IP_3).

ii. The concerted action of IP_3 and Ca^{2+} on the gating of the receptor channels, which conduct Ca^{2+} release from internal stores.

The model has been proved suitable to simulate a range of experimental results in the context of the AP in *Chara*, including a complex behavior of Ca^{2+} mobilization under periodic stimulation with higher-order phase locking and irregular responses upon increased stimulation frequency. This demonstrates that the all-or-none type activation of the action potential is only the consequence of the preceding all or- none type mobilization of Ca^{2+} from internal stores. The dependency of the gating of the receptor channel on $[Ca^{2+}]c$ suggests that the Ca^{2+} concentration before stimulation of the AP has an influence on the following excitation kinetics.

To examine the effect of variable $[Ca^{2+}]c$ on the kinetics of the electrically stimulated changes in Ca^{2+}, we modified the model as follows: Cells move excess Ca^{2+} from the cytoplasm back into internal stores by an endogenous Ca^{2+} pump system (e.g., [37]). In the model, this process is accounted for by a Hill function:

$$\overline{g}(C) = \frac{\overline{p}_1 C^4}{C^4 + \overline{p}_2^4} \tag{9.1}$$

In this equation, $\overline{p}_1$ and $\overline{p}_2$ are the Hill coefficients, and C is the cytosolic Ca^{2+} concentration. For more details, see Othmer [23]. To achieve different $[Ca^{2+}]c$ under resting conditions, which are known to occur during light/dark transitions [24,25], we varied the Hill factor $\overline{p}_2$ in Eq. 1. This procedure is only an indirect approach, since the chloroplasts from which the Ca^{2+} originates during light/dark transitions [24] are not considered as extra Ca^{2+} pool in the model for $[Ca^{2+}]c$ dynamics. Nonetheless, this simple manipulation of the model should be sufficient to provide basic insight into the dependency of Ca^{2+} mobilization on $[Ca^{2+}]c$.

Fig. 9.8 illustrates the results of this simulation. As a consequence of reduced Ca^{2+} pump activity, the resting $[Ca^{2+}]c$ increases over the physiological range from ~ 20 nM to 200 nM. This roughly covers the changes in $[Ca^{2+}]c$ of 50–250 nM found in response to light/dark transitions

in *Chara* [24,25]. The simulation further shows that an elevation of $[Ca^{2+}]c$ before the stimulation results in a progressive shortening of the delay time between stimulation and the rapid phase of $[Ca^{2+}]c$ rise. The dependence of this delay time on the resting $[Ca^{2+}]c$ concentration is plotted in the inset of Fig. 9.8.

On the assumption that the change in membrane voltage during the AP is only the consequence of an activation of $[Ca^{2+}]c$ -sensitive Cl^- channels [11,38], the model simulation compares well with the experimental data. The assumed progressive decrease in $[Ca^{2+}]c$ of ~ 150 nM after the transition from dark to light results in an increasing delay time between the electrical stimulus and the rapid phase of $[Ca^{2+}]c$ rise, or the activation of the Cl^- channels, respectively.

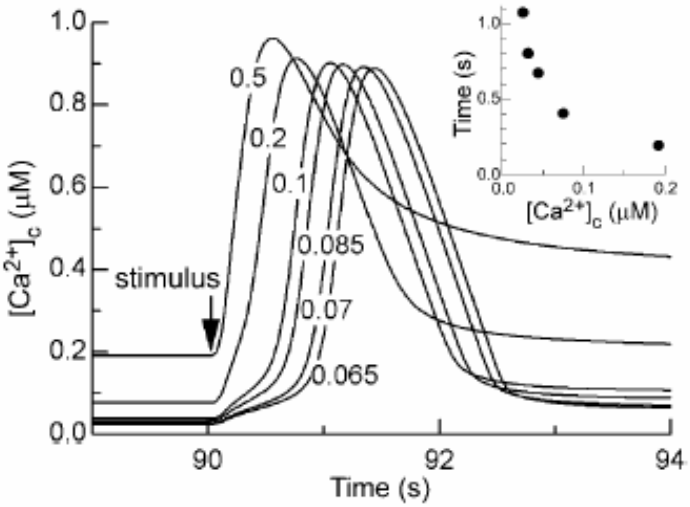

Figure 9.8: Simulated $[Ca^{2+}]c$ transients in response to a single electrical stimulation (100 ms/5 μA). Data were calculated with model parameters reported in Wacke *et al*. (2003) [20]. Different curves are obtained by changing the Hill coefficients $\bar{p}_2$ in the model term, which describes the buffering of $[Ca^{2+}]c$. An increase in $\bar{p}_2$ over a range of 0.065 μM–0.5 μM results in reduced Ca^{2+} buffering and a consequent increase in the resting $[Ca^{2+}]c$. In the simulation, pulses were started after 90 s in which the system was allowed to equilibrate. (*Inset*) Delay time between stimulus and maximal slope of $[Ca^{2+}]c$ increase as a function of resting $[Ca^{2+}]c$ before stimulation.

9.5. Analysis and discussion

The results of our measurements and subsequent model studies demonstrate the potential of using noninvasive magnetic measurements as a way to obtain information about the axial intracellular action currents associated with depolarization and repolarization of the membrane potential during AP propagation [27]. This current reflects the summed contribution of all transmembrane ionic currents as well as electrogenic transport and other secondary transport processes in intracellular compartments. The SQUID microscope with its high spatial resolution will be a convenient instrument in studying these events in details. In those cases where different transmembrane ionic currents can be observed as transiently separable events, the analysis and the interpretation of the data can be undertaken. This is possible, for example, in the case of the influence of light on the kinetics of ionic currents during the AP.

The main observation in this work was that a transfer of cells from the light into the dark resulted in an appreciable and reversible change in the kinetics of the action potential. Predominantly, the first part of the AC/AP temporal evolution, i.e., the slow depolarization part, increased progressively with time of light exposure; the rapid part of the AP, including depolarization and repolarization, was on the other hand only marginally affected. These observed changes in the kinetics of the *Chara* AP could in principle be modeled by a classical HH approach by adding a variable delay factor. However, there is no mechanistic motivation for such a delay factor, and it is difficult to envisage how a first-order voltage dependent process could produce such a long and variable delay.

The experimental observations are, on the other hand, fully consistent with the view that the AP in *Chara* is of a ‘‘chemical’’ nature, i.e., based on a quasi all-or-none type liberation of Ca^{2+} from internal stores [17,20]. The model for the *Chara* AP [20] predicts that a decrease of

the resting $[Ca^{2+}]c$ by ~ 250 nM, as is expected to occur in response to a dark/light transition [24,39], causes a delay in the onset of the rapid rise in $[Ca^{2+}]c$ during excitation. Assuming that the activation of the Cl^- channels, which cause the depolarization, is the direct consequence of the change in $[Ca^{2+}]c$, the measured data nicely match the model prediction, even on a quantitative basis. The model further predicts that a modulation of the resting $[Ca^{2+}]c$ has no big effect on the kinetics of the bulk changes of $[Ca^{2+}]c$. Again, this prediction is met by the present data because the features in the temporal evolution of the AC/AP were basically unchanged.

Previous measurements have assessed the changes in $[Ca^{2+}]c$ after light/dark transitions indirectly by recording the velocity of cytoplasmic streaming, because this velocity is proportional to $[Ca^{2+}]c$ [40]. In long-term recordings, Plieth and co-workers [41] found that it took ~ 30 min to achieve a steady streaming velocity after transferring plants from dark to light. A slow time course for the change in Ca^{2+} in a similar order of magnitude can also be deduced from direct recordings of $[Ca^{2+}]c$ in *Chara*. The usual rise in $[Ca^{2+}]c$ after light/dark transitions was even after 5 min in the dark not yet fully saturated [39]. Hence, the time course in Ca^{2+} changes after light/dark transitions are of the same order of magnitude as the one we found in our measurements within experimental errors. Therefore, the entire observation of the change in the AP kinetics found under light/dark transition can be quantitatively explained by a slow progressing change in the resting $[Ca^{2+}]c$ and a consequent modulation of this parameter on the release of Ca^{2+} from internal stores.

9.6. Conclusion

We performed electric measurements of the AP in parallel with noninvasive magnetic measurements of the associated action current and found an excellent correspondence. The

temporal evolution of electric and magnetic signals and the modeling study enabled us to associate the altered depolarization of illuminated *Chara corallina* internodal cells with changes in the cytoplasmic concentration of Ca^{2+} ions in combination with a second messenger cascade. This is consistent with the view of a biochemical nature of electrically elicited AP and AC in these cells.

Our experimental results demonstrate the potential of SQUID microscope imaging for noninvasive magnetic measurements of axial intracellular current in electrically stimulated single internodal cells of *Chara corallina* under the influence of light. This kind of measurement provides a valuable technique to complement the longer existing electrophysiological methods in studies of plant cells.

9.7. Acknowledgments

Our sincere thanks to Dr. Randy Wayne of Cornell University for providing us with specimens of Chara corallina algae. We thank John Wikswo for his hospitality (Z.T.) and comments on this manuscript. One of us (L.F.) would like to thank to Mary J. Beilby for the program information on the calculation of temporal evolution of AP in Chara corallina.

This research has been supported in part by a National Research Council Collaboration in Basic Science and Engineering program and by National Institutes of Health (NIH) grants R42 GM54963 and R01 HL58241. The SQUID microscope has been developed under NIH grant R42GM54963 and National Science Foundation grant DBI 9604948.

9.8. References

[1] K. Umrath, "On the excitation propagation in higher plants," *Planta*, vol. 7, pp. 174-207, 1929.

[2] A. B. Hope and G. P. Findlay, "The action potential in Chara," *Plant and Cell Physiology*, vol. 5, pp. 377-379, 1964.

[3] A. B. Hope and N. A. Walker, *Physiology of Giant Algal cells*. London: Cambridge University Press., 1975.

[4] M. Tazawa, T. Shimmen, and T. Mimura, "Membrane Control in the Characeae," *Annual Review of Plant Physiology and Plant Molecular Biology*, vol. 38, pp. 95-117, 1987.

[5] T. Shimmen, T. Mimura, M. Kikuyama, and M. Tazawa, "Characean Cells As A Tool for Studying Electrophysiological Characteristics of Plant-Cells," *Cell Structure and Function*, vol. 19, no. 5, pp. 263-278, 1994.

[6] M. J. Beilby, "Current Voltage Curves for Plant Membrane Studies - A Critical Analysis of the Method," *Journal of Experimental Botany*, vol. 41, no. 223, pp. 165-182, 1990.

[7] H. D. Kranz, D. Miks, M. L. Siegler, I. Capesius, C. W. Sensen, and V. A. R. Huss, "The Origin of Land Plants - Phylogenetic-Relationships Among Charophytes, Bryophytes, and Vascular Plants Inferred from Complete Small-Subunit Ribosomal-Rna Gene-Sequences," *Journal of Molecular Evolution*, vol. 41, no. 1, pp. 74-84, 1995.

[8] K. G. Karol, R. M. McCourt, M. T. Cimino, and C. F. Delwiche, "The closest living relatives of land plants," *Science*, vol. 294, no. 5550, pp. 2351-2353, 2001.

[9] M. J. Beilby and H. G. L. Coster, "Action Potential in Chara-Corallina .2. 2 Activation-Inactivation Transients in Voltage Clamps of the Plasmalemma," *Australian Journal of Plant Physiology*, vol. 6, no. 3, pp. 323-335, 1979.

[10] U. Homann and G. Thiel, "Cl- and K+ Channel Currents During the Action-Potential in Chara - Simultaneous Recording of Membrane Voltage and Patch Currents," *Journal of Membrane Biology*, vol. 141, no. 3, pp. 297-309, 1994.

[11] G. Thiel, U. Homann, and C. Plieth, "Ion channel activity during the action potential in Chara: New insights with new techniques," *Journal of Experimental Botany*, vol. 48, pp. 609-622, 1997.

[12] M. Kikuyama, "Ion Efflux During Excitation of Characeae - Comparison of Voltage-Clamp and Conductometry Method for Efflux Measurement," *Plant and Cell Physiology*, vol. 28, no. 8, pp. 1427-1434, 1987.

[13] P. H. Barry, "Volume flows and pressure changes during action potential in cells of Chara australis. I. Experimental results.," *Journal of Membrane Biology*, vol. 3, pp. 313-334, 1970.

[14] V. A. Shepherd, M. J. Beilby, and T. Shimmen, "Mechanosensory ion channels in charophyte cells: the response to touch and salinity stress," *European Biophysics Journal with Biophysics Letters*, vol. 31, no. 5, pp. 341-355, 2002.

[15] R. E. Williamson and C. C. Ashley, "Free Ca2+ and Cytoplasmic Streaming in the Alga Chara," *Nature*, vol. 296, no. 5858, pp. 647-651, 1982.

[16] M. Kikuyama and M. Tazawa, "Transient Increase of Intracellular Ca-2+ During Excitation of Tonoplast-Free Chara Cells," *Protoplasma*, vol. 117, no. 1, pp. 62-67, 1983.

[17] M. Wacke and G. Thiel, "Electrically triggered all-or-none Ca2+-liberation during action potential in the giant alga Chara," *Journal of General Physiology*, vol. 118, no. 1, pp. 11-21, 2001.

[18] K. Okihara, T. Ohkawa, I. Tsutsui, and M. Kasai, "A Ca-2+-Dependent and Voltage-Dependent Cl--Sensitive Anion Channel in the Chara Plasmalemma - A Patch-Clamp Study," *Plant and Cell Physiology*, vol. 32, no. 5, pp. 593-601, 1991.

[19] M. Tazawa and M. Kikuyama, "Is Ca2+ release from internal stores involved in membrane excitation in characean cells?," *Plant and Cell Physiology*, vol. 44, no. 5, pp. 518-526, 2003.

[20] M. Wacke, G. Thiel, and M. T. Hutt, "Ca2+ dynamics during membrane excitation of green alga Chara: Model simulations and experimental data," *Journal of Membrane Biology*, vol. 191, no. 3, pp. 179-192, 2003.

[21] M. T. Nelson, H. Cheng, M. Rubart, L. F. Santana, A. D. Bonev, H. J. Knot, and W. J. Lederer, "Relaxation of Arterial Smooth-Muscle by Calcium Sparks," *Science*, vol. 270, no. 5236, pp. 633-637, 1995.

[22] P. Chavis, L. Fagni, J. B. Lansman, and J. Bockaert, "Functional coupling between ryanodine receptors and L-type calcium channels in neurons," *Nature*, vol. 382, no. 6593, pp. 719-722, 1996.

[23] H. G. Othmer, "Signal transduction and second messenger systems," in *In Case Studies In Mathematical Modeling – Ecology, Physiology and Cell Biology*. H. G. Othmer, F. R. Adler, M. A. Lewis, and J. Dallon, Eds. NJ: Prentice Hall, 1997, pp. 99-126.

[24] A. J. Miller and D. Sanders, "Depletion of Cytosolic Free Calcium Induced by Photosynthesis," *Nature*, vol. 326, no. 6111, pp. 397-400, 1987.

[25] C. Plieth, B. Sattelmacher, and U. P. Hansen, "Light-induced cytosolic calcium transients in green plant cells. I. Methodological aspects of chlorotetracycline usage in algae and higher-plant cells," *Planta*, vol. 207, no. 1, pp. 42-51, 1998.

[26] J. W. Clark and R. Plonsey, "A mathematical evaluation of the core conductor model," *Biophys. J.*, vol. 6, pp. 95-112, 1966.

[27] J. K. Woosley, B. J. Roth, and J. P. Wikswo, "The Magnetic-Field of A Single Axon - A Volume Conductor Model," *Mathematical Biosciences*, vol. 76, no. 1, pp. 1-36, 1985.

[28] Z. Trontelj, R. Zorec, V. Jazbinsek, and S. N. Erne, "Magnetic Detection of A Single Action-Potential in Chara-Corallina Internodal Cells," *Biophys. J.*, vol. 66, no. 5, pp. 1694-1696, 1994.

[29] D. Drung, "The Ptb 83-Squid System for Biomagnetic Applications in A Clinic," *IEEE Trans. Appl. Supercond.*, vol. 5, no. 2, pp. 2112-2117, 1995.

[30] F. Baudenbacher, N. T. Peters, and J. P. Wikswo, Jr., "High Resolution Low-Temperature Superconductivity Superconducting Quantum Interference Device Microscope for Imaging Magnetic Fields of Samples at Room Temperatures," *Rev. Sci. Instrum.*, vol. 73, no. 3, pp. 1247-1254, 2002.

[31] J. P. Barach, J. A. Freeman, and J. P. Wikswo, "Experiments on the Magnetic-Field of Nerve Action-Potentials," *J. Appl. Phys.*, vol. 51, no. 8, pp. 4532-4538, 1980.

[32] L. Trahms, S. N. Erne, Z. Trontelj, G. Curio, and P. Aust, "Biomagnetic Functional Localization of A Peripheral-Nerve in Man," *Biophys. J.*, vol. 55, no. 6, pp. 1145-1153, 1989.

[33] M. Slibar, Z. Trontelj, V. Jazbinsek, G. Thiel, and W. Mueller, "Magnetic field and electric potential of excited plant cell Chara corallina: calculation and comparison with experiment,". C. J. Aine, Y. Okada, G. Stroink, S. J. Swithenby, and C. C. Wood, Eds. Springer, 2000, pp. 679-682.

[34] T. Mimura and M. Tazawa, "Light-Induced Membrane Hyperpolarization and Adenine-Nucleotide Levels in Perfused Characean Cells," *Plant and Cell Physiology*, vol. 27, no. 2, pp. 319-330, 1986.

[35] A. L. Hodgkin and A. F. Huxley, "A quantitative description of membrane current and its application to conductance and excitation in nerve," *Journal of Physiology (London)*, vol. 117, pp. 500-544, 1952.

[36] M. J. Beilby, "Cl- Channels in Chara," *Philosophical Transactions of the Royal Society of London Series B-Biological Sciences*, vol. 299, no. 1097, pp. 435-445, 1982.

[37] A. S. N. Reddy, "Calcium: silver bullet in signaling," *Plant Science*, vol. 160, no. 3, pp. 381-404, 2001.

[38] B. Biskup, D. Gradmann, and G. Thiel, "Calcium release from InsP(3)-sensitive internal stores initiates action potential in Chara," *Febs Letters*, vol. 453, no. 1-2, pp. 72-76, 1999.

[39] C. Plieth, "Estimation of ion concentrations and their variations in cells and tissues of green plants using image analysis as ratiometric fluorescence microscopy and laser Doppler anemometry." PhD University of Kiel, Germany, 1995.

[40] D. W. Mccurdy and A. C. Harmon, "Calcium-Dependent Protein-Kinase in the Green-Alga Chara," *Planta*, vol. 188, no. 1, pp. 54-61, 1992.

[41] C. Plieth, B. Sattelmacher, and U. P. Hansen, "Light-induced cytosolic calcium transients in green plant cells. II. The effect on a K+ channel as studied by a kinetic analysis in Chara corallina," *Planta*, vol. 207, no. 1, pp. 52-59, 1998.

CHAPTER X

SUMMARY AND FUTURE WORK

10.1. Summary

The objectives of this research were the development and utilization of monolithic thin-film low-critical-temperature (*Tc*) superconducting quantum interference device (SQUID) sensors to measure and image magnetic fields with an unprecedented combination of high spatial resolution and field sensitivity.

The review of high resolution imaging of magnetic fields and scanning SQUID microscopy in Chapter 2 demonstrated the magnitude and importance of developing new techniques capable of combining high sensitivity measurements with high spatial resolution imaging. This goal was achieved through the innovative design of monolithic low-*Tc* SQUID sensors optimized to measure the magnetic field of specific magnetic source configurations. Chapter 3 presented a review of the methodology to optimize, design and characterize SQUID sensors.

Chapter 4 presented the development of two monolithic sensors, the bare SQUID and the multiloop SQUID, as well as their incorporation into the microscope system. The first sensor was optimized to measure magnetic dipolar sources, which are typically encountered in rock magnetism. The second one was designed to measure axial current or sheet current sources typically found in bioelectric phenomena. The system was used to image the magnetic field distributions of geological thin sections and isolated rabbit hearts.

The improvement on spatial resolution and sensitivity are key elements in the advance of rock magnetism and cardiac electrophysiology. The new SQUID microscope enabled rock-magnetic and paleomagnetic experiments on individual grains in standard petrographic thin sections, allowing for matching the magnetic features with the minerals composition.

The sensitivity achieved by using monolithic multiloop SQUID sensors, in combination with optical transmembrane potential imaging, allows comprehensive studies of the relationship between extracellular potentials, transmembrane potentials and action currents in cardiac tissue.

Details of the design and optimization of the monolithic bare SQUID sensors were presented in Chapter 5. Three sensor configurations were designed, fabricated, characterized and tested. The best sensor proved to be the 40-μm hole and 40-μm washer bare SQUID, which achieved a field resolution of 1.4 $pT/Hz^{1/2}$ with a corresponding flux noise of 5 $\mu\Phi_o/Hz^{1/2}$. The system was used to scan and image the magnetic field of a thin section of the Martian meteorite, attaining a spatial resolution of 120 μm, which was comparable to the sensor-to-sample separation.

In Chapter 6, details of the design and optimization of the monolithic multiloop SQUID sensor were presented, as well as high-resolution images of cardiac biomagnetic fields. A magnetic field resolution of 450 $fT/Hz^{1/2}$ with a equivalent flux noise of 1.7 $\mu\Phi_o/Hz^{1/2}$ was accomplished using a 5-spoke, 250 μm diameter multiloop SQUID. The sensor was used to measure the magnetic field generated from planar excitation waves in a whole heart preparation at a sensor-to-sample distance of about 100 μm. In agreement with the predictions of the bidomain model, a current component parallel to the wave front was found, providing supportive evidence of the adequacy of the such model for forward calculations of the MCG.

Of great theoretical and practical importance is the study the Martian magnetic field. Scientists have not yet been able to find an answer to the actual strong magnetization crust of the planet. Evidences of the ancient Martian magnetic field were found in the ALH84001 Martian meteorite. Standard paleomagnetic techniques estimate a lower limit for the magnetization of this meteorite, and therefore do not provide precise information about the Martian magnetic field at the time of the meteorite formation. These techniques do not have the sensitivity and resolution to explore the meteorite internal magnetic heterogeneities. Chapter 7 shows the first evidence of an intense magnetic field in Mars 4 billion years ago. Using the new SQUID microscope system with a bare SQUID sensor, high resolution scans of a 30-μm thin section of the Martian meteorite were obtained. This study demonstrated the ability of our system to perform measurements not achievable with any other technique available.

In addition, our high sensitivity system was used to successfully detect and identify single magnetic microparticles by combing microfluidic devices and low-*Tc* SQUID microscopy. Chapter 8 presented the detection and identification of 6-μm single magnetic particles confined inside a microfluidic channel. These results open new possibilities of magnetically tagging cells and subsequently discriminating them according to their magnetic moment. The practical relevance of this measurement lies on the possibility of creating high-content magnetic flow cytometry and magnetic cell sorting devices.

Finally, Chapter 9 showed the results of our experiments in plant electrophysiology. The goal of the project was to explore the influence of light in the intracellular axial currents in Chara corallina single cells, by parallel and noninvasive electric and magnetic measurements of the action potential and action currents. The temporal evolution of electric and magnetic signals and the appropriate modeling enabled us to associate the altered depolarization with changes in the

cytoplasmic concentration of Ca^{2+} ions and its correspondent influence in Ca^{2+}-sensitive Cl^- channels. Our instrument proved to be a valuable tool for biological noninvasive magnetic experiments and could provide complementary information on single ion channel microelectric measurements.

10.2. Future work

RT- sample Low-*Tc* SQUID microscopy is an emerging technique and there is a lot of space for new developments. Recently, Hypres, the company that manufactures our chips, has improved its fabrication process, allowing us to have tighter optimization constraints and, therefore, improving the noise characteristics of our sensors. With this in mind, we have designed a new set of bare and multiloop SQUID sensors. Tables 10.1 (a) and (b) show the expected noise performances and field sensitivities of the latest generation of SQUID sensors.

As part of the continuing effort to improve our SQUID characterization techniques, we have teamed up with the German national metrology institute, *Physikalisch-Technische Bundesanstalt* (PTB). They have characterized a set of our latest multiloop SQUID sensors, which achieved excellent noise performance. Table 10.2 shows a summary of these results. We believe that part of this noise characterization improvement originates from the use of an innovative set of SQUID electronics with a low noise integrated current source [1]. We are currently testing the same set of SQUID electronics and expect to reproduce such results in our lab.

One of the key factors that will improve RT-sample low-*Tc* SQUID microscopy is our ability to get even closer to the sample. As shown in Chapter 4, the spatial resolution and field sensitivity to image magnetic dipolar sources will drastically improve by placing smaller sensors

closer to the sample. In order to achieve such small distances, one ought to reduce the vacuum window thickness and make sure that the surface of the sensor is parallel to the surface of the window. Lee *et al.*[2] reported (on one occasion) a sample-to-sensor distance of 15 μm using a 3-μm thick silicon nitride vacuum window. A realistic goal is to reduce our current sample-to-sensor distance by at least a factor of two (that is, to 50 μm), improving the spatial resolution by the same factor and the moment sensitivity of our system by a factor of eight.

Table 10.1 (a) and (b): Expected flux noise and field sensitivity of the new set of optimized bare and multiloop SQUID designs, respectively.

(a)

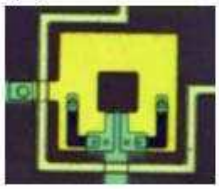

Washer w (μm)	Hole h (μm)	β_L $\beta_L \approx 1$	β_C $\beta_c \leq 0.7$	$S\phi^{1/2}$ (1KHz) ($\mu\phi_o/Hz^{1/2}$)	$S_B^{1/2}$ (1KHz) (pT/ $Hz^{1/2}$)
30 μm	5 μm	1	0.65	0.415	0.7
40 μm	5 μm	1	0.65	0.495	0.5
50 μm	5 μm	1	0.65	0.568	0.4

(b)

No. Spokes	Diameter (μm)	β_L $\beta_L \approx 1$	β_C $\beta_c \leq 0.7$	$S\phi^{1/2}$ (1KHz) ($\mu\phi_o/Hz^{1/2}$)	$S_B^{1/2}$ (1KHz) (fT/ $Hz^{1/2}$)
5	300	1	0.63	0.40	50
5	600	1	0.63	0.57	18
5	900	1	0.63	0.57	10

Table 10.2: PTB flux noise measurements of new set of multiloop SQUIDs and corresponding expected field sensitivity at 1KHz.

No. Spokes	Diameter (μm)	$S\phi^{1/2}$ (1Hz) ($\mu\phi_o/Hz^{1/2}$)	$S\phi^{1/2}$ (100Hz) ($\mu\phi_o/Hz^{1/2}$)	$S\phi^{1/2}$ (1KHz) ($\mu\phi_o/Hz^{1/2}$)	$*S_B^{1/2}$ (1KHz) ($fT/Hz^{1/2}$)
5	250	5.4	1.1	0.8	212
6	500	6.3	2.7	2.6	142
8	1000	6.5	1.4	1.1	17

Following the efforts by Ketchen and Kirtley *et al.*[3], a major step in instrument development will be the possibility of measuring the other two components of the magnetic field and, in this way, build the next generation of SQUID microscopes: the Vector Scanning SQUID microscope. Dr. Franz Baudenbacher's group in collaboration with Dr. Benjamin Weiss at MIT are planning to develop this pioneering instrument which will bring to the table a whole new variety of magnetic information. It is not difficult to foresee the significant impact that this new generation of SQUID microscopes will have in the development of the rock-magnetic and biomagnetic field sciences. I am looking forward to seeing it!

10.3. References

[1] D. Drung, "High-T-c and low-T-c dc SQUID electronics," *Superconductor Science & Technology*, vol. 16, no. 12, pp. 1320-1336, 2003.

[2] T. S. Lee, Y. R. Chemla, E. Dantsker, and J. Clarke, "High-T-c SQUID microscope for room temperature samples," *IEEE Trans. Appl. Supercond.*, vol. 7, no. 2, pp. 3147-3150, 1997.

[3] M. B. Ketchen, J. R. Kirtley, and M. Bhushan, "Miniature vector magnetometer for scanning SQUID microscopy," *IEEE Trans. Appl. Supercond.*, vol. 7, no. 2, pp. 3139-3142, 1997.

APPENDIX A

THEORETICAL CONSIDERATIONS FOR IDENTIFICATION OF MAGNETIC MICROPARTICLES

A.1. SQUID identification of a single magnetic dipole

The magnetic field of a magnetic dipole is given by:

$$\vec{B}(\vec{r}) = \frac{\mu_0}{4\pi}\left[-\frac{\vec{m}}{r^3} + \frac{3(\vec{m}\cdot\vec{r})\vec{r}}{r^5}\right]. \tag{A.1}$$

In our experimental setup, the SQUID system detects the vertical (z) component of the magnetic field. Assuming an arbitrary dipole moment $\vec{m} = m_x\hat{x} + m_y\hat{y} + m_z\hat{z}$ moving along a generic parameterized path in $\boldsymbol{R}^3$, $\gamma = \{(x(t), y(t), 0) : t_0 \le t \le t_1\}$, and that the SQUID sensor is positioned at a distance h above the trajectory plane, we get

$$B_z(\vec{m},t) = -\frac{\mu_0}{4\pi}\frac{m_z}{\left[(x_s - x(t))^2 + (y_s - y(t))^2 + h^2\right]^{3/2}} + \frac{\mu_0}{4\pi}\frac{3h\left[m_x(x_s - x(t)) + m_y(y_s - y(t)) + m_z h\right]}{\left[(x_s - x(t))^2 + (y_s - y(t))^2 + h^2\right]^{3/2}}, \tag{A.2}$$

where x_s and y_s stand for the x and y coordinates of the SQUID sensor. Rearranging (A.2) gives

$$\begin{aligned} B_z(\vec{m},t) = {} & m_x\frac{\mu_0}{4\pi}\frac{3h(x_s - x(t))}{\left[(x_s - x(t))^2 + (y_s - y(t))^2 + h^2\right]^{5/2}} + m_y\frac{\mu_0}{4\pi}\frac{3h(y_s - y(t))}{\left[(x_s - x(t))^2 + (y_s - y(t))^2 + h^2\right]^{5/2}} + \\ & + m_z\frac{\mu_0}{4\pi}\frac{2h^2 - (x_s - x(t))^2 - (y_s - y(t))^2}{\left[(x_s - x(t))^2 + (y_s - y(t))^2 + h^2\right]^{5/2}}. \end{aligned} \tag{A.3}$$

The SQUID sensor is generally not blind to any of the three components of the magnetic moment. Changing m_x, m_y or m_z will change the output voltage of a SQUID sensor. The only way to be insensitive to m_x or m_y is to have a very particular straight trajectory and the SQUID perfectly aligned over it so that $x(t) = \text{constant} = x_s$ (or, equivalently, $y(t) = \text{constant} = y_s$). As

for m_z, the bead has to travel along a circle of radius $h\sqrt{2}$ and the SQUID has to be positioned right above the center of the circle in order to be insensitive to the z component of the moment. We have used a serpentine path, in which x, y and $\rho = \sqrt{x^2 + y^2}$ vary, and such theoretical conditions are never met.

A.2. Solution uniqueness analysis for fixed path

The path is fixed by the geometry of the microfluidic serpentine channel. To address the uniqueness of the solution for a fixed path, we first analyze the simpler case represented by (A.3), where the moment is not changing direction as the particle moves. Here it is convenient to use some tools of functional analysis.

Equation (A.3) shows that the z-component of the magnetic field is a linear combination of three functions (vectors) in the Hilbert Space $L^2(\boldsymbol{R})$:

$$B_z(\vec{m},t) = m_x f_1(t) + m_y f_2(t) + m_z f_3(t)\,, \tag{A.4}$$

where $f_1(t) = \dfrac{\mu_0}{4\pi} \dfrac{3h\left(x_s - x(t)\right)}{\left[\left(x_s - x(t)\right)^2 + \left(y_s - y(t)\right)^2 + h^2\right]^{5/2}}$, $f_2(t) = \dfrac{\mu_0}{4\pi} \dfrac{3h\left(y_s - y(t)\right)}{\left[\left(x_s - x(t)\right)^2 + \left(y_s - y(t)\right)^2 + h^2\right]^{5/2}}$ and

$f_3(t) = \dfrac{\mu_0}{4\pi} \dfrac{2h^2 - \left(x_s - x(t)\right)^2 - \left(y_s - y(t)\right)^2}{\left[\left(x_s - x(t)\right)^2 + \left(y_s - y(t)\right)^2 + h^2\right]^{5/2}}$.

Since the denominators are never zero, as $h > 0$, and the parameterized path is smooth and has finite length, it is easy to verify that those three functions are square integrable on $\boldsymbol{R}$. Hence, to show that the solution is unique is equivalent to show that the three vectors f_1, f_2 and f_3 are linearly independent, constituting a basis for a subspace of $L^2(\boldsymbol{R})$. In such case, the decomposition of $B_z(\vec{m},t)$ into $f_1(t)$, $f_2(t)$ and $f_3(t)$ is unique and there is only one set of

coefficients (m_x, m_y, m_z) associated with it. Since the functions f_1, f_2 and f_3 have the same denominator, it is sufficient to verify that the condition holds for the numerators. That is,

$$\lambda_1 f_1 + \lambda_2 f_2 + \lambda_3 f_3 = 0 \Rightarrow \lambda_1 3h(x_s - x(t)) + \lambda_2 3h(y_s - y(t)) + \lambda_3[2h^2 - (x_s - x(t))^2 - (y_s - y(t))^2] = 0, \forall t \in R \tag{A.5}$$

Therefore, to ensure uniqueness, one should choose the functions $x(\cdot)$ and $y(\cdot)$ so that the only solution to (A.5) is the trivial solution $\lambda_1 = \lambda_2 = \lambda_3 = 0$. It is worth noticing that the three aforementioned specific paths that lead to insensitivity to one component of the magnetic moment are embedded in (A.5), as they clearly imply non-unique solutions.

At this point, for the sake of avoiding lengthy and cumbersome calculations, we will suppose a slightly different geometry for our serpentine channel. Instead of the actual piecewise path, easier to fabricate and comprised of straight line segments and semicircles, we assume that the channel has the shape of a sine function. However, all the analysis that follows can be applied to the actual geometry.

The serpentine channel can be described by

$$x(t) = t \text{ , } y(t) = \sin(t) \text{ , for } t_0 \le t \le t_f \text{ , and } x(t) = y(t) = 0 \text{ otherwise .} \tag{A.6}$$

Substituting (A.6) in (A.5) gives

$$\lambda_1 3h(x_s - t) + \lambda_2 3h(y_s - \sin(t)) + \lambda_3\left[2h^2 - (x_s - t)^2 - (y_s - \sin(t))^2\right] = 0, \quad \forall t \in I \text{ ,} \tag{A.7}$$

where I is the interval [t_0 , t_f]. Clearly, there is no other combination, besides $\lambda_1 = \lambda_2 = \lambda_3 = 0$, that satisfies the equation over the whole interval. Thus, the solution is unique.

Now consider the more complex case where the bead rotates around the z-axis due to asymmetries in the velocity profile, as detailed in the paper. In this case, the moment changes its direction with respect to the fixed coordinate system x-y-z. We assume that the z-component of

the magnetic moment does not change along the path. Consequently, $\vec{m}$ is now a function of *t*: $\vec{m}(t) = m_x(t)\hat{x} + m_y(t)\hat{y} + m_z\hat{z}$. In order to derive the equations for $m_x(t)$ and $m_y(t)$, it is first necessary to calculate the tangent vector with respect to the trajectory:

$$\hat{\tau}(t) = \frac{\dot{x}\,\hat{x} + \dot{y}\,\hat{y}}{\sqrt{\dot{x}^2 + \dot{y}^2}} = \frac{1}{\sqrt{1+\cos^2(t)}}\left[\hat{x} + \cos(t)\hat{y}\right] \tag{A.8}$$

Let $\vec{m}_0 = m_{x0}\hat{x} + m_{y0}\hat{y} + m_{z0}\hat{z}$ denote the magnetic moment at t_0, θ_0 denote the angle between $\hat{\tau}(0)$ and $\hat{x}$, and $\theta(t)$ denote the angle between $\hat{\tau}(t)$ and $\hat{x}$. Then

$$\cos(\theta_0) = \hat{\tau}(0)\cdot\hat{x} = 1/\sqrt{2} \quad , \quad \sin(\theta_0) = \hat{\tau}(0)\cdot\hat{y} = 1/\sqrt{2} \tag{A.9a}$$

$$\cos\left(\theta(t)\right) = \hat{\tau}(t)\cdot\hat{x} = 1/\sqrt{1+\cos^2(t)} \quad , \quad \sin\left(\theta(t)\right) = \hat{\tau}(t)\cdot\hat{y} = \cos(t)/\sqrt{1+\cos^2(t)}\,. \tag{A.9b}$$

To calculate $\vec{m}(t)$ we need to rotate $\vec{m}_0$ counterclockwise about the *z*-axis by $\theta(t) - \theta_0$:

$$\begin{bmatrix} m_x(t) \\ m_y(t) \\ m_z \end{bmatrix} = \begin{bmatrix} \cos\left(\theta(t)\right) & -\sin\left(\theta(t)\right) & 0 \\ \sin\left(\theta(t)\right) & \cos\left(\theta(t)\right) & 0 \\ 0 & 0 & 1 \end{bmatrix} \begin{bmatrix} \cos\left(\theta_0\right) & \sin\left(\theta_0\right) & 0 \\ -\sin\left(\theta_0\right) & \cos\left(\theta_0\right) & 0 \\ 0 & 0 & 1 \end{bmatrix} \begin{bmatrix} m_{x0} \\ m_{y0} \\ m_{z0} \end{bmatrix} \tag{A.10}$$

Substituting (A.9a) and (A.9b) in (A.10) yields

$$m_x(t) = \frac{1}{\sqrt{2\left[1+\cos^2(t)\right]}}\left[\left(1+\cos(t)\right)m_{x0} + \left(1-\cos(t)\right)m_{y0}\right]$$

$$m_y(t) = \frac{1}{\sqrt{2\left[1+\cos^2(t)\right]}}\left[\left(\cos(t)-1\right)m_{x0} + \left(1+\cos(t)\right)m_{y0}\right]\,. \tag{A.11}$$

$$m_z = m_{z0}$$

Substituting (A.11) in (A.4) yields

$$B_z(\vec{m}_0,t)=\frac{1}{\sqrt{2\left[1+\cos^2(t)\right]}}\left[\left(1+\cos(t)\right)m_{x0}+\left(1-\cos(t)\right)m_{y0}\right]f_1(t)+$$
$$+\frac{1}{\sqrt{2\left[1+\cos^2(t)\right]}}\left[\left(\cos(t)-1\right)m_{x0}+\left(1+\cos(t)\right)m_{y0}\right]f_2(t)+m_{z0}f_3(t)\,. \tag{A.12}$$

After some manipulation, we get

$$B_z(\vec{m}_0,t)=m_{x0}g_1(t)+m_{y0}g_2(t)+m_{z0}g_3(t)\,, \tag{A.13}$$

where

$$g_1(t)=\frac{\mu_0}{4\pi}\frac{1}{\sqrt{2\left[1+\cos^2(t)\right]}}\left\{\frac{3h\left[\left(x_s-t\right)\left(1+\cos(t)\right)+\left(y_s-\sin(t)\right)\left(\cos(t)-1\right)\right]}{\left[\left(x_s-t\right)^2+\left(y_s-\sin(t)\right)^2+h^2\right]^{5/2}}\right\}\,,$$

$$g_2(t)=\frac{\mu_0}{4\pi}\frac{1}{\sqrt{2\left[1+\cos^2(t)\right]}}\left\{\frac{3h\left[\left(x_s-t\right)\left(1-\cos(t)\right)+\left(y_s-\sin(t)\right)\left(1+\cos(t)\right)\right]}{\left[\left(x_s-t\right)^2+\left(y_s-\sin(t)\right)^2+h^2\right]^{5/2}}\right\}\ \text{and} \tag{A.14}$$

$$g_3(t)=f_3(t)=\frac{\mu_0}{4\pi}\frac{2h^2-\left(x_s-t\right)^2-\left(y_s-\sin(t)\right)^2}{\left[\left(x_s-t\right)^2+\left(y_s-\sin(t)\right)^2+h^2\right]^{5/2}}\,.$$

Finally, substituting (A.14) in (A.5) and rearranging terms, we get

$$\lambda_1 g_1+\lambda_2 g_2+\lambda_3 g_3=0\Rightarrow\lambda_1 3h\left[\left(x_s-t\right)\left(1+\cos(t)\right)+\left(y_s-\sin(t)\right)\left(\cos(t)-1\right)\right]+$$
$$\lambda_2 3h\left[\left(x_s-t\right)\left(1-\cos(t)\right)+\left(y_s-\sin(t)\right)\left(1+\cos(t)\right)\right]+\lambda_3\left[2h^2-\left(x_s-t\right)^2-\left(y_s-\sin(t)\right)^2\right]\sqrt{2\left[1+\cos^2(t)\right]}= \tag{A.15}$$
$$=0,\quad \forall t\in I$$

By inspecting (A.15), we conclude that only the trivial solution satisfies the equation for all values of *t*, demonstrating that the decomposition is also unique in the more general case. Even though the actual serpentine path has several properties similar to the sinusoidal path, the analysis above doesn't constitute a formal mathematical proof that the decomposition is unique in that case. However, one can see from (A.5) and (A.15) that very few non-pathological functions can lead to linear dependence and, consequently, to non-uniqueness. A strong evidence

that uniqueness also holds in the actual serpentine comes from the fact that the cost function (error) used in the optimization procedure always presented a clear global minimum. If multiple solutions were possible, then a global minimum could not exist. The rationale for using a serpentine channel is precisely to modulate the direction of the moment, therefore breaking symmetries that could eventually lead to an unsuccessful detection of one component of the magnetic moment.

A.3. Minimum distance between consecutive particles for successful identification

The peak-to-peak noise is about 0.05 times the p-p value of the signal. From figure A.1, which shows the normalized minimum sensor-to-bead distance versus serpentine segment number, we notice that roughly four segments are required for the signal to be comparable to the noise. Therefore, in the worst case, if one bead is leaving the serpentine, past the 4^{th} segment from the center, a second bead should be, at least, at the same distance from the sensor. Thus, 8 segments is the minimum distance between beads so as to avoid interferences. Now, each segment is comprised of a straight part and a semicircular part, with a total length of 480 μm. The minimum safe distance between consecutive beads along the serpentine is, then, 3.9 mm.

A.4. Noise incorporation in simulated signals

We simulated the SQUID output signal, which is the actual signal recorded during the experiments. SQUIDs do not sense magnetic fields directly, but magnetic fluxes instead. The integration over the effective area was also implemented in the model. Noise is always present in the measurements (it is both generated and picked up by the SQUID sensor), and the noise spectrum is an important way to characterize a SQUID design. Noise introduces distortions in

the shape of the traces and therefore it should be present in the simulated signals for a faithful visual comparison between experimental and simulated data (Fig. 8.2 and Fig. 8.3). It seems to us that it would be unrealistic and academic, in this case, to just simulate an ideal magnetic field and try to compare it with an actual experimental trace, as the signal-to-noise ratio is not very large. In addition, it allows for a good estimate of this figure.

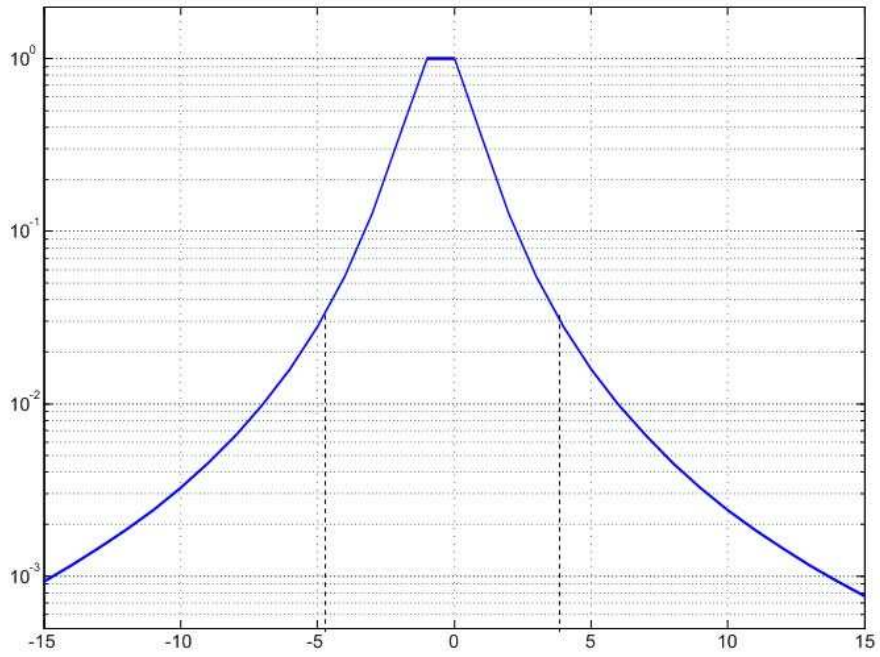

Figure A.1: Normalized minimum sensor-to-bead distance versus serpentine segment number.

A.5. Acknowledgements

I would like to thank Dr. Eduardo Andrade Lima for his important contribution in the development of this theoretical analysis.